

UCSF

UC San Francisco Electronic Theses and Dissertations

Title

Advanced Clinical Metabolic Health Assessment Using 3D Optical and Dual Energy X-Ray Imaging

Permalink

<https://escholarship.org/uc/item/8sv245g4>

Author

Ng, Bennett Kim

Publication Date

2018

Peer reviewed|Thesis/dissertation

Advanced Clinical Metabolic Health Assessment Using 3D Optical and Dual Energy X-Ray Imaging

by

Bennett Kim Ng

DISSERTATION

Submitted in partial satisfaction of the requirements for the degree of

DOCTOR OF PHILOSOPHY

in

Bioengineering

in the

GRADUATE DIVISION

of the

UNIVERSITY OF CALIFORNIA, SAN FRANCISCO

AND

UNIVERSITY OF CALIFORNIA, BERKELEY

Dedication

In August 2013 when I began this PhD, I had mixed emotions. I was excited for the opportunities, uncertain about the challenges, and unfamiliar with the surroundings. A PhD represented one of those tasks too large to really fathom at the outset. Now, five years later, I find myself incredibly thankful. Thankful for the experiences, the learning, and the relationships that I will have for the rest of my life. While there is only one name listed as the author of any dissertation, I know that mine is a product of the immeasurable support I have been blessed to receive throughout the years. To the individuals listed below, and to countless others who inspire and support me: thank you.

- **To my PI, Professor John Shepherd:** Thank you for supporting, challenging, and encouraging me to grow as a researcher and engineer. I am lucky to have had you as a mentor, from the first day we met at interview weekend. Thank you for providing me with the tools, time, and connections to succeed and for sending me around the world to share our work. I admire your intellectual vigor and excitement for new ideas, as well as your positivity and ability to enjoy life no matter how crazy it becomes.
- **To my advisors, Professors Steven Conolly, Christian Vaisse, and Christian Diederich:** Thank you for asking me the tough questions and giving me the honest answers. Your support has broadened my perspective to question and investigate everything (my own work included), and to see the bigger picture of how disparate fields come together for the betterment of human health. Thank you also for the fun talks, barbecues, and retreats that balance the long days in lab.
- **To my labmates, Jesus, Ben, Markus, Bo, Leila, En, Nisa, et al.:** Thank you for sharing this journey with me, through the long days when we didn't see the sun (quite literally). Thanks for all the laughs and celebrations, for the inside jokes and indoor basketball games. Thank you for teaching me things, sharing your lives, and supporting each other. While the lab has changed a lot since I joined, I'm excited for where we will all go.
- **To Ronald Yadon, Robert Mullins, Teresa Coda, Dr. Karen Jones, Jim McIntyre, Theresa Britschgi, Dr. Herbert Sauro, Dr. Wilbert Copeland, and Dr. Michael Kellen:** Thank you for inspiring me to study and pursue a career in science.
- **To my family:** Thank you for everything. For raising me, supporting me, and giving me opportunities, guidance, and love. Thank you for always being there for me, at home in Renton, down in the Bay Area, or anywhere in the world. For keeping together through daily messages and photos, and all of the big life decisions and events. You've supported me every step of the way and given me the space to grow.
- **To my friends, Olivia, Will, Daniel, Kristen, John, Phil, Andrea, Camilo, Matt, Elaine, Andrew, Yiqi, et al.:** Thank you for being my second family. For running races, cooking and sharing meals, and going on adventures near and far. For being there through the good times and the bad, for laughing, crying, and celebrating together. For playing basketball and making skits together. Thank you for making these last five years some of the best of my life.

Acknowledgements

Parts of this dissertation are reprints of materials that appear in several publications listed below. The co-author listed in this publication directed and supervised the research that forms the basis for the dissertation. Specific author contributions for each publication are provided.

1. B. K. Ng, B. J. Hinton, B. Fan, A. Kanaya, and J. A. Shepherd, “Clinical anthropometrics and body composition from 3D whole-body surface scans,” *Eur J Clin Nutr*, vol. 70(11), pp. 1265–70, Nov. 2016.

JAS and BKN designed and conducted the research; BKN, BJH and JAS analyzed data; BKN and JAS drafted the manuscript and had primary responsibility for final content. All authors reviewed and approved the final manuscript.

2. J. A. Shepherd, B. K. Ng, B. Fan, A. V. Schwartz, P. Cawthon, S. R. Cummings, S. Kritchevsky, M. Nevitt, A. Santanasto, and T. F. Cootes, “Modeling the shape and composition of the human body using dual energy X-ray absorptiometry images,” *PLoS ONE*, vol. 12, no. 4, p. e0175857, Apr. 2017.

JAS and TFC first conceptualized the manuscript. JAS, BKN, BF, and TFC designed and implemented the research project. JAS, BKN, and BF performed analysis. JAS and BKN wrote and edited the manuscript. All authors reviewed and approved the final manuscript.

3. B. K. Ng, Y. E. Liu, W. Wang, T. L. Kelly, K. E. Wilson, D. A. Schoeller, S. B. Heymsfield, and J. A. Shepherd, “Validation of Rapid 4-Component Body Composition Assessment using Dual-Energy X-Ray Absorptiometry and Bioelectrical Impedance Analysis,” *Am J Clin Nutr*, *In Review*.

BKN and JAS drafted the manuscript and had primary responsibility for final content. All authors reviewed and approved the final manuscript.

4. B. K. Ng, B. Fan, U. Lim, L. Le Marchand, L. Wilkens, and J. A. Shepherd, “Body shape and fat/lean distribution from whole-body DXA accurately predict metabolic syndrome across sex and ethnicity subgroups,” *Am J Clin Nutr*, *In Submission*.

BKN and JAS drafted the manuscript and had primary responsibility for final content. All authors reviewed and approved the final manuscript.

5. B. K. Ng, M. J. Sommer, Y. Nie, B. Fan, B. Bourgeois, C. Vaisse, B. Curless, S. B. Heymsfield, and J. A. Shepherd, “Improved Body Composition Prediction by Advanced 3D Optical Imaging Approach Compared to Conventional Anthropometry,” *Am J Clin Nutr*, *In Submission*.

BKN, MJS, SBH, and JAS designed and conducted research, performed analysis, and had primary responsibility for drafting the manuscript. YN, BB, and BF performed statistical analysis. All authors reviewed and approved the final manuscript. MJS and BKN contributed equally to this work.

Abstract

Despite tremendous progress in biological understanding of metabolic diseases and development of novel imaging techniques over the past several decades, clinical assessments and epidemiological studies for metabolic disease are largely limited to simple surrogate measurements such as body mass index. Recent advances in dual-energy X-ray absorptiometry (DXA) and 3D optical surface scanning have enabled new opportunities for integrative and clinically-accessible metabolic health assessment.

The focus of this dissertation was to develop novel 3D and DXA imaging methods for detailed metabolic risk assessment that are fast, safe, and accessible. This work centered on the hypothesis that detailed descriptors of body shape and compositional distribution of tissues throughout the body better reflect health risk than currently-used metrics.

I present derivation of high-resolution quantitative fat, lean, and bone images from DXA, and describe statistical appearance models of these images that can be used to accurately predict metabolic syndrome and diabetes status across ethnicities. I demonstrate clinically-viable body composition estimation from commercial 3D optical body scans using traditional anthropometric measurements, then improved accuracy and precision using more detailed 3D statistical shape models that efficiently capture 95% of body shape variance. Finally, I describe integrative methods including a combination DXA and bioelectrical impedance technique to provide rapid, accurate, and precise four-component (4C) body composition. 4C assessment is useful for monitoring of many metabolic conditions including over/de-hydration, malnutrition, obesity, and sarcopenia, and this technique enables practical implementation in the clinic.

These works collectively provide new tools to researchers, clinicians, and even individuals around the world to assess metabolic status and track, visualize, and predict personalized body changes towards improved health.

Abbreviations

- **3DO** three-dimensional optical
- **4C** four-component
- **ADP** air displacement plethysmography
- **AUC** area under the curve
- **BIA** bioelectrical impedance analysis
- **BMD** bone mineral density
- **BMI** body mass index
- **CT** computed tomography
- **%CV** coefficient of variation
- **D₂O** deuterium oxide
- **DXA** dual energy X-ray absorptiometry
- **FFM** fat free mass
- **FFMI** fat free mass index
- **FM** fat mass
- **FMI** fat mass index
- **ICP** iterative closest point
- **MAD** median absolute difference
- **MetS** metabolic syndrome
- **MRI** magnetic resonance imaging
- **PCA** principal component analysis
- **R²** coefficient of determination
- **RMSE** root-mean-square error
- **SAM** statistical appearance model
- **SEM** standard error of the mean
- **TBW** total body water
- **T2DM** type II diabetes mellitus
- **UWW** underwater weighing
- **VAT** visceral adipose tissue

Table of Contents

1 Background.....	1
1.1: Motivation: The Burden of Metabolic Disorders	1
1.2: Metabolic Syndrome.....	2
1.3: Diabetes.....	3
1.4: Sarcopenia, Cachexia, and Osteoporosis.....	5
1.5: Treatments and Solutions	9
2 Body Composition and Disease Risk.....	13
2.1: History	13
2.2: Multi-Component Models.....	14
2.3: Tissue Quality and Spatial Distribution	18
2.4: Technology Considerations.....	19
3 Body Composition Analysis Techniques.....	21
3.1: Classical Anthropometry.....	21
3.2: Total Body Density.....	23
3.3: Total Body Water	25
3.4: Dual Energy X-Ray Absorptiometry.....	29
3.5: Computed Tomography and Magnetic Resonance Imaging.....	30
3.6: Three-dimensional whole-body surface Imaging	32
3.7: Unmet Needs and Proposed Solutions.....	36
4 Advanced Techniques in DXA Body Composition.....	38
4.1: High-resolution 3-component DXA image separation	38
4.2: Statistical Appearance Models of 3D Body Shape and Mortality Risk	46
4.3: Body Composition Appearance and Metabolic Disease across Ethnicities	64
5 3D Surface Scanning for Metabolic Health Assessment	81
5.1: Clinical Anthropometrics from Commercial 3D Body Scanners	81
5.2: The Shape Up! Studies.....	95
5.3: Manifold Regression to Predict Compositional Shape Change.....	112
6 Novel Multi-Modality Clinical Assessment Techniques.....	115
6.1: Validation of DXA + BIA for Clinical 4C Body Composition Assessment	115
6.2: Ultra DXA + 3D Optical Imaging for True 3C and 4C Whole-Body Imaging.....	135
7 Future Directions.....	150

8 Conclusions	152
References	154
Appendix: Code Availability.....	169
Publishing Agreement	171

List of Tables

Table 2-1: Summary of multi-component body composition models. The components of each model sum to equal total body mass. Adapted from [46]......15

Table 3-1: Summary of body composition techniques and measurements. Cost, patient burden, accessibility, and specific diagnostic needs must be considered when selecting an appropriate measurement technique.....21

Table 4-1: Demographic characteristics of selected participants in HealthABC study.54

Table 4-2: Correlation coefficients for each principal component of the shape model versus demographic and anthropometric variables60

Table 4-3: Logistic regression equations for sex, race, and mortality60

Table 4-4: Demographic characteristics of the 1855 (916 male) participants included in this analysis. Continuous variables are reported as [mean (standard deviation)] unless otherwise noted......75

Table 4-5: Correlations between shape, texture, and appearance modes and metabolic markers of interest (male)76

Table 4-6: Correlations between shape, texture, and appearance modes and metabolic markers of interest (female)77

Table 4-7: Logistic regression equation performance for MetS and diabetes status as a function of fat shape, texture, and appearance modes. Data were randomly assigned to training (80%) or validation (20%) sets.78

Table 5-1: Summary statistics of the model calibration population and validation groups. Reported circumferences, areas, and volumes were derived from the 3D optical scans. Unpaired two-tailed t-tests were performed to detect significant mean differences in the direct 3D measurements between the two groups (P-values shown in the right-most column, * denotes $P \leq 0.05$). Note that body composition was measured using DXA on the calibration group and BIA on the validation group......90

Table 5-2: Test-retest precision of measurements derived from the 3D optical scanner. Each participant in the calibration data set was scanned twice, with repositioning......91

Table 5-3: Derived fat mass, fat free mass, and percent fat prediction equations from 3D optical measurements. Models were trained using gold-standard measurements from whole-body DXA scans. Whole-body models

were validated against an external dataset that included scale weight and bioelectrical impedance measurements. Parameters were selected to validate previous work by Lee, et al. (11, 18).92

Table 5-4: Subject Characteristics.101

Table 5-5: Correlation of principal modes to measurements, male.....102

Table 5-6. Correlation of principal modes to measurements, female.....105

Table 5-7. Predictions of body composition from 3D scans. Linear models were trained using 5-fold cross validation.....108

Table 5-8. Test-retest precision of body composition predictions from 3D scans109

Table 5-9: List of markers for 3D body scans. Adapted from [184]......112

Table 6-1: Summary demographic statistics of the 23 participants included in the present analysis (11 male). Total BMC, TBW, and Body Volume measures are reported from DXA, deuterium dilution, and air displacement plethysmography, respectively.121

Table 6-2: Test-retest precision for the BIA and DXA measurements utilized in the study. Duplicate measurements were collected using each modality, with repositioning. High variability in BIA Total Body Water measurements leads to imprecision in BIA fat mass and 4C DXA+BIA fat and protein masses. Removal of outlier BIA TBW measurements as described in the text results in significantly improved precision for each of those measurements.127

List of Figures

Figure 1-1: World Health Organization voluntary global targets for prevention and control of noncommunicable diseases to be attained by 2025. Source: [45]11

Figure 2-1: Graphical representation of the various components of the molecular level model of body composition. Source: [52].....16

Figure 3-1: Example of an underwater weighing apparatus. The subject rests on a seat connected to a force meter. The seat is lowered into the water until the subject is completely submerged, and her underwater weight is then measured. Image source: <https://education.uky.edu/khp/laboratories/exercise-physiology-lab/>.....24

Figure 3-2: The BOD POD (COSMED, Rome, Italy) air displacement plethysmography device for measuring body volume. Image source: <https://bit.ly/2KKrTZr>26

Figure 3-3: A clinical multifrequency segmental bioelectrical impedance analysis device with touch electrodes connected to the subject’s fingers and ankles. InBody S10 (InBody Co. Ltd., Seoul, South Korea). Image source: <http://www.inbody.com/global/product/inbodys10.aspx>.....28

Figure 3-4: A dual energy X-ray absorptiometry scanner. GE iDXA (GE Healthcare, Madison, WI). Image source: <https://bit.ly/2ws7DJ5>.....30

Figure 4-1: Principle of DXA. High and low energy X-ray attenuation profiles *A_{high}* and *A_{low}* are measured simultaneously. Different materials have different attenuation profiles by X-ray energy level. The ratio of specific mass attenuation coefficients (in cm^2/g) at low and high energies are used to determine *k_{bone}* and *k_{soft}* coefficients that allow for isolation of bone and soft tissue masses, respectively. Adapted from [131].38

Figure 4-2: The “R-factor” ratio between low- and high-energy X-ray attenuation can be used to estimate fat/lean composition of soft tissue. For DXA, beam hardening effects with increased thickness produce a nonlinear relationship which requires multi-point calibration using soft tissue phantoms. Adapted from [130].39

Figure 4-3: Example of soft tissue interpolation required in DXA scans. The image on the left from a GE scanner and the image on the right is from a Hologic scanner (courtesy of Joseph P. Wilson).....41

Figure 4-4: High-energy air-phase images extracted from a whole-body DXA scan. The image on the left is the raw data extracted from the scan file, and the image on the right is an interleaved, upscaled version that uses all three bone/soft tissue/air phase images from the Hologic internal reference system.42

Figure 4-5: Quantitative 2C and 3C image extraction from whole-body DXA scan files. High- and low-energy X-ray attenuation maps are extracted from Hologic scan files (left group). Simple 2C subtraction assuming fixed soft tissue composition produces detailed bone and soft tissue mass images (middle group). 3C modeling

of variable soft tissue composition using the Hologic internal reference system enables calculation of bone, fat, and lean mass images.43

Figure 4-6: Regression plots for whole-body fat, lean, and bone mass as measured by the 3c_dxa algorithms (y-axes) compared with Hologic report values (x-axis). Hologic fat and lean values were calculated with the NHANES calibration enabled [132].45

Figure 4-7: Annotation schemes and triangulations for texture warping. A full-body shape model containing 82 annotation points was initially developed. To eliminate spatial noise introduced by pose variation, a 52-point subset model was created that excludes the forelimbs and head.50

Figure 4-8: Mean images created with the 200 R-value images. Images were calculated using alignment with (a) translation, (b) translation, rotation, and scaling (affine), and (c) piecewise warping using the triangle model in Figure 4-7. Each successive mean image is visually sharper than the last, indicating that the more advanced alignment techniques are more effective at eliminating noise from shape and pose variation. ..51

Figure 4-9: Shape only modes (first 6). For each mode, the ± 3 standard deviation (left and right respectively) images are shown. 23 modes were required to explain 95% of shape variance. At a high level, we see that body height is captured in Mode 1, width in Mode 5, and android/gynoid shape variation in Mode 2. Note that several modes capture variation in subject pose.55

Figure 4-10: Texture only modes (first 6). For each mode, the ± 3 standard deviation (left and right respectively) images are shown. 261 modes explained 99% of the variance. Since this model captures only texture information, all images have the same shape, but differing grayscale intensity indicating different distributions of tissues throughout the regions of the body.56

Figure 4-11: Combined appearance modes (first 6). For each mode, the ± 3 standard deviation (left and right respectively) images are shown. 237 modes explained 99% of the variance. This model captures dominant modes of variation in both texture and shape.57

Figure 4-12: The first 8 appearance modes for a SAM of solid body thickness (lean + fat thickness) and 52-point annotation. (± 3 SD). We see significant differences in body shape roughly corresponding to weight, height, and sex in Modes 1, 2, and 3, respectively. Again, pose variation is captured in multiple modes.58

Figure 4-13: Hybrid model of shape, thickness, and leanness including bone. Total thickness is represented by green intensity and %lean by red intensity. (± 3 SD). Mode 1 captures dramatic body shape and composition variance ranging from a high-lean, low-thickness (thin) phenotype to a low-lean, high-thickness phenotype.58

Figure 4-14: Linear regression models of sex and ethnicity using the combined appearance model of Leanness + Thickness images (± 3 S.D.s). There were 3 appearance modes used in the sex model that achieved an AUROC of 0.99. There were 6 appearance modes used in the Race model that achieved an AUROC of 0.91.

These models show that statistical appearance of body shape, thickness, and leanness accurately identifies sex and race differences in the sample population.....59

Figure 4-15: Linear regression model of mortality status using the combined appearance model of Thickness images (± 3 S.D.s). There were three appearance modes used in the model that achieved training AUC of 0.66 and validation AUC of 0.62. In the difference image, green indicates greater thickness in the low-risk image and red indicates greater thickness in the high-risk image.61

Figure 4-16: Schematic representation of the Statistical Appearance Modeling approach utilized in the present study.67

Figure 4-17: Mean body mass index and fat/lean composition by sex/ethnicity subgroup.....70

Figure 4-18: Weighted mean statistical texture of whole-body DXA fat by sex and ethnicity. The mean fat texture of each subgroup is shown relative to the overall means across all ethnicities. Marked differences, particularly in the trunk and leg regions, are apparent. Notably, fat distributions for each ethnicity are consistent across sexes.72

Figure 4-19: Weighted mean statistical texture of whole-body DXA lean by sex and ethnicity. The mean lean texture of each subgroup is shown relative to the overall means across all ethnicities.73

Figure 4-20: Estimated risk of MetS for each sex/ethnicity subgroup. These estimates were created by applying the logistic regression models (Table 4-7) to the weighted subgroup means of BMI, shape, and fat appearance (texture image shown in Figure 4-18 and Figure 4-19). Estimates were compared to actual observed prevalence of MetS (grey columns on left chart). It can be seen that fat appearance models produce lower RMSE in MetS risk estimates than corresponding body shape and BMI models, supporting the idea that fat appearance holds metabolically significant information beyond traditional shape descriptors.....74

Figure 5-1: 3D scanner body circumferences and surface area vs. criterion methods. Clockwise from top left: hip circumference, waist circumference, and body surface area comparisons, then sample matched DXA and 3D optical images with annotated landmarks. 3D circumferences and surface area show high correlation with manual tape measures. Biases may be the result of non-identical landmark positioning between the methods. Of note, body surface area shows significant bias that may be explained by the fact that the 3D scanner software does not report surface area of the head and neck. This omission is not a technical shortcoming, but a design decision by the manufacturer to avoid inaccuracies introduced by voluminous hair.88

Figure 5-2: 3D scanner body volume vs. criterion methods. Clockwise from top left: total volume vs. ADP and DXA, arms vs. DXA, legs vs. DXA, and trunk vs. DXA. High precision and accuracy is observed for whole-body volume. Due to differences in partition locations, regional measurements are not directly comparable between the 3D scanner and DXA. For instance, the legs are partitioned horizontally at the crotch in the 3D optical system, but diagonally from the crotch up to the top of the hip in the DXA system.

Consequently, reported leg volumes are lower on the 3D system than the DXA system. Refinement of the regional partitions is necessary before cross-modality comparisons can be performed.89

Figure 5-3: The first 12 principal components that captured 95% of shape variance in males. Each component displays -3 SD to the left and +3 SD to the right.103

Figure 5-4: The first 9 principal components that captured 95% of shape variance in females. Each component displays -3 SD to the left and +3 SD to the right.104

Figure 5-5: Annotated 3D body scan with 75 landmarks shown. Mesh annotation and visualization was performed in MeshLab version 1.3.2.111

Figure 5-6: Predicted 3D body shape changes for individual male (left) and female (right) participants. Actual participant scans are shown in the middle of each set. Height and age were held constant while fat mass and lean mass, were varied independently using manifold regression. Numbers next to each body represent BMI.114

Figure 6-1: Linear regression between body volume measurements from DXA and ADP (n=23). High correlation was observed, though a slope significantly different from 1 was detected. These data were used to determine a linear correction equation for body volume from DXA: $BV_{ADP} = 0.993 BV_{DXA}$ (95% CI: [0.990, 0.996]). The dashed line is the line of identity.122

Figure 6-2: Linear regression between total body water measurements from BIA and D2O (n=23). High correlation was observed, though a slope significantly different from 1 was detected. These data were used to determine a linear correction equation for total body water from BIA: $TBW_{D2O} = 0.956 TBW_{BIA}$ (95% CI: [0.932, 0.979]). The dashed line is the line of identity.124

Figure 6-3: Linear regression between whole-body percent fat from the 2-, 3-, and 4-component body composition assessment methods in this study versus the reference 4C Lohman model (n=23). “n.s.” indicates that the regression intercept was non-significant (P > 0.05) and set to zero.125

Figure 6-4: Linear regression of whole-body 4C residual protein measured by DXA+BIA method versus Lohman reference method (n=23). The equation for the line of best fit is $Prot_{DXA+BIA\ 4C} = 0.99 Prot_{Lohman\ 4C}$ (95% CI: [0.93, 1.05]). The dashed line is the line of identity.126

Figure 6-5: Histograms of fat-free mass hydration (defined as total body water divided by fat-free mass from DXA) (n=23). More variance was observed when using BIA for TBW than when using D2O for TBW. The observed range of hydration values extends beyond physiological bounds for healthy adults in the sample; definition of thresholds on plausible hydration levels may provide criteria to validate BIA TBW measurements.128

Figure 6-6: Whole-body percent fat from various body composition assessment methods versus the reference 4C Lohman model. “n.s.” indicates that the regression intercept was non-significant and set to zero. This figure matches Figure 3 but includes DXA percent fat with NHANES correction enabled. It can be seen that

DXA (NHANES) significantly overestimates percent fat versus all other methods tested, particularly in leaner individuals.....	134
Figure 6-7: DXA can simultaneously resolve two tissue compartments (bone and homogenous soft tissue, left), but not three (bone, lean, and fat). Consequently, soft tissue composition must be interpolated in all pixels containing bone (right).....	135
Figure 6-8: Prototype Ultra DXA system with integrated transparent acrylic tabletop and 3D depth cameras. ...	139
Figure 6-9: Blue wax/plastic water step phantom on Delrin sheets used to approximate water, lipid, and protein, respectively.	139
Figure 6-10: Isolated water, lipid, and protein images of the step phantom generated using the 3C “Ultra DXA” technique. High-resolution DXA attenuation measurements and known thicknesses were used to derive cubic polynomials to estimate water, fat, and protein composition. Cross-sectional thickness profiles are shown below each image, showing good agreement to the actual dimensions of the step phantom.	141
Figure 6-11: Effect of averaging multiple 3D optical depth measurements. We found that averaging of approximately 20 depth measurements reduced error below 0.5 mm.	143
Figure 6-12: Two examples of assembled 3D meshes from depth images collected from a single depth camera over a single pass of the densitometer C arm. Images were collected approximately every 3 seconds and assembled using the Iterative Closest Point algorithm. The presence of many well-defined depth features (e.g. corners and ridges) is necessary for ICP to produce reliable alignments. Smaller participants with less shape features or smaller bodies may prove more problematic for alignment particularly near the feet end of the scanner and between scan passes.	145
Figure 6-13: Challenges in alignment of 3D depth images. In regions with few distinct depth features (e.g. the near the feet shown at left), there may be insufficient correspondence for reliable alignment. One failed image alignment can then cause subsequent images to align incorrectly. Timing information can be used with the known movement of the densitometer to predict the exact location at which each image was taken (right).....	146

1 | Background

1.1: Motivation: The Burden of Metabolic Disorders

Obesity is a global epidemic that affects 650 million adults worldwide [1]. Characterized by an excess of adipose tissue in the body, obesity is significantly associated with a host of diseases such as diabetes, heart disease, and stroke, and responsible for some 2.8 million deaths annually [2]. Despite significant research, education, and policy efforts, obesity prevalence continues to rise around the world, with particularly stunning increases in children [3], [4]. Obesity is estimated to cause approximately 4% of cancers in men and 10% of cancers in women [5]. As of 2008, medical costs associated with obesity were estimated at a staggering \$147 billion [6]. By 2030, it is estimated that 50% of American adults will be obese [7], and related medical costs will account for 18% of all US healthcare expenditures [8].

There are several contributors to the rise of the obesity epidemic. At a basic level, fat accumulation occurs with a net positive energy balance, where calories consumed but not expended are stored in adipose tissues [9]. At a societal level, the proliferation of inexpensive, energy-dense, and often sugary foods coupled with general trends towards physical inactivity and increasingly sedentary lifestyles are highly conducive to obesity [10]. There is increasing evidence that gut microflora, genetics, epigenetics, sleep patterns, and a variety of other factors may contribute to obesity [11]. Whatever the case, it is clear that significant work must be done to curb and reverse the obesity crisis.

Obesity is defined as an abnormal and excessive accumulation of fat tissue, but it is an indicator of complex underlying metabolic imbalances. In practice, obesity is classified using the crude metric

of body mass index (BMI) that is only a surrogate for body fatness. BMI fails to account for actual differences in fat and lean tissue [12], and its generalizability to people of different ages and ethnicities has been shown to be limited without statistical adjustments [13]–[15]. Nonetheless, BMI and similarly simple metrics such as waist circumference remain the primary tools broadly available in clinical practice and epidemiological research. There is clear opportunity and need for more sophisticated yet accessible tools for metabolic health assessment. The focus of this dissertation research was to develop novel tools and techniques for accurate and precise metabolic health assessment that can be readily implemented in clinical and population research settings.

In the following sections of this chapter, several prominent metabolic disorders will be detailed, along with a discussion of clinical tools for diagnosis and management.

1.2: Metabolic Syndrome

Broadly, metabolism refers to the conversion of energy through various chemical transformations to sustain life. Human metabolic disorders, then, are dysfunctions somewhere in the complex biochemical processes, tissues, and systems that extract energy from nutrient intake. Several different measurable biomarkers of metabolism have been identified as significant risk factors for diseases such as diabetes, heart disease, and stroke, which ultimately lead to decreased quality of life and early death.

Metabolic Syndrome (MetS) has been defined using a particular set of risk factors that directly promote disease: abdominal obesity, hypertension, hyperglycemia, and dyslipidemia. Several organizations such as the International Diabetes Foundation, the World Health Organization, and

the American Heart Association have offered various guidelines for specific diagnosis of MetS [16], [17]. The consensus National Cholesterol Education Program and American Heart Association guidelines [17], [18] classify MetS as the presence of three or more of the following:

- Abdominal adiposity: waist circumference >40 inches (men) or > 35 inches (women)
- Elevated blood pressure: > 130/85 mm Hg, or medication
- Elevated fasting glucose: ≥ 100 mg/dL, or medication
- Elevated serum triglycerides: >150 mg/dL, or medication
- Reduced HDL cholesterol: <40 mg/dL (men) or <50 mg/dL (women), or medication

Metabolic syndrome represents a clustering of endogenous risk factors associated with obesity, atherosclerotic cardiovascular diseases, and diabetes, and conducive to inflammation and thrombosis. The particular manifestations of MetS are known to vary among individuals, particularly across different ethnicities [18]. Ongoing research is being performed to determine appropriate therapeutic strategies for individuals with MetS.

1.3: Diabetes

Diabetes mellitus is a metabolic disease estimated to affect 422 million adults worldwide and cause 1.6 million deaths annually. The disease is characterized by chronically elevated glucose in the blood, generally resulting from either insufficient insulin production by the pancreas (Type I diabetes, T1DM), or a developed resistance to insulin (Type II diabetes, T2DM). In either case, elevated blood sugar for prolonged periods of time can lead to a host of systemic issues including heart disease, kidney failure, loss of vision, and nerve damage [19].

Clinical diagnosis of diabetes, as defined by the World Health Organization, requires one of the following positive tests:

- Fasting plasma glucose ≥ 126 mg/dL
- 2-hour plasma glucose ≥ 200 mg/dL
- HbA1c $\geq 6.5\%$

Fasting glucose indicates a baseline blood sugar level long after a meal, while a 2-hour glucose test indicates the body's ability to respond to glucose load. The fasting glucose cut-point of 126 mg/dL was identified as a threshold for specific micro-vascular complications such as retinopathy, but systemic risks increase even at lower sustained fasting glucose levels. Glycated hemoglobin (HbA1c) is a more long-term indicator of blood glucose levels that is insensitive to immediate fasting state. Compared to plasma glucose levels, HbA1c has been shown to be a stronger predictor of cardiovascular disease and death [20].

Type II diabetes, formerly known as “adult-onset diabetes” represents 90% of all diabetes cases. Overweight and obesity are the strongest known risk factors for T2DM, and the rise of the childhood obesity epidemic has resulted in a concurrent rise in childhood T2DM that has rendered the “adult-onset” label inaccurate. Prevalence of T2DM has shown particular growth in low- and low-middle income countries. In the Eastern Mediterranean region, prevalence of diabetes increased from 5.9% in 1980 to a whopping 13.7% in 2014 [21]. Trends in physical activity and food availability – particularly the growth of inexpensive, calorie-dense sugary and fatty foods – have created conditions highly conducive to obesity and diabetes.

There are several ongoing efforts to curb the rise and effects of diabetes. At the individual level, people living with diabetes must regularly monitor their blood sugar levels, commonly using finger prick blood tests throughout the day. Health education and lifestyle counseling, targeted at improved diet and activity patterns, as well as medications such as insulin or hypoglycemic agents are the direct methods for diabetes treatment. Integrated treatment to target associated risk factors such as high blood pressure include other medications such as diuretics and ACE inhibitors [22]. More drastic treatments such as bariatric surgery to reduce energy intake have been shown to be effective for combating severe obesity-related T2DM [23]. At the population and public health level, educational programs to increase awareness about healthy lifestyles and diabetes risks, as well as regulatory measures to limit food high in sugars, fats, and salt are core efforts to combat diabetes. Sugar-sweetened beverage taxes have been shown to be effective at limiting consumption, particularly in young people [24], [25].

As a growing global epidemic, it is encouraging to see that 72% of countries around the world have a specifically funded national program to address diabetes. The causes and effects of diabetes are complex, but a commitment to understand the mechanisms of disease and identify multifaceted treatment and prevention strategies can significantly counteract the rise of diabetes and improve overall metabolic health in societies around the world.

1.4: Sarcopenia, Cachexia, and Osteoporosis

While obesity – an excess accumulation of adipose tissue – is perhaps the most visible disorder of human metabolism, disorders of muscle and bone tissue represent significant risks for loss of function, falls and bone fracture, disability, and death. These diseases significantly can affect quality

of life, limiting one's ability to perform activities and tasks, or in cases of traumatic fracture, necessitating a loss of independence.

Sarcopenia is defined as a loss of skeletal muscle mass and strength associated with aging. The Greek roots of the term "sarcopenia" literally translate to "flesh loss". While it is widely (and intuitively) known that aging is associated with wasting and loss of strength, work towards consensus definition of the disease is ongoing. The European Working Group on Sarcopenia in Older People (EWGSOP) diagnoses sarcopenia as the presence of at least two of the following conditions [26]:

- Low muscle mass
- Low muscle strength
- Low physical performance

The EWGSOP provides recommended methods and tests for measuring muscle mass, strength, and performance. There are currently several proposed cut-off points for classification of each. Nonetheless, a new ICD-10 code for sarcopenia was officially introduced in 2016 [27], representing a key milestone supporting ongoing sarcopenia research and development of targeted therapies. Current research efforts for sarcopenia treatments focus on development of nutrition plans with specific macronutrient targets, and development and validation of physical activity regimens and medications that are effective for improvement and maintenance of strength and functional ability.

Cachexia is a closely-related general wasting condition in which muscle mass is lost and often energy intake is reduced, generally accompanying diseases such as cancer, HIV/AIDS, and end-stage renal disease [28]. Most individuals with cachexia are also sarcopenic, due to the significant loss of

muscle mass, but most individuals with sarcopenia are not cachectic (since low strength and functional performance can be observed in the absence of dramatic loss of muscle mass) [26]. Indeed, it has been shown that strength, but not muscle mass is associated with mortality in an older cohort [29], suggesting that muscle quality can be just as important as muscle mass to physical function and ability [30].

Osteoporosis – literally “porous bones” in Greek – is a disease in which bone strength has dropped significantly and risk of fracture is elevated. It is estimated that some 200 million people worldwide have osteoporosis, and 8.9 million osteoporotic fractures occur per year [31]. The disease affects more women than men, with particularly significant loss of bone strength observed after menopause. Osteoporosis is often called a “silent disease” because there are generally few visible symptoms until a fracture occurs. Fractures significantly affect quality of life and lead to significant pain, loss of independence, institutionalization, and death.

The gold standard for diagnosis of clinical osteoporosis is measurement of areal bone mineral density (BMD) using dual energy X-ray absorptiometry (DXA). A person is classified as osteoporotic if his or her BMD is less than or equal to 2.5 standard deviations below reference values for a healthy 30-year old adult [32]. The WHO international standard site for diagnosis is the femoral neck, but the International Society for Clinical Densitometry recognizes low BMD measurements at any of the lumbar spine, total hip, or femoral neck (and in some cases the forearm) for diagnosis of osteoporosis in postmenopausal women and men over the age of 50 [33]. The FRAX fracture risk assessment tool was created using several population-based cohorts around the world to predict individual 10-year

fracture risk based on several established risk factors. Several different versions of the tool exist with specific calibrations for different ethnicities and regions [34].

While bones are generally thought to be relatively static compared soft tissues in the body, bone tissues are constantly being resorbed and reformed. In addition to macroscopic bone density (which is dominated by mineralized exterior cortical bone), it has been shown that microscopic trabecular structure within the bone significantly affects overall bone strength [35], [36]. Medications for osteoporosis target various mechanisms of bone formation and turnover [37] – bisphosphonates (which cause cell death of the osteoclasts that destroy bone tissue), rank ligand inhibitors (which suppress the development of osteoclasts, and hormone replacement (e.g. estrogen for postmenopausal women) are the major classes. Nutrition and lifestyle interventions to promote bone health are also major components of osteoporosis treatment plans.

As muscle and bone are tightly integrated, it is not surprising that osteoporosis and sarcopenia are often associated conditions. They are key predictors of frailty – a phenotype defined by low strength and activity, slowness and exhaustion, and unintentional weight loss [38], [39]. Diverse and ongoing loading of bone, mediated by applied muscle forces, is necessary to maintain BMD and structural integrity. Resistance training, and in particular impact training, have been shown to increase muscle strength and bone density [40]. Indeed, there is a growing body of biochemical research evidence for an integrated “bone-muscle unit” with numerous biological interconnections and constant “cross-talk” [41]. Identification of underlying biochemical pathways provide more holistic targets for improvement of bone and muscle health simultaneously.

Obesity, sarcopenia, and osteoporosis each present significant challenges to health and quality of life. However, some individuals face a concomitant double- or triple-burden of two or three of these diseases. In such individuals, risks are elevated and outcomes are worse than in individuals with only one of these diseases alone [42]. Whereas obesity has generally been shown to be protective towards bone health (due to increased basal loading, or impact protection), individuals with sarcopenic obesity see compounding effects of metabolic risk [43]. The interplay between bone, muscle, and fat tissues in the body, and the cross relationships with insulin resistance, inflammation, and blood lipids underscore the complex nature of human metabolism, and the need for integrative research towards effective treatments.

1.5: Treatments and Solutions

The burdens of metabolic disorders are clear. Economic, societal, and individual costs of obesity, diabetes, osteoporosis, and associated diseases continue to grow. Combating these trends requires effective individual treatment options as well as broader public health initiatives.

At the individual level, lifestyle changes focused on improved diet and physical activity regimens are the first line of treatment. Caloric restriction and physical training plans designed to target a 500- to 1000-calorie deficit per day are recommended, with a broader aim of losing 7-10% of body weight within 6 to 12 months [18]. Macronutrient recommendations include 25-35% of calories from all fats, including mostly unsaturated fats, <7% of total calories from saturated fat, and minimal trans-fats. Simple sugars should be limited. Alcohol and sodium consumption should also be limited to mitigate hypertension. There is conflicting evidence on the long-term efficacy of low-carbohydrate / high-fat diets, with some evidence for effectiveness in short-term weight loss (but not

long-term maintenance), at a cost of undesirably high fat intake and limited vegetable intake. It is generally agreed that an emphasis on fresh fruits and vegetables and low-fat dairy products is beneficial. There is growing evidence that a Mediterranean diet rich in plant-based foods, vegetable oils, and whole grains, an emphasis on fish and poultry over red meats, limited salt is effective at reducing cardiovascular disease risk and overall mortality [44]. Vigorous activity of at least thirty minutes per day is recommended most if not all days of the week for all individuals. Increased targets of 60 minutes of aerobic activity every day are recommended for individuals with MetS aiming to lose significant amounts of body weight [18].

Pharmacologic treatments for dyslipidemia include fibrate, nicotinic acid, and statins to improve lower LDL and triglyceride levels. For prediabetic and diabetic individuals, drugs that stimulate insulin production and inhibit sugar absorption are available, including metformin, thiazolidinediones, and acarbose, along with direct insulin treatments. Low dose aspirin is recommended to limit risk of thrombosis. ACE inhibitor and diuretic medications are recommended address hypertension [18].

More broadly, the WHO has created a global action plan to address the burdens of non-communicable diseases (NCDs) such as cardiovascular disease and diabetes [45]. The plan involves recommendations for sweeping multi-sector political and public health efforts at regional, national, and global levels to create systems and environments to improve health and lower prevalence of NCDs across people of all ages, socioeconomic statuses, and regions. The plan defines nine high-level voluntary global targets for prevention and control of noncommunicable diseases to be attained by 2025 (Figure 1-1).

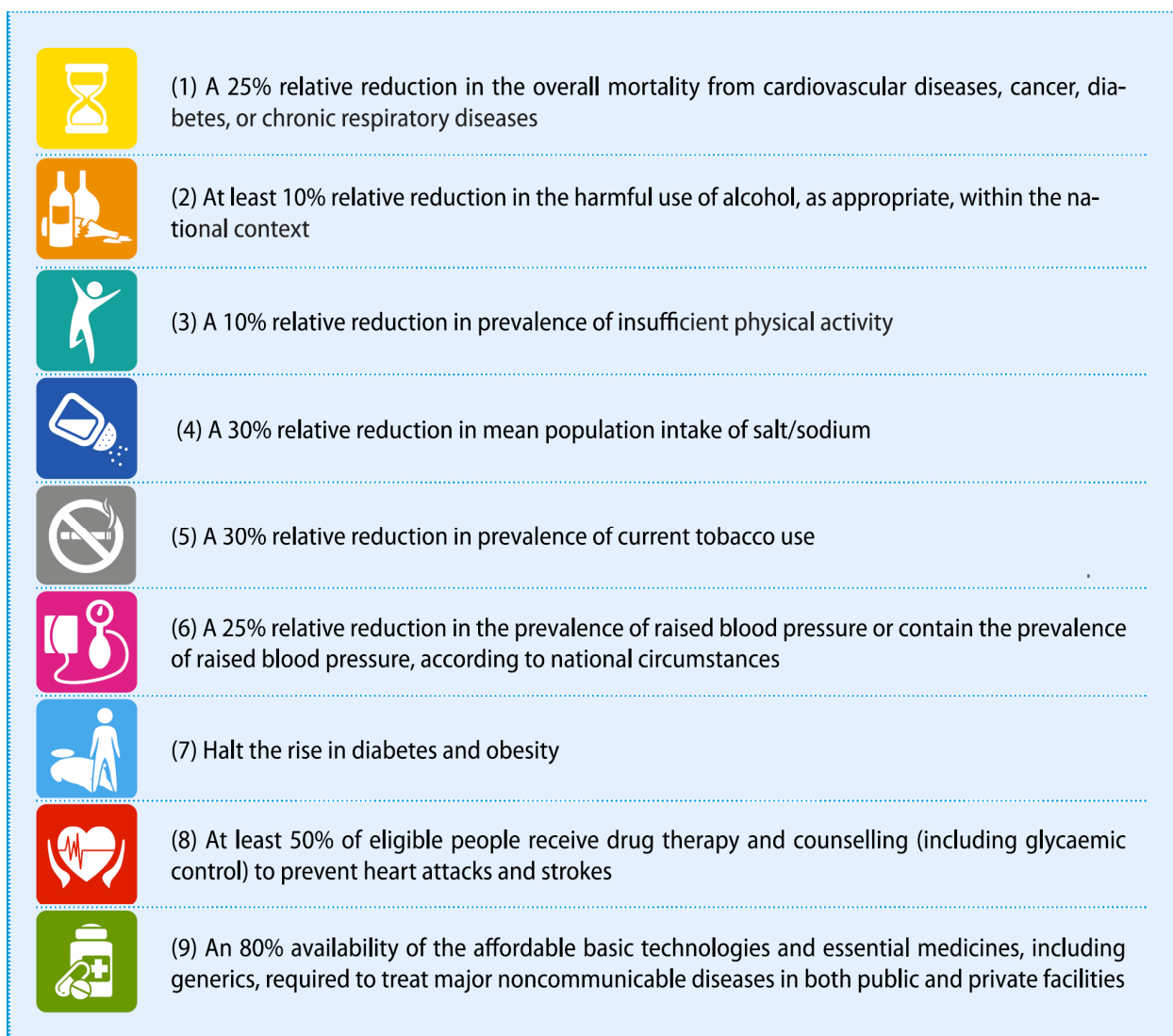


Figure 1-1: World Health Organization voluntary global targets for prevention and control of noncommunicable diseases to be attained by 2025. Source: [45]

The plan focuses on (1) raising awareness and urgency of public initiatives and advocacy efforts to address NCDs, (2) creating health-promoting environments to reduce modifiable risk factors at the population level, (3) strengthening healthcare systems and coverages to ensure access to treatment, (4) supporting research and development for prevention and control of NCDs, and (5) monitoring trends and evaluating progress in addressing the burden of NCDs worldwide. The plan emphasizes human rights and equity, recognizing that these diseases are global problems that require multi-level solutions that are safe, accessible, and culturally sensitive, and that global progress to

improve metabolic health worldwide requires broad cooperation across sectors. These efforts can include thoughtful taxation and regulation on food advertising, alignment of food production incentives with evidence-based research and population health goals, support of fundamental research to better understand metabolic health, and dissemination of the latest knowledge, diagnostics, and treatments to healthcare providers and systems around the world.

2 | Body Composition and Disease Risk

The tissue composition of the body is a long-term reflection of a person's accumulated nutrient intake, physical activity patterns, and overall health status. There are many levels of description for body composition, from elements to tissues, to organs. Body composition research at these various levels allows us to understand the metabolic processes of the body and how they become disturbed in disease states. Metabolic diseases, whether specifically defined by a macroscopic indicator (as excess adiposity defines obesity), or by particular blood markers (as blood glucose levels define diabetes), have specific compositional signatures. Thus, human body composition provides powerful indicators of metabolic state and dynamics, and the study of body composition provides clinicians with tools to diagnose and monitor metabolic disease and treatments.

2.1: History

Conceptually, body composition dates back to ancient Greece around 400 BCE [46]. The Greeks believed that the human body was fundamentally made of the cosmic elements of fire, earth, air and water. Contemporary body composition research began with foundational research in the 1850s identifying and relative amounts of protein, fat, salts, and water in the body. L.A.J. Quintlet in 1871 defined Quintlet's index as body weight over height squared – the precursor to body mass index (BMI) as we know it today. Advancing technologies such as the development of stable and radioactive isotopes and conceptual metabolic models around the 1930s ushered in a “golden era” of body composition research. Underwater weighing, whole-body labeled potassium counting, and neutron activation analysis techniques were all introduced to measure body volume, fat and lean

mass, and protein. Body composition imaging techniques such as DXA, computed tomography (CT), and magnetic resonance imaging (MRI) were introduced in the 1970s and 1980s, providing not just quantification of total body composition, but also regional composition and rich 2D and 3D visualizations of tissue distributions in the body. Many large studies such as the National Health and Nutrition Examination Survey in the United States have been created that include various body composition measurements [47]. Such studies provide reference data to establish normative compositional benchmarks and track overall population health over time.

2.2: Multi-Component Models

There exist several different conceptual models for human body composition. The body can be divided into elements, molecules, cells, tissues and organs, or regions [46], [48]. Shen and Wang summarized these models and their constituent components as shown in Table 2-1. Within each of these model levels there may be multiple different particular models with differing numbers of components. Models with fewer components necessarily group smaller components into larger ones – for example the two-component molecular model contains fat mass (FM) and fat free mass (FFM), where FFM contains protein, mineral, and carbohydrate. The two-component molecular model is widely used due to its simplicity and direct connection to metabolism: FFM encompasses “actively metabolizing” tissues and FM represents energy storage.

Table 2-1: Summary of multi-component body composition models. The components of each model sum to equal total body mass. Adapted from [46].

Model Level	Components	Number of Components
Atomic	Hydrogen, oxygen, nitrogen, carbon, sodium, potassium, chlorine, phosphorous, calcium, magnesium, sulphur	11
Molecular	Lipid, water, protein, mineral, carbohydrate	2-6
Cellular	Cells (adipocytes and others), extracellular fluids, extracellular solids	3-4
Tissue-Organ	Adipose tissue, skeletal muscle, bone, visceral organs, other tissues	5
Whole-Body	Appendages, trunk, head	3

The various model levels of body composition analysis have conceptual and historical underpinnings. While the different models and levels are closely related, it is not always possible to draw direct correspondences between components. For example, lipid and fat are often discussed interchangeably, but there is a small amount of lipid mass found in lean tissues. Furthermore, the term “lean tissue” is not equivalent to “fat free mass” despite similar conflicting usage in practice and in the literature [46]. Bazzocchi visualizes the subtle differences in these molecular body composition components graphically in Figure 2-1. Appropriate model selection is dependent upon the availability and practicality of measurement techniques, the outcome measurement of interest, and the overall purpose for composition analysis.

Chemical analysis of human cadavers is perhaps the most precise way to quantify body composition [49], though this is for obvious reasons impractical for health assessment. Perhaps the first practical *in vivo* body composition analysis technique was Behnke’s two-component (2C) underwater weighing method introduced in 1942 [50]. This method relies on direct measurements of weight in and out of water to estimate body volume and density. Using assumed densities of fat and fat-free tissues, the relative masses of those components can be calculated [51]. This method is

simple and elegant, but it necessarily obfuscates much compositional detail in assuming fixed densities of summed “fat free” mass.

MOLECULAR level

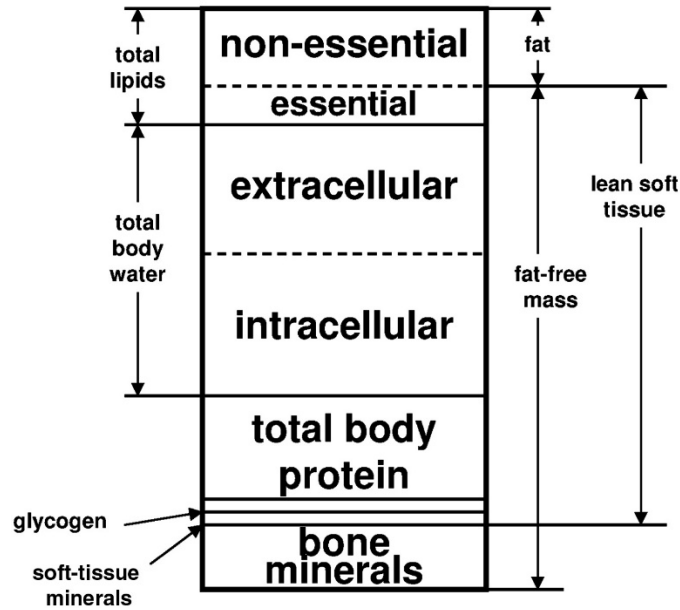


Figure 2-1: Graphical representation of the various components of the molecular level model of body composition. Source: [52]

The major components of fat free mass are water, protein, minerals, and glycogen. While in many cases, the relative composition of these components may be relatively stable, it has been shown that variability is observed depending on several factors including fasting status, growth, pregnancy, race, and disease [53]. To address this, Siri proposed a three-component (3C) model separating “fat free mass” into water and non-fat solids (protein, minerals, and glycogen). This was enabled in 1950 by the introduction of isotopic water dilution techniques to measure total body water [54]. In these measurements, a subject consumes a small dose of stable isotopic water (e.g. deuterium). The dose is allowed to equilibrate over the course of a few hours. Water samples (either urine or saliva) are

collected throughout the process and analyzed for dose concentration to calculate the size of the total body water pool.

The effort to further quantify specific “residual mass” components was boosted in 1963 with the introduction of single-photon absorptiometry (SPA) as a method for quantification of bone mineral mass [55]. This enabled a four-component (4C) model including fat, water, mineral, and residual protein (+glycogen) masses that was used by Selinger [56] to accurately quantify body composition in children, whose fat-free mass composition was not accurately represented by the stable assumptions calculated on adults.

Notably, SPA bone mineral measurements were only reliable at bony sites free of significant overlying soft tissue. The development of dual-photon absorptiometry (DPA) [57] and then DXA [58] in the 1980s surmounted this issue by enabling simultaneous quantification of bone and soft tissue mass at different locations throughout the body. While it should be recognized that these dual-energy techniques must assume fixed density of soft tissue, the density of bone mineral is so significantly higher that calculated bone mineral content is relatively insensitive to small changes in assumed soft tissue density.

Fundamentally the development of these 2C, 3C, and 4C models rely upon accurate measurement of body mass and volume to attain density. Additional material-specific measurements (e.g. body water and mineral mass) are added to precisely fix certain components and allow for calculation of increasingly specific residual mass. Five- and six-component models were recently described by Wang [59] and others that separate mineral into osseous and soft tissue components,

then a separate glycogen component [53], but these models remain relatively limited in practice due to their inherent complexity.

Over the past few decades there has been significant development in techniques for measuring molecular-level body composition for research, clinical, and even consumer applications [53]. While improved accessibility and availability of body composition analysis is undoubtedly positive for management of metabolic health and disease around the world, the proliferation of different techniques underscores the need for appropriate reference standards and calibration to ensure accurate risk assessment and clinical interpretation.

2.3: Tissue Quality and Spatial Distribution

Whole-body bone mineral density is known to be a significant predictor of bone fracture risk, but it is not utilized in clinical practice for diagnosis of osteoporosis. Rather, site-specific bone density at the hip, spine, and forearm are officially recommended by the International Society for Clinical Densitometry [60]. It is intuitive that site-specific bone structure and density would better predict fracture than whole-body metrics given that bone fractures are mechanical failure events that occur at specific locations where an applied force exceeds the capacity of a specific bone. The local density of bone, as well as the spatial distribution of cortical and trabecular bone, each provide additional information towards prediction of fracture [61]–[64].

A growing body of evidence shows that local information about tissue quality and spatial distribution is similarly powerful for assessing metabolic risk from body composition. Muscle quality, as quantified by intra- and inter-muscular fat using Computed Tomography, is more

predictive of functional strength than muscle mass alone [65], [66]. This is particularly important because muscle strength, but not mass, has been shown to predict mortality in older adults [29], despite the fact that strength is notoriously difficult to measure with high precision [67]. Passive methods for assessment of muscle quantity and quality may offer stronger predictors of functional ability, fall risk, and mortality. The spatial distribution of fat tissues throughout the body has been shown to have a significant effect on metabolic risk. For example, visceral fat has been shown to predict mortality even after adjustment for subcutaneous fat and age [68]. Even more localized fat measurements such as pericardial fat and liver fat have been shown to be independent predictors of coronary artery calcification and insulin resistance, respectively [69]–[71]. At a higher level, android-to-gynoid fat ratio is an independent predictor of diabetes [72]. Trunk-to-leg volume ratio is a strong predictor of diabetes and mortality risk independent of other metrics of fat quantity and distribution [73]. The significance of these measures of fat distribution throughout the body are loosely captured by simple metrics such as waist circumference, waist-hip ratio, and “apple” vs. “pear” body shapes. Indeed, the diagnostic criterion of waist circumference in classifying the Metabolic Syndrome underscores the importance of body shape/tissue distribution over shape-agnostic measurements such as body mass index.

2.4: Technology Considerations

It is clear that detailed metrics and models of body composition and distribution and quality hold key insight into metabolic status and disease risk. Ideally, all of the aforementioned metrics would be available when evaluating a clinical patient or research subject. However, detailed composition analyses, such as four-component body composition analysis or quantification of liver

fat, may be expensive or impractical. Clinicians and researchers must constantly weigh the costs of particular measurements versus the information benefits to be gained, with particular sensitivity to specific patient needs and available resources. Equipment accessibility, patient burden, use of ionizing radiation, and measurement invasiveness must all be considered when selecting body composition assessments. Because of these concerns, in many cases only simple metrics like weight, body mass index, and waist circumference may be used in practice. Several different body composition measurement techniques, and the strengths, applications, and limitations of each, will be discussed in the following chapter.

3 | Body Composition Analysis Techniques

There are a variety of techniques used to measure body composition, from simple surrogate anthropometric measurements like BMI to high-resolution 3D whole-body computed tomography and magnetic resonance imaging. A summary of the primary tools used in body composition research is provided in Table 3-1. We detail each method in the following sections

Table 3-1: Summary of body composition techniques and measurements. Cost, patient burden, accessibility, and specific diagnostic needs must be considered when selecting an appropriate measurement technique.

Technique	Measurements	Measurement Level	Cost	Notes
Anthropometry	Body Mass Index, Waist Circumference, Waist Hip Ratio	Whole-Body, Regional	Very Low	
Underwater Weighing (UWW)	Total Body Volume, %Fat	Whole-Body	Moderate	
Air Displacement Plethysmography (ADP)	Total Body Volume, %Fat	Whole-Body	Moderate	
Deuterium Dilution (D ₂ O)	Total Body Water, %Fat	Whole-Body	High	
Bioelectrical impedance Analysis (BIA)	Total Body Water, %Fat	Whole-Body, Regional	Low	
Computed Tomography (CT)	Volume, Fat, Muscle, Bone	Whole-Body, Regional, Voxel	High	High Ionizing Radiation Dose
Magnetic Resonance Imaging (MRI)	Volume, Fat, Muscle	Whole-Body, Regional, Voxel	High	
Dual Energy X-ray Absorptiometry (DXA)	Volume, Fat, Lean, Bone	Whole-Body, Regional, Pixel	Moderate	Low Ionizing Radiation Dose
3D Optical Surface Imaging	Volume, Fat, Lean	Whole-Body, Regional	Low	

3.1: Classical Anthropometry

Anthropometry, meaning “human measure” in Greek, encompasses a variety of simple measurements of the human body including lengths, circumferences, and mass. Because anthropometric measurements typical only require simple tools such as rods, tapes, calipers, and scales, these methods are highly accessible and easily acquired even in resource-limited environments [74]. As described previously, body mass index – or the Quintlet index – is perhaps one of the most

broadly-used anthropometric measurements available. Requiring only scale weight and a height measurement, BMI is highly appealing for population studies especially in low- and middle-income countries where access to clinics and health assessment tools may be limited. Indeed, despite the fact that obesity is defined specifically by an excess accumulation of adipose tissue, the diagnostic metric for overweight and obesity is BMI (which does not discriminate between body tissue types) [1], [75]. Keys noted in a 1972 review of various anthropometric indices that BMI, while not without its flaws, is a suitable indicator of obesity at the population level [76]. Despite its limitations for individual assessment (e.g. athletes with high muscle mass may be classified overweight or obese despite very low body fat levels), BMI in many cases continues to be the frontline metric for physician assessment of metabolic status [77].

Waist circumference (WC) and waist-hip-ratio (WHR) are other simple anthropometrics that approximate central adiposity. There several other indices that have been developed such as waist height ratio (WHtR) [78] and a body shape index (ABSI) [79]. Several studies have shown that these metrics better predict adverse metabolic outcomes than BMI [80]–[83]. However these indices are still not direct measurements of body composition, and there can be significant variability in measurement depending on observer training and measurement site [84], [85]. While anthropometric measurements are highly useful and practical for health assessment, they remain surrogate measures of body composition.

3.2: Total Body Density

Behnke and Siri's two-component body composition models require accurate measurement of body density. Scale weight is simple to measure with high accuracy. There are two primary methods for measuring body volume, described below.

3.2.1 Underwater Weighing

Underwater weighing (UWW, also known as hydrostatic weighing) is based on Archimedes' principle that buoyant force exerted on an object is equal to the weight of fluid displaced by the object. The subject's weight is measured in the open air (W_{air}), then weighed underwater ($W_{underwater}$) [86]. Underwater weight is acquired by having the subject sit on a seat connected to a force meter (Figure 3-1). The seat is lowered into a large tank of water until the subject is completely submerged, and weight is recorded. Volume of the body V_B is then calculated as follows:

$$V_B = \frac{W_{air} - W_{underwater}}{D_{water}} - V_R$$

where D_{water} is the density of water and V_R is residual volume, which is dominated by lung volume. Subjects are typically encouraged to exhale completely before submersion. Residual volume can then be measured using gas dilution techniques or estimation equations based on subject sex, age, and height [86]. Body density is given by $D_B = W_B / V_B$, which can be used with reference densities of fat and fat free mass to calculate two-component body composition, as described by Siri [51] and Brožek [87]. The Siri equation is reproduced below.

$$\%Fat = \left(\frac{495}{D_B} \right) - 450$$



Figure 3-1: Example of an underwater weighing apparatus. The subject rests on a seat connected to a force meter. The seat is lowered into the water until the subject is completely submerged, and her underwater weight is then measured. Image source: <https://education.uky.edu/khp/laboratories/exercise-physiology-lab/>

3.2.2 Air Displacement Plethysmography

In 1995, Dempster and Atkins reported on the development of the BOD POD, a new device for body volume measurement that relies upon air displacement plethysmography (ADP) [88]. The technique had been proposed and researched for several decades, but this work marked the first implementation of ADP with sufficient accuracy and stability for commercial deployment [89].

A subject sits inside the enclosed chamber of the BOD POD (Figure 3-2) while wearing minimal, form-fitting clothing. The subject chamber is connected to a smaller chamber with a flexible diaphragm in between. The volumes of the two (empty) chambers are known precisely, and the diaphragm is actuated to induce small volume changes between the two chambers.

Using Boyle's Law ($P_1V_1 = P_2V_2$), the volume of the loaded subject chamber can be calculated. Subtracting this from the volume of the empty subject chamber yields the body volume of the subject. As with underwater weighing, the measured volume must be adjusted downward for residual lung volume – either from equation estimates or a direct measurement using a breathing tube that attaches to the system and employs the same ADP measurement principle.

The same composition equations used to estimate body %Fat from UWW body volume measurements (such as the Siri equation in the preceding section) are used for ADP body volume measurements [88]. Due to its ease of use compared to UWW, ADP is now the primary tool for body volume measurement [53]. Specially-designed devices with smaller volume chambers such as the PEA POD have been developed for children and infants, and several studies have been performed to validate the accuracy of the technique in such individuals [90].

3.3: Total Body Water

Accurate measurement of total body water (TBW) mass enabled four-component body composition measurement in the laboratory setting. This is particularly useful in individuals with variable hydration status (e.g. growing children and older adults) whose FFM composition may not be accurately predicted by reference adult norms. In normally-hydrated adults, TBW measurements alone can be used with reference fat free mass hydration (73.2%) [91] to estimate %Fat:

$$FFM = TBW/0.732$$

$$\%Fat = 100 * \left(1 - \frac{FFM}{TotMass}\right)$$



Figure 3-2: The BOD POD (COSMED, Rome, Italy) air displacement plethysmography device for measuring body volume. Image source: <https://bit.ly/2KKrTZr>

3.3.1 Deuterium Dilution

Dilution measurement techniques for calculating total body water require a dose of isotopic water that mixes freely in the body water pool. The dose is administered, and the subject is instructed to refrain from strenuous activity or food/drink consumption for a period of 2-5 hours while the dose equilibrates. Body water samples (usually saliva or urine) are collected and analyzed using spectrometric techniques such as Fourier Transform Infrared Spectrometry (FTIR) to

determine the dose concentration within the body water pool. The size of the body water pool is then the administered dose amount divided by the equilibrated dose concentration [92]:

$$TBW (kg) = \eta * \frac{Dose D_2O [mg]}{enrichment D in saliva \left[\frac{mg}{kg} \right]}$$

where η is a dilution space correction factor, described below.

Stable water isotopes of 2H_2O (deuterium, also D_2O) or $H_2^{18}O$ (O-18 water) are commonly used today for dilution protocols to measure total body water [53], [54]. These isotopes have largely supplanted the radioactive isotope 3H_2O (tritium) [93] for this purpose. It must be noted that each of the isotopic molecules occur naturally, and thus trace amounts may be present in the body at baseline. In addition, each of the aforementioned water isotopes undergo exchange with non-aqueous oxygen or hydrogen in the body [53]. Correction factors must be applied to account for these considerations. For deuterium dilution protocols, experimentally validated dilution space correction factor is $\eta = 1.041$ [92].

3.3.2 Bioelectrical Impedance Analysis

Characterization of the electrical properties of tissues dates back to the 1870s, but the foundations of modern bioelectrical impedance analysis (BIA) were developed a century later [94]. In brief, the body is modeled as one or more homogeneous conductive cylinders. A tetrapolar array of electrodes is attached at distant points on the body (e.g. the ankle and wrist, see Figure 3-3) – a small current is passed between one pair of electrodes, and the voltage differential is measured across the other pair. Measurements are recorded at one or more frequencies to estimate the resistance and

reactance (together, impedance) of the body. At zero (or very low) frequency, the electrical signal is insulated by cell membranes and conducted only by extracellular water (ECW) in the body. At infinite (or very high) frequency, the signal is conducted through both intracellular (ICW) and extracellular water. These combined represent total body water [95].



Figure 3-3: A clinical multifrequency segmental bioelectrical impedance analysis device with touch electrodes connected to the subject's fingers and ankles. InBody S10 (InBody Co. Ltd., Seoul, South Korea). Image source: <http://www.inbody.com/global/product/inbodys10.aspx>

BIA is an attractive tool for body composition analysis because it is relatively inexpensive, fast, and easy to use. The balance of ICW to ECW in the body can be used to estimate fat/lean composition using assumed hydration constants for those tissue types. Segmental BIA devices perform a series of measurements across different pairs of electrodes connected to each appendage to estimate regional body composition in the limbs and trunk. Many commercial products have been introduced at the consumer level that offer body fat estimates using BIA technology. It should be noted that BIA fat estimates are sensitive to fluctuations in hydration, and that the electrical

conductivity of the skin can introduce significant noise. Furthermore, the assumed cylinder model of the body may not hold for individuals with varying body shapes [96].

3.4: Dual Energy X-Ray Absorptiometry

DXA was first introduced in the 1980s as a tool for measuring areal BMD [97]. DXA represented a significant advance over single- and dual-photon absorptiometry techniques as it allowed for wide field of view imaging of bone density, even in regions of the body with significant soft tissue. Today, DXA is the primary technique for diagnosis of osteopenia and osteoporosis. Body composition analysis is a second significant use of DXA technology. Subjects lie flat on the scanner bed (Figure 3-4) during a whole-body scan that takes about five minutes. The principles of DXA will be discussed in section 4.1.1 .

The scan arm and table of the device move in a coordinated fashion to sweep the X-ray beams across the entire table. X-ray dose from a whole-body DXA scan is less than 5 microsieverts – an amount comparable to the dose received in one day due to natural background radiation. Scan data are processed on a connected computer. A certified technician analyzes the scan, and a report is generated that includes fat, bone, and lean masses for the total body as well as arm, leg, and trunk subregions [98].



Figure 3-4: A dual energy X-ray absorptiometry scanner. GE iDXA (GE Healthcare, Madison, WI). Image source: <https://bit.ly/2ws7DJ5>

DXA is appealing for body composition analysis because it provides regionalized 3-component body composition. DXA can also be used to estimate the relative amounts of subcutaneous and visceral fat in the abdomen using a projection method described by Kaul and colleagues [99]. The technology provides rich body composition information, but its use of ionizing radiation (albeit low dose) and high training requirements for technicians are limitations to broader use.

3.5: Computed Tomography and Magnetic Resonance Imaging

Quantitative Computed Tomography (QCT) is an X-ray based 3D imaging method that can be used to quantitatively image body composition in three dimensions [100]. By calibrating measured attenuation in Hounsfield Units (HU) to materials of known density, QCT provides quantitative density measurements. Notable body composition metrics include volumetric BMD, skeletal muscle volumes, organ volumes, visceral fat volume, and intermuscular adipose tissue (an indicator of muscle quality) [101]. QCT can provide richly-detailed full body 3D images of internal composition, but the high X-ray dose requirements limit its use to select research applications or

opportunistic screening [102]. In most cases, only specific cross-sections of interest within the body are imaged using CT in order to minimize dose.

Magnetic resonance imaging (MRI) is another 3D technique that can provide high-resolution internal composition images. MRI can provide many of the same internal volume measurements that CT provides, without any ionizing radiation. Development of chemical shift imaging techniques has enabled isolation and relative quantification of fat and water signals in MR images, and recent work on ultra-short- and zero-time echo (UTE/ZTE) MR imaging has made it possible to image bones [103]. MRI has several advantages for detailed body composition imaging, but it is prohibitively expensive for clinical analysis of body composition, and unsuitable for individuals with BMI exceeding about 40 kg/m² due to bore size and field of view limitations [104].

Both CT and MRI scanners feature a large circular bore that contains the imaging hardware. The subject lies flat on a table that is slowly moved through the bore during the imaging process. Imaging studies can be confined to small regions of interest, such as over a specific organ, or cover the whole-body (sometimes broken into several sequences).

A highly-specialized imaging procedure involving simultaneous positron emission tomography (PET) and CT imaging has been developed to image metabolically-active brown adipose tissue (BAT), or “brown fat” [105]. There are significant research efforts to understand the genesis and activation of brown fat, as this type of adipose tissue converts stored energy into heat and is associated with improved glucose sensitivity, bone density, and overall metabolic health [106], [107].

Because PET-CT imaging requires high X-ray dose in addition to a radioactive tracer, its use is even more limited to specialized research applications.

3.6: Three-dimensional whole-body surface Imaging

3.6.1 Background

Initial development of 3D surface scanning of the human body was largely driven by military and commercial interests [108], [109]. The technology offers a rapid, noninvasive method for acquiring several anthropometric measurements from a large number of individuals, thus providing a scalable solution for custom fitting. 3D surface scan anthropometry supports multiple simultaneous measurements with high precision and repeatability [110]. In addition, 3D scans can be analyzed post-acquisition if new body measurements are desired. All of these features make 3D surface scanning a compelling tool for clinical use.

3.6.2 Imaging Technologies

There are several different technologies and for 3D surface imaging. We describe the technologies suitable for whole-body scanning below.

Laser line scanners sweep laser lines across a subject. Charge couple device (CCD) or complementary metal oxide semiconductor (CMOS) sensors are used to record the subject. Using fixed geometry between the laser source and image sensor, the deformation pattern of the recorded laser line is used to determine surface position in space. Line position information is assembled from all images in the sweep sequence to produce a full 3D model.

Structured light scanners utilize controlled illumination patterns across the imaging field of view to extract depth information. These include a projector to cast controlled bands of light across the field of view. “Light coding” scanners, such as the Kinect (Microsoft Corporation, Redmond, WA, USA), include an infrared (IR) emitter that casts a dot pattern across the field of view. In all cases, deformation of the known illumination pattern can be used to calculate depth throughout the scene.

Stereophotogrammetry scanners reconstruct 3D images from multiple 2D photographs taken from different angles around the subject. Landmarks are co-registered between images, and the known positions of the image sensors are used to triangulate each pixel in space. This technology, which mimics the depth perception of the human visual system, has already been implemented in a few consumer devices such the Nintendo 3DS portable video game system.

Time of flight (ToF) scanners also utilize coupled scene illumination (visible light or IR) and image recording (using CCD or CMOS sensors) [111]. However, instead of measuring pattern deformations, these scanners measure the round-trip time (RTT) for reflected photons to reach the image sensor in order to calculate depth information. The hardware in ToF scanners must be accurate to the picosecond scale to achieve millimeter precision. Previously used primarily for architectural and surveying purposes, ToF technology (for near-field applications) has been made more broadly accessible with the introduction of the second-generation Microsoft Kinect.

Millimeter wave scanners utilize electromagnetic (EM) wave reflection patterns from the skin surface to construct a full 3D body image. Active scanners emit EM energy at the subject and measure reflected signals, while passive scanners only measure ambient/background EM radiation.

The advantage of millimeter wave technology is that the EM frequencies utilized freely penetrate most clothing materials. These scanners have seen broad adoption for security screening purposes at major airports.

The software used to derive measurements from 3D scans accepts raw data from the scanners in the form of a list of unconnected sampled surface points in 3D space (called a point cloud). These points are used to reconstruct a closed surface [112]. Smoothing and template interpolation techniques [113] may be applied to correct holes or irregularities in a scan. A set of defined landmarks are algorithmically placed on the closed surface, and surface measurements are calculated between these landmarks [114].

3.6.3 Applications and Opportunities

3D optical scanners provide a number of measurements that are useful in the clinical setting. These include various length, area, and volume measurements. Wells, et al. showed that 3D body surface scanning systems produced anthropometric measurements with precision within 0.5 cm [114]. The efficacy of these measures has been reported in various studies in both adult and youth populations [115]–[117]. 3D length and circumference measurements can be utilized to quickly calculate several established body shape indices, including waist-to-hip ratio (WHR), waist-to-height ratio (WHtR), a body shape index (ABSI), and body roundness index (BRI). These indices have been shown to be significant risk factors for all-cause mortality, cardiovascular disease, diabetes mellitus, hypertension, sleep apnea, and cancer [79], [118]–[121]. Wang, et al. [115] demonstrated that 3D surface scanning can measure whole-body volume with precision below 1%. Notably, 3D optical scanning offers the distinct advantage of regional volume assessment, which is not possible

with UWW or ADP. Regional body volume is of interest for the calculation of indices such as the trunk-to-leg volume ratio (TLVR), which has been shown to be an independent risk factor for diabetes and mortality, even for individuals within the “normal” BMI range [73].

Utilizing 3D scanners, national studies on population anthropometrics have been conducted in several countries including the UK, USA, China, Spain, Mexico, Thailand, France, Korea, and Taiwan [122], [123]. These studies have been used to identify longitudinal trends in population anthropometrics and differences between national and ethnic groups.

An emerging use of 3D optical surface scanners is joint detection and pose/posture assessment [124]. In particular, the broad release of the consumer-oriented Microsoft Kinect and its accompanying software development kit has provided an accessible tool for static and dynamic marker-free skeleton posture detection from 3D surface images [125], [126]. Reyes, et al. demonstrated that such a system can be used for static posture analysis, spine curvature analysis, and range of movement analysis, with sufficient accuracy for diagnosis of musculoskeletal disorders such as scoliosis, kyphosis and lordosis [127].

3D surface scanning offers an appealing method for body composition analysis. Lee, et al. derived models of total and regional fat and lean mass utilizing regional volume and circumference features derived from 3D optical scans [128]. The same group also demonstrated estimation of visceral fat area using similar measures [129].

3D body surface scanning is clearly appealing for its ease of use, lack of ionizing radiation, and commodity hardware. Validation of 3D body scan methods using commercial hardware would

provide direct translational applications suitable for clinical and personal use. While linear, areal, and volumetric measurements from 3D scanners have been used for a variety of applications described above, there is significant fine surface and texture detail not utilized by these metrics. More detailed 3D body shape features may provide improved clinical health information at no extra cost or risk.

3.7: Unmet Needs and Proposed Solutions

Human body composition research has advanced tremendously over the past 70 years. There are several conceptual models for body composition with varying levels of complexity, and many different techniques available for body composition research. Our understanding of the biochemical processes and disorders of the human metabolic system continues to grow. However, despite these advances, simple surrogate measurements of body composition such as BMI or waist circumference remain the de facto standards in many clinical settings and epidemiological studies around the world. While valuable as population metrics, these measurements have limited accuracy for individual tracking, and often require increasingly-cumbersome adjustments for different sexes, ethnicities, and regions. There is an unmet need for accessible tools for detailed individual body composition analysis in the clinic and in the field.

To address this need, we propose several solutions built upon 3D optical (3DO) body surface scanning and DXA technology:

1. Validation of commercially-available 3D body scanners for rapid clinical anthropometric assessment that obviates the need for laborious tape and caliper measurements.
2. Development of statistical shape models that capture detailed features of 3D body shape and provide simple descriptors for the complexities of body shape and composition.

3. Development of statistical appearance models of DXA composition images to identify features of fat and lean tissue distribution that are uniquely associated to disease risk.
4. Integration and validation of BIA and DXA imaging to provide rapid, accurate, and practical 4C body composition.
5. Integration of 3DO and DXA technology to provide high resolution three- and four-component composition across the whole body.

Collectively these solutions would enable richer and more detailed body composition assessments in the clinical setting that may allow doctors to better predict disease risk and develop personalized treatment recommendations. They can also enable individuals to use accessible consumer imaging devices to better understand and monitor their own health.

4 | Advanced Techniques in DXA Body Composition

4.1: High-resolution 3-component DXA image separation

4.1.1 DXA Physics

The core principle of DXA is that different materials have unique X-ray attenuation properties. Measured beam attenuation at two different X-ray energy levels due to photoelectric and Compton scattering effects provides two independent measurements of tissue thickness at each pixel [130]. Using calibrated mass attenuation coefficients, it is possible to determine the masses of two different materials at a given pixel (Figure 4-1).

DXA Principle Of Operation

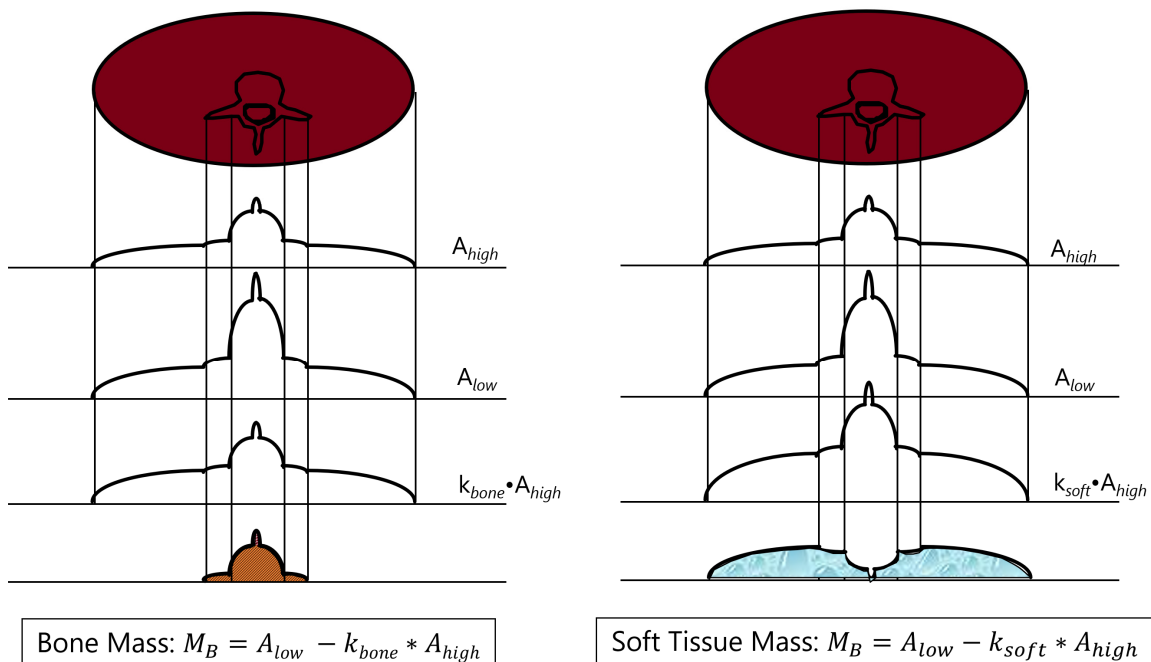


Figure 4-1: Principle of DXA. High and low energy X-ray attenuation profiles A_{high} and A_{low} are measured simultaneously. Different materials have different attenuation profiles by X-ray energy level. The ratio of specific mass attenuation coefficients (in cm^2/g) at low and high energies are used to determine k_{bone} and k_{soft} coefficients that allow for isolation of bone and soft tissue masses, respectively. Adapted from [131].

The innovation of DXA and DPA over single-photon absorptiometry allowed for subtraction of soft tissue thickness over a bony structure, thus enabling accurate measurement of bone density even in regions of the body with significant soft tissue. However, the composition of soft tissue can vary significantly across the body and across different people. To address this, the “R-factor”, or ratio of high to low energy attenuation $R = A_{low}/A_{high}$, can be used to determine the fat/lean composition of soft tissue in the absence of bone. A higher R value indicates higher lean content and a lower R value indicates higher fat content. The numerical relationship between R-factor and percent fat can be calibrated empirically, but for polychromatic X-ray systems such as DXA, that relationship varies with total thickness due to beam hardening, as shown in Figure 4-2. DXA soft tissue calibration thus requires nonlinear mapping to a phantom with multiple different fat/lean combinations at multiple different thicknesses [130].

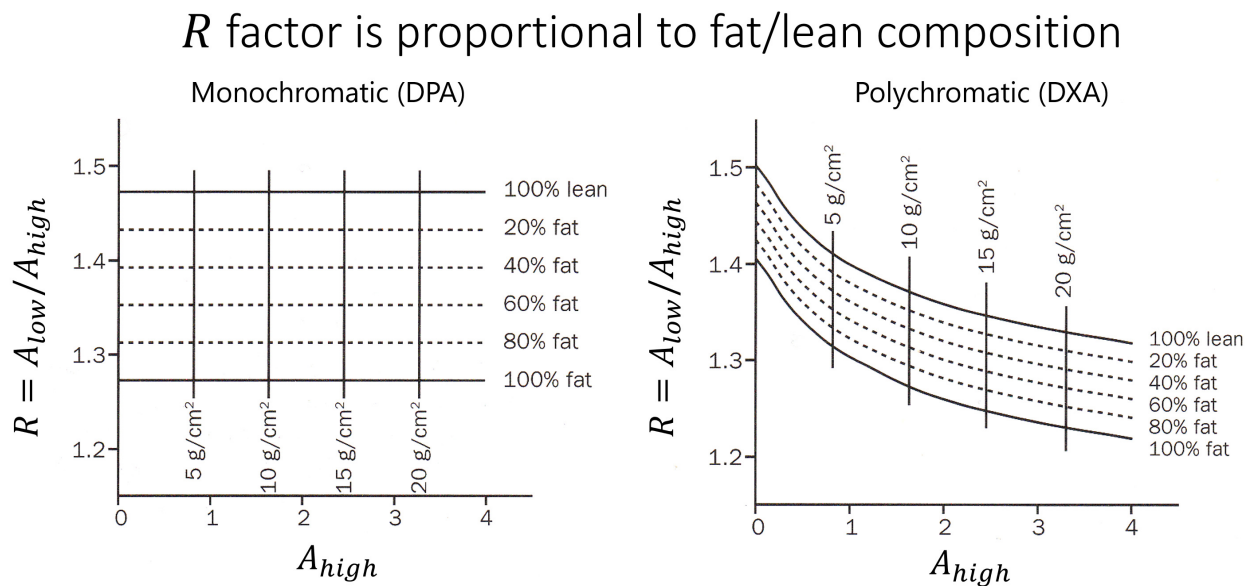


Figure 4-2: The “R-factor” ratio between low- and high-energy X-ray attenuation can be used to estimate fat/lean composition of soft tissue. For DXA, beam hardening effects with increased thickness produce a nonlinear relationship which requires multi-point calibration using soft tissue phantoms. Adapted from [130].

4.1.2 Three Component Spatial Assumptions

Although DXA reports contain fat, lean, and bone masses, DXA technology can be used to measure two different materials at a given pixel. As described above, bone mass and combined soft tissue mass can be calculated at a given pixel, but the composition of the soft tissue must be known. Fat/lean soft tissue composition can be estimated using the R-factor, but only in pixels that do not contain bone. Spatial assumptions about soft tissue composition must be made to produce 3C output from DXA. Specifically, the soft tissue composition over pixels with bone is assumed to be equal to the average soft tissue composition across neighboring pixels without bone. In practice, this approximation is performed at each line on a DXA scan, and thresholding is used to determine the presence of bone in a pixel [130].

While spatial approximation of soft tissue is likely robust in the appendages (where there is a large area of relatively homogeneous soft tissue only compared to a small area of bone), the abdominal region presents a particular challenge due to increased variability in fat distribution and limited lateral area free of bone. In whole-body scans, approximately 60% of body area may require spatial interpolation (Figure 4-3).

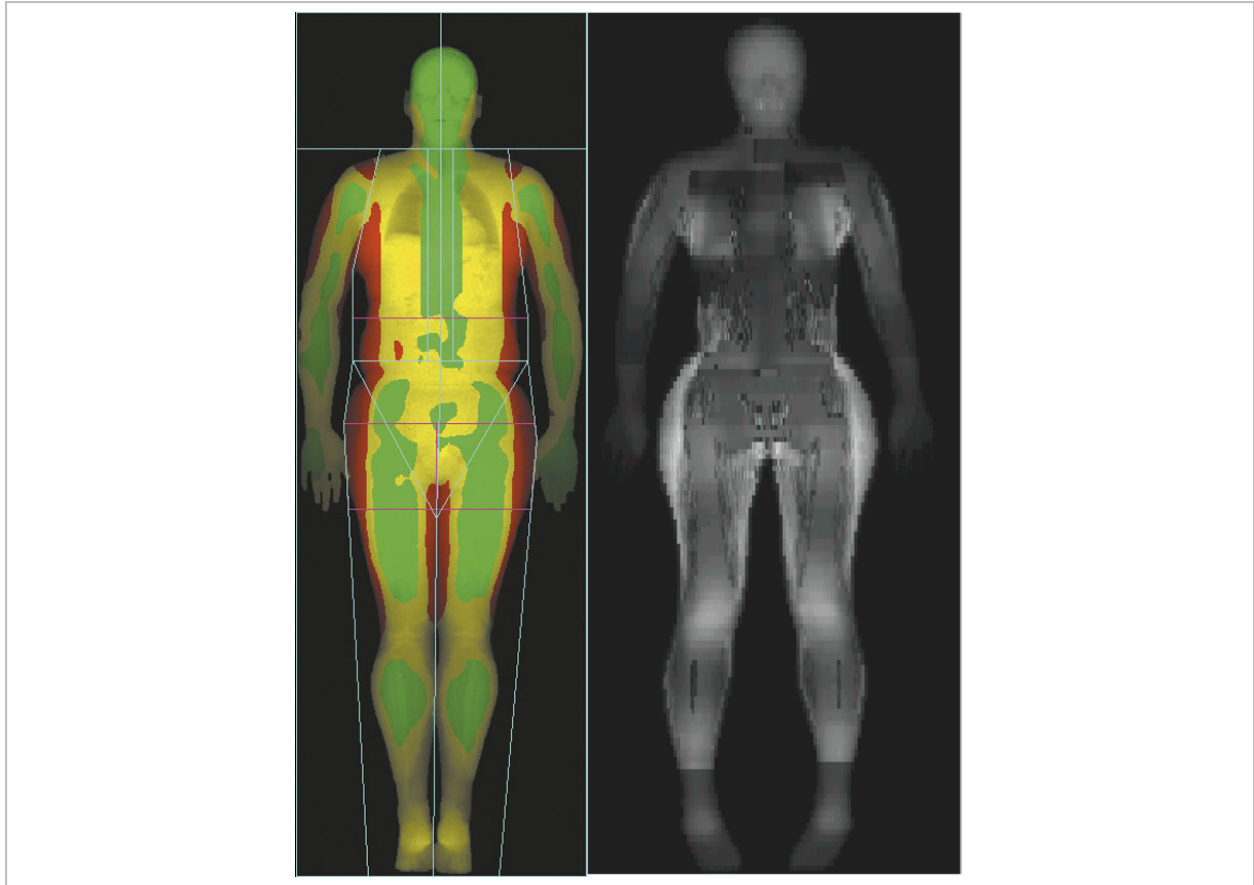


Figure 4-3: Example of soft tissue interpolation required in DXA scans. The image on the left from a GE scanner and the image on the right is from a Hologic scanner (courtesy of Joseph P. Wilson).

4.1.3 DXA Calibration and Image Processing

Accurate quantitative body composition measurements from DXA rely on careful calibration of the densitometer. Densitometers from Hologic, Inc. (Marlborough, MA) employ a continuous “internal reference system” calibration mechanism consisting of a wheel or drum of known thicknesses of different phantom materials approximating bone, soft tissue, and air that rotates in synchronization with the input power supply (60 Hz in the US). By measuring the differences in attenuations through each of the internal reference system, soft tissue mass attenuation coefficients can be determined in real-time. This allows the system to automatically adjust for beam hardening effects that occur with increased tissue thickness.

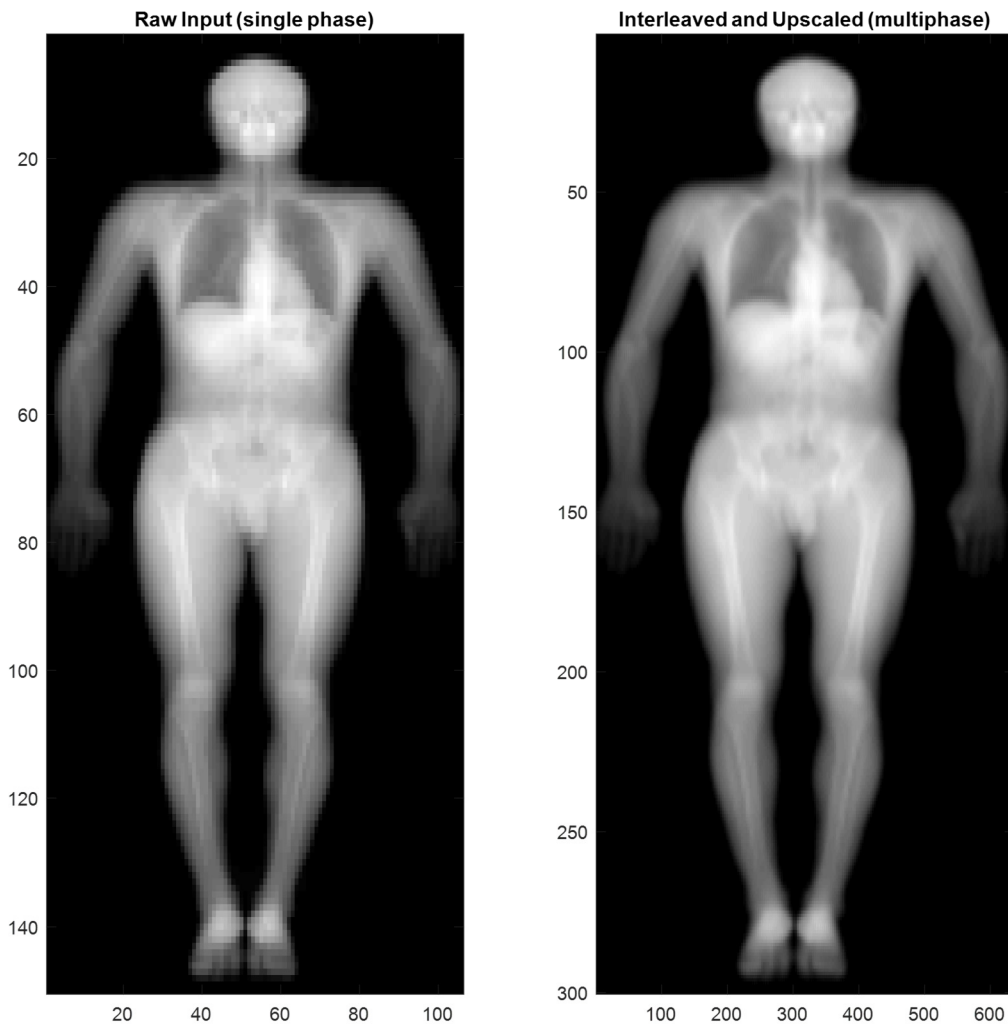


Figure 4-4: High-energy air-phase images extracted from a whole-body DXA scan. The image on the left is the raw data extracted from the scan file, and the image on the right is an interleaved, upscaled version that uses all three bone/soft tissue/air phase images from the Hologic internal reference system.

In addition to the bone/soft tissue/air phases of the internal reference system, the X-ray source oscillates between high and low energies such that there is a total of six transmission measurements in sequence [130]. These measurements are made in a continuous, sequential cycle throughout the duration of the scan, and each group of six measurements is collected into a single pixel. In actuality the sequential measurements are made at immediately adjacent to each other. We developed algorithms to linearly match and interleave the bone, soft tissue, and air phase images to provide increased resolution (Figure 4-4).

We used these high-resolution images from raw DXA scan files along with the bone and soft tissue calculation techniques described by Blake and Fogelman. Further improvements included areal sampling of adjacent soft tissue-only pixels for estimation of soft tissue composition (as opposed to line-by-line sampling) and use of a 2-dimensional second order polynomial surface for soft tissue composition estimation at each pixel. The soft tissue composition equation was calibrated to measurements of the official Hologic Tissue Bar (or TBAR) phantom – a six-step acrylic and aluminum phantom designed to approximate different fat/lean compositions at different thicknesses. The processing algorithms were developed in MATLAB R2016b (The MathWorks, Inc., Natick, MA) and are available in the ‘3c_dxa’ repository of the Shepherd Lab GitHub (see Appendix: Code Availability). They allow for generation of quantitative, high-resolution fat, lean, and bone images from any standard Hologic DXA scan (Figure 4-5). The algorithms support all major scan types, but the focus of this development was whole-body scans for body composition analysis.

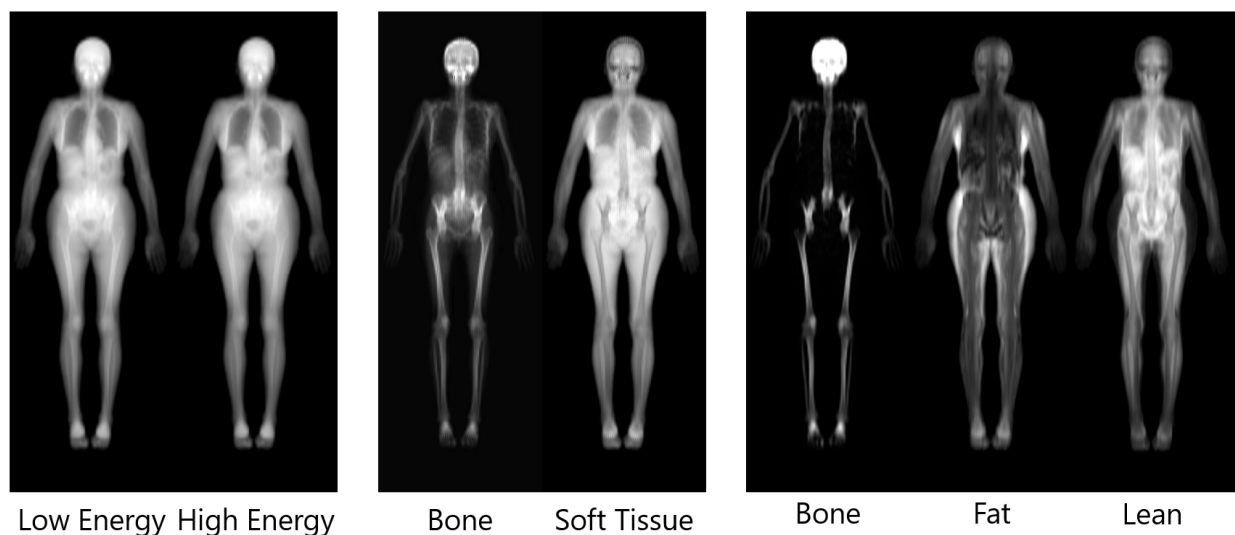


Figure 4-5: Quantitative 2C and 3C image extraction from whole-body DXA scan files. High- and low-energy X-ray attenuation maps are extracted from Hologic scan files (left group). Simple 2C subtraction assuming fixed soft tissue composition produces detailed bone and soft tissue mass images (middle group). 3C modeling

of variable soft tissue composition using the Hologic internal reference system enables calculation of bone, fat, and lean mass images.

As of this writing, the current stable version of the 3c_dxa code is tagged “mec2000_08.08.17”. This version of the code was used to process images from the Multiethnic Cohort (MEC) Obesity, Body Fat Distribution, and Cancer Risk study as will be described in section 4.3: . Total mass was calculated from the derived 3c bone/fat/lean images from this study of older adult men and women (n=1,851) and compared with corresponding mass values on the Hologic DXA report. Regression plots are shown in Figure 4-6. Coefficients of determination were $R^2 = 0.94$, 0.90 , and 0.64 for fat, lean, and bone mass, respectively. This present version of the 3c_dxa algorithm on the whole underreports fat and lean mass, but overreports bone mass relative to Hologic report values. Further refinement and calibration of the 3c_dxa code, potentially in conjunction additional understanding of the manufacturer’s software and whole-body scan processing algorithms, would improve agreement with tabulated Hologic report mass measurements.

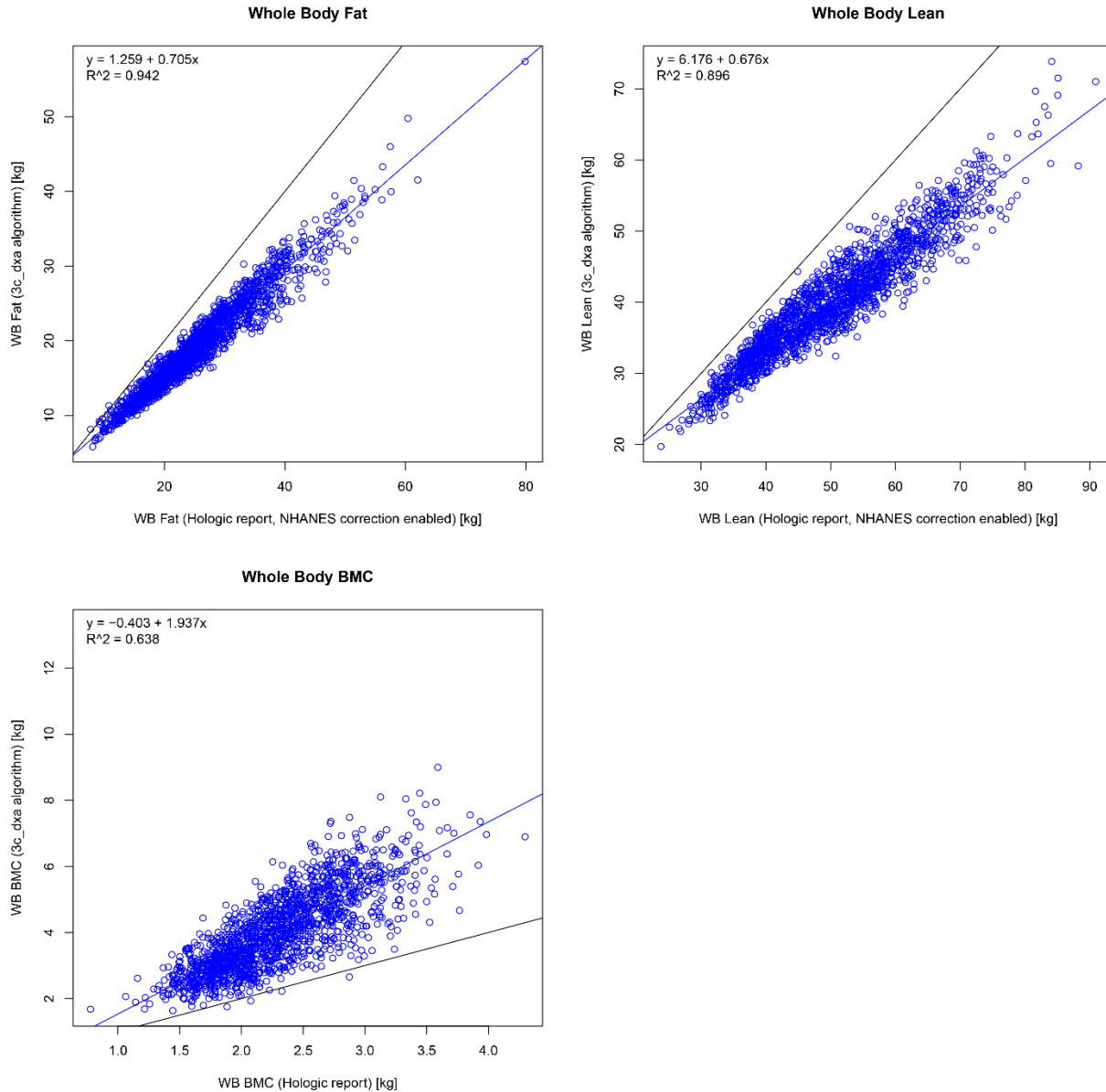


Figure 4-6: Regression plots for whole-body fat, lean, and bone mass as measured by the 3c_dxa algorithms (y-axes) compared with Hologic report values (x-axis). Hologic fat and lean values were calculated with the NHANES calibration enabled [132].

Images generated using this 3C pixel-by-pixel image processing approach, as well as the pixel-by-pixel total thickness estimation described by Wilson, allow for analysis and modeling of detailed spatial distribution of body tissues that is not captured in standard DXA reports. In the following sections, we describe the construction such detailed DXA “statistical appearance models”, and their metabolic significance in terms of disease and mortality risk.

4.2: Statistical Appearance Models of 3D Body Shape and Mortality Risk

4.2.1 Introduction

Global prevalence of diabetes has more than doubled over the past 30 years, affecting nearly 1 in 10 adults, and increasing numbers of children [133], [134]. The largest contributor is type 2 diabetes, linked to dyslipidemia, hypertension, and insulin resistance, collectively referred to as “metabolic syndrome.” Metabolic syndrome accounts for approximately 6-7% of all-cause mortality, 12-17% of cardiovascular disease, and 30-52% of diabetes [135]. Higher Body Mass Index (BMI), a measure of excess weight, was associated with mortality in early studies [136], [137] but is now controversial [138], [139] because more recent work has shown that higher BMI at older age is protective against mortality. However, measures of body shape and central adiposity have been shown to be associated with increased mortality risk. Waist circumference (WC) and its ratio to the hips are more closely related to adverse outcomes than BMI [80], [81], [118], [140]–[142]. The ratio of trunk-to-leg volume is a strong indicator of diabetes (fifth-to-first quintile odds ratio 6.8) and mortality risk (odds ratio 1.8), independent of BMI and WC [73], showing that more advanced descriptors of body shape accurately indicate metabolic risk beyond traditional measures. We hypothesize that statistical models of the shape and thickness of the whole body will better determine metabolic status and thus mortality risk than existing body shape measures.

Statistical appearance modeling (SAM) [143] has several successful applications including manufacturing [144], handwriting recognition [145], facial recognition [146], and medical imaging of the brain [147], heart [148], eye, liver, lung, kidney, prostate, knees [149], and proximal femur [62], [150]. To date, this powerful technique has not been applied to quantitative DXA body

composition scans. We have developed SAM algorithms to analyze pixel-based shape and composition from whole-body dual-energy X-ray absorptiometry (DXA) scans [151], [152]. Statistical appearance models from reanalyzed DXA images provide dominant modes of variance of body shape and thickness across a population. The statistical appearance models can be used to investigate associations of body shape and tissue density distribution and demographic (i.e. sex, race, etc.) and clinically-relevant disease outcomes (diabetes, sarcopenia, mortality) to identify those at high disease risk.

In this study, we present the methods to prepare DXA data for analysis, the challenges associated with image registration, and application of the resulting statistical appearance models to estimate mortality risk as a function of body shape.

4.2.2 Methods

Here we detail the DXA acquisition and image processing algorithms, as well as the statistical appearance modeling techniques. We then describe the statistical analysis of the models to identify and visualize SAM modes strongly associated with clinical variables such as sex and race, as well as mortality status in a sample of older adults.

DXA Scan Analysis

In commercial DXA systems, the X-ray attenuation values are used to directly solve for the mass of fat and lean soft tissue. We previously derived relationships from calibration phantom X-ray attenuations to quantify tissue volume and mass at each pixel in whole-body DXA scans [151].

Using custom software developed by the authors in MATLAB (MathWorks, Inc., Natick, MA), we

processed the raw low- and high-energy (HE) X-ray attenuation values from a Hologic QDR 4500A densitometer (Hologic, Inc., Bedford, MA) to produce three types of images for this study: (1) total thickness images, capturing the sum thicknesses all tissues in the body; (2) leanness images, defined as the ratio of fat-free (i.e. lean + bone) tissue thickness to total tissue thickness; and (3) R-value images, defined as the ratio of low-energy attenuation to high-energy attenuation. R-value decreases as thickness increases [130] and is used to calculate soft tissue composition (i.e. percent fat). Note that we define thickness here as tissue thickness projected onto the image plane (tissue thickness = tissue mass / tissue density * pixel area). Total thickness is thus generally the sum of the tissue thickness excluding air cavities. It is equivalent to linear path length an X-ray takes through the body.

Raw X-ray attenuation images from the DXA scanner had a resolution of 327 x 150 pixels, at 16-bit pixel depth. Each pixel had spatial dimensions of 2mm x 13mm. All images were upsampled by a factor of 6.5 in the y-direction to have a resulting resolution of 327 x 975 square (2mm x 2mm) pixels. Output thickness and R-value images were exported with 8-bit depth to be compatible with some of the annotation software.

Image Annotation

We defined 82 points on the skin edges as well as bony and soft tissue landmarks. A subset of available images were used to build an semi-automated annotation algorithm based on Constrained Local Model (CLM) methods [153], [154]. The annotator was blinded to participant data. This CLM was then run on each of the remaining R-file training images. Point placements by the algorithm were manually reviewed and corrected by the human annotator where necessary.

Differences in patient positioning led to variations in the extremities, which are of limited importance when examining body composition. Thus, we created a 52-point extended torso model, which includes the torso, the upper arms and upper legs, but not the forelimbs.

Statistical Appearance Modeling

Statistical shape and appearance models were constructed from the annotated images. Details of the approach can be found in [143]. In summary: (1) A shape model is built by (i) translating each set of annotation points so that they have a common center of gravity, (ii) applying Principal Component Analysis (PCA) to vectors containing the 2D annotation point coordinates that represent the aligned shapes for each image. (2) Shape variation is removed by warping each image to a reference frame defined by the mean body shape. Specifically, each image is deformed using a piece-wise affine transformation defined by a triangle mesh (see Figure 4-7 and Figure 4-8). (3) A “texture” model is built by applying PCA to vectors defined by the pixel-by-pixel grayscale intensity of these warped images. Texture models contain no 2D (in-plane) shape variation – only grayscale intensity differences due to varying X-ray attenuation measurements for each participant. (4) An “appearance” model is built by applying PCA to vectors formed by concatenating the shape and texture parameters. Appearance models thus capture both shape and texture information and reveal the ways in which shape and texture are correlated.

Concretely, a completed appearance model represents both (in-plane) shape and texture using the linked linear models

$$x = \bar{x} + Q_x c$$

$$g = \bar{g} + Q_g c$$

where x is a vector containing the annotation point coordinates, \bar{x} is the mean shape vector, g is a vector containing the grayscale pixel intensities in the mean shape reference frame, \bar{g} is the mean grayscale intensity vector, the columns of Q_x and Q_g are the ordered eigenvectors that span the variance in shape and texture across the images, and c is the vector of appearance model parameters. We refer to each eigenvector as a mode of shape and texture variation. These modes linearly map the compact parameter vector c to the shape and texture vectors x and g .

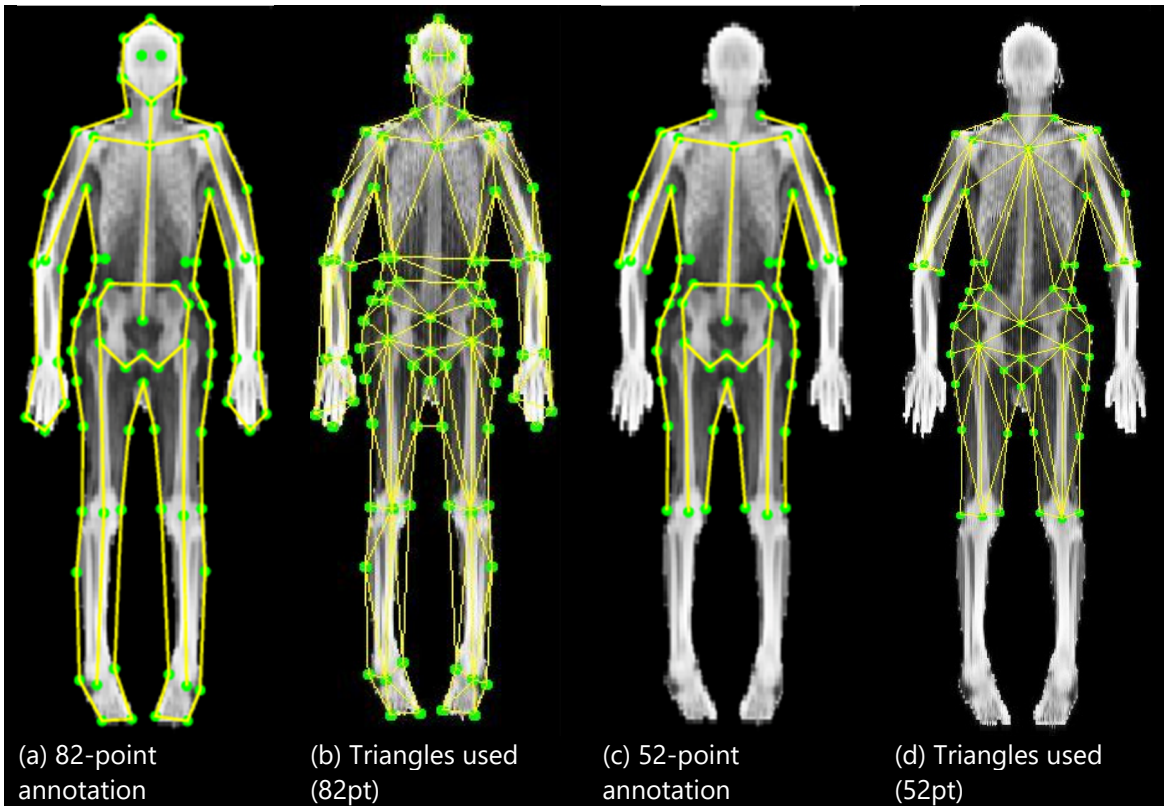


Figure 4-7: Annotation schemes and triangulations for texture warping. A full-body shape model containing 82 annotation points was initially developed. To eliminate spatial noise introduced by pose variation, a 52-point subset model was created that excludes the forelimbs and head.

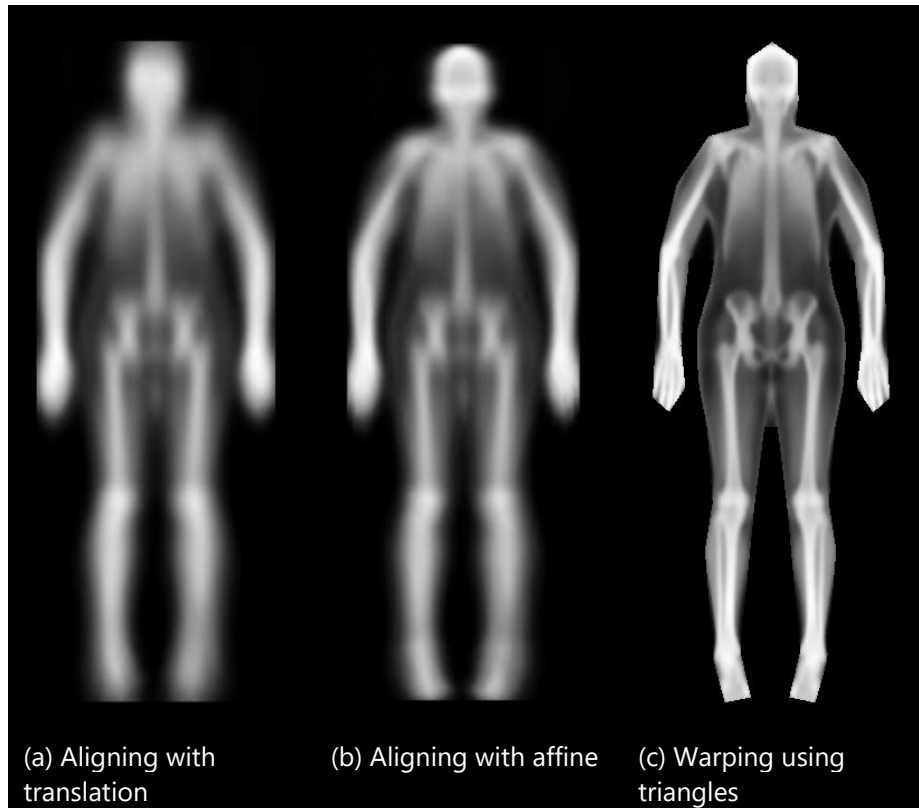


Figure 4-8: Mean images created with the 200 R-value images. Images were calculated using alignment with (a) translation, (b) translation, rotation, and scaling (affine), and (c) piecewise warping using the triangle model in Figure 4-7. Each successive mean image is visually sharper than the last, indicating that the more advanced alignment techniques are more effective at eliminating noise from shape and pose variation.

The appearance model allows new images with different shapes and textures to be generated by selecting new values for the parameters in c . Each image can then be compactly encoded by a vector of parameters, c , obtained by fitting a parameter vector c that synthesizes an image as close as possible to the original [143].

Proof of Concept Sample

A total sample of 400 older adults (ages 70-79) was selected from the longitudinal Health, Aging and Body Composition (Health ABC) study [29], [30], [155]. Two sets of 100 cases (participants who died during the first six years of follow-up) and 100 BMI-, sex-, and age-matched controls were selected. One set was used for model calibration and the other was used for validation.

Selection was stratified by sex and race (black and white). The Health ABC study was initiated in 1997 by the National Institute on Aging to examine the impact of changes in body composition and health conditions on age-related physiologic and functional status. At baseline, each participant received numerous clinical evaluations including whole-body DXA scans acquired using Hologic QDR 4500A systems (Hologic, Inc., Bedford, MA) and software version 9.03, located at two study sites. Validity of fan-beam DXA for measuring fat-free mass and leg muscle mass has been previously reported [156].

Statistical appearance models were trained on the calibration dataset and validated on the validation dataset. We investigated the bivariate association of the SAM parameter vectors to continuous variables of BMI and age using general linear regression models (proc GLM), and categorical variables of mortality status, sex, and race using logistic regression (proc LOGISTIC). Stepwise selection for the most significant SAM parameters, i.e. the number that explained 95% of the variance, were used to select parameters at a significance of $p \leq 0.05$ to estimate each outcome variable. All statistical analysis was done using SAS software, version 9.2 (SAS Institute, Inc., Cary, NC). This study and all included analyses were approved by Health ABC and the UCSF Committee on Human Research.

4.2.3 Results

Statistical Appearance Model Training

Figure 4-7 (a) shows the 82 points used to describe the outline of the body and some key landmarks on the skeleton. Figure 4-7 (b) shows the associated triangulation scheme used to warp the image to a reference frame. Figure 4-7 (c) shows the 52-point subset that excludes the points

associated with the lower arms and legs. Figure 4-7 (d) shows the associated triangles to the 52 points. Wherever possible, the triangles in the 52-point annotation are unchanged from the 82-point annotation. This demonstrates how our algorithm can select how the image is warped by manually defining the triangle relationships. Table 4-1 shows the relevant demographic and anthropometric markers for the sample participants included in this study. Figure 4-8 shows the mean image of the 200 calibration participants with progressively more sophisticated registration: (a) translating the images so that the centres of gravity coincide, (b) applying an affine transformation so that the bounding boxes coincide, and (c) using the full piece-wise affine transformation from triangulated mesh. The final registration has corrected for a range of body positions and shapes to bring all the pixels into approximate correspondence, allowing analysis of equivalent structures to be done easily. The images are displayed using the histogram equalised R-images. The models are built from 200 examples and their reflections (400 samples in total).

We found that 23 shape modes explained 95% of the shape variance defined by our markers. The first 6 shape modes are shown in Figure 4-9. Furthermore, after registering all images to the average shape, we found that 261 texture modes explained 95% of the variance in X-ray attenuation (represented as greyscale.) Six texture modes are shown in Figure 4-10. Figure 4-11 shows the combination of the shape and texture variances to form the full statistical appearance model. The first 237 SAM modes explained 95% of the combined shape and texture appearance. The model is capable of synthesizing both in-plane shape changes and intensity changes, and shows the main correlations between the two.

Table 4-1: Demographic characteristics of selected participants in HealthABC study.

Variable	White Men	Black Men	White Women	Black Women	P-value
Calibration set	N = 51	N = 49	N = 50	N = 50	
Age at baseline (yrs)	75.7 (3.0)	73.3 (2.7)	74.3 (3.0)	74.2 (3.1)	<0.01
Height (cm)	172.8 (5.8)	172.1 (5.8)	158.9 (5.2)	158.9 (6.6)	<0.01
Weight (kg)	80.7 (12.8)	77.5 (17.0)	66.0 (12.6)	71.6 (13.1)	<0.01
BMI (kg/m ²)	27.1 (4.3)	26.1 (5.3)	26.2 (5.0)	28.4 (4.9)	0.07
BMI Category (n)					
Underweight	1	5	4	0	
Normal	16	16	14	10	
Overweight	22	16	26	26	
Obese	12	12	6	14	
6-year status (n)					
Living	26	24	25	25	
Deceased	25	25	25	25	
Sagittal diameter (cm)	22.8 (3.2)	21.9 (3.7)	21.1 (2.8)	22.7 (2.8)	0.03
Abdominal circ. (cm)	101.1 (10.7)	96.4 (14.8)	96.4 (11.2)	97.7 (12.3)	0.18
Validation set	N = 50	N = 50	N = 50	N = 50	
Age at baseline (yrs)	74.7 (3.2)	72.4 (2.6)	74.0 (2.5)	74.1 (2.8)	<0.01
Height (cm)	172.2 (5.4)	172.7 (7.3)	159.8 (5.4)	159.8 (6.2)	<0.01
Weight (kg)	76.6 (9.8)	78.7 (14.7)	65.4 (13.5)	72.6 (11.9)	<0.01
BMI (kg/m ²)	25.8 (2.9)	26.3 (4.3)	25.7 (5.6)	28.5 (4.9)	0.08
BMI Category (n)					
Underweight	0	0	2	0	
Normal	24	20	22	14	
Overweight	20	22	16	20	
Obese	6	8	10	16	
6-year status (n)					
Living	25	25	25	25	
Deceased	25	25	25	25	
Sagittal diameter (cm)	21.8 (2.6)	22.2 (3.3)	20.6 (3.4)	22.4 (3.3)	0.02
Abdominal circ. (cm)	98.9 (9.2)	97.1 (12.5)	97.2 (14.7)	97.1 (11.9)	0.86

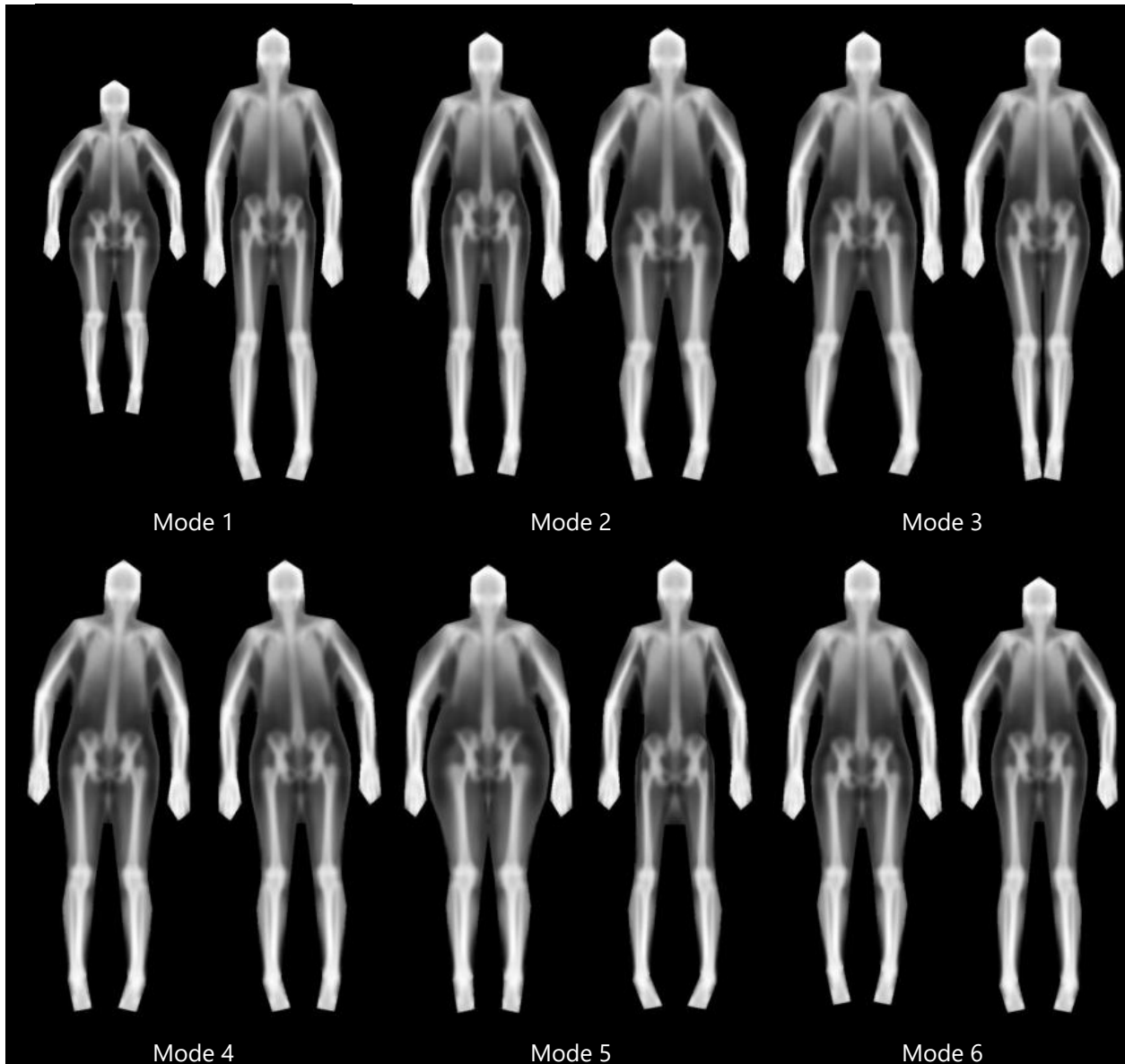


Figure 4-9: Shape only modes (first 6). For each mode, the ± 3 standard deviation (left and right respectively) images are shown. 23 modes were required to explain 95% of shape variance. At a high level, we see that body height is captured in Mode 1, width in Mode 5, and android/gynoid shape variation in Mode 2. Note that several modes capture variation in subject pose.

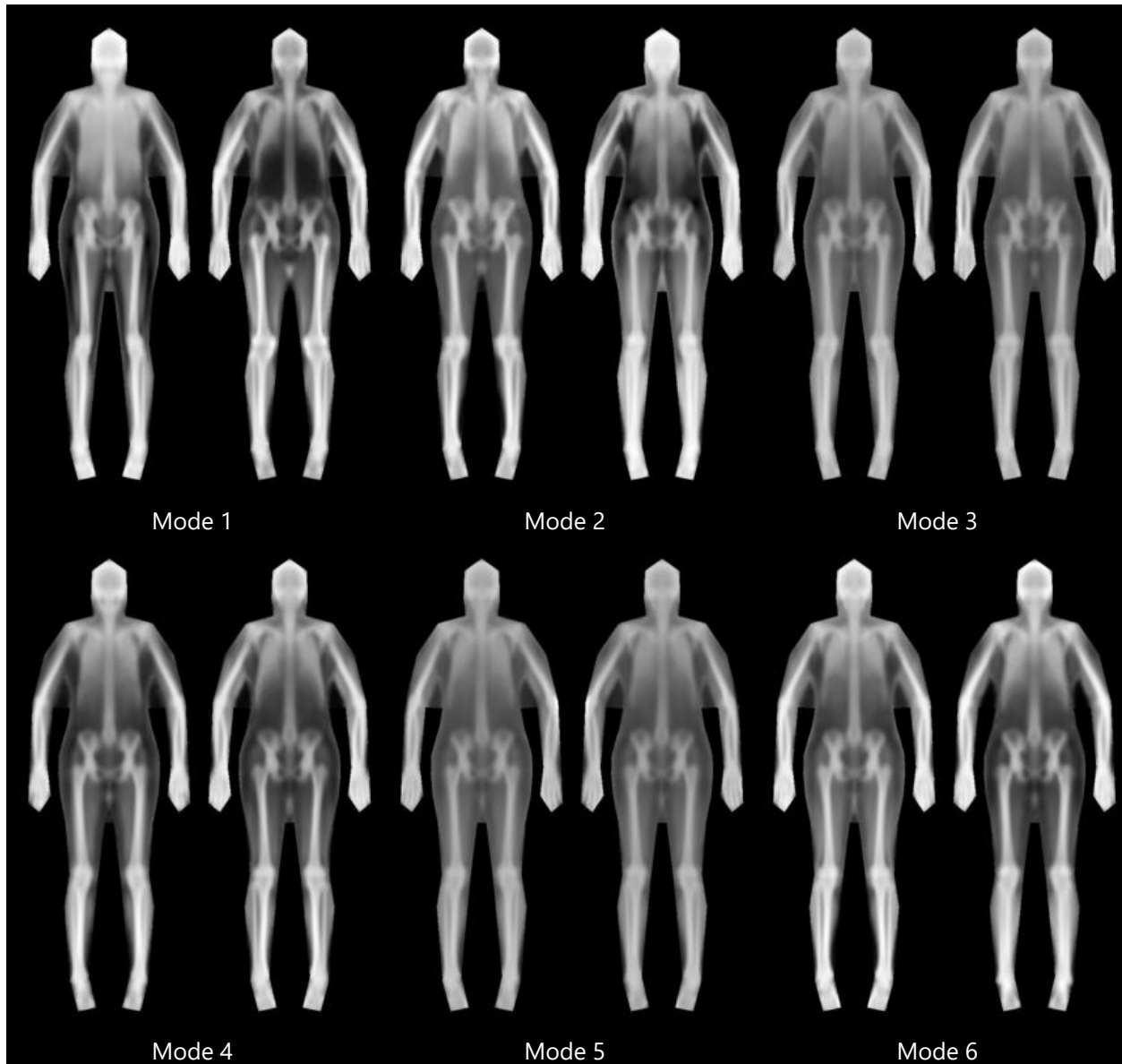


Figure 4-10: Texture only modes (first 6). For each mode, the ± 3 standard deviation (left and right respectively) images are shown. 261 modes explained 99% of the variance. Since this model captures only texture information, all images have the same shape, but differing grayscale intensity indicating different distributions of tissues throughout the regions of the body.

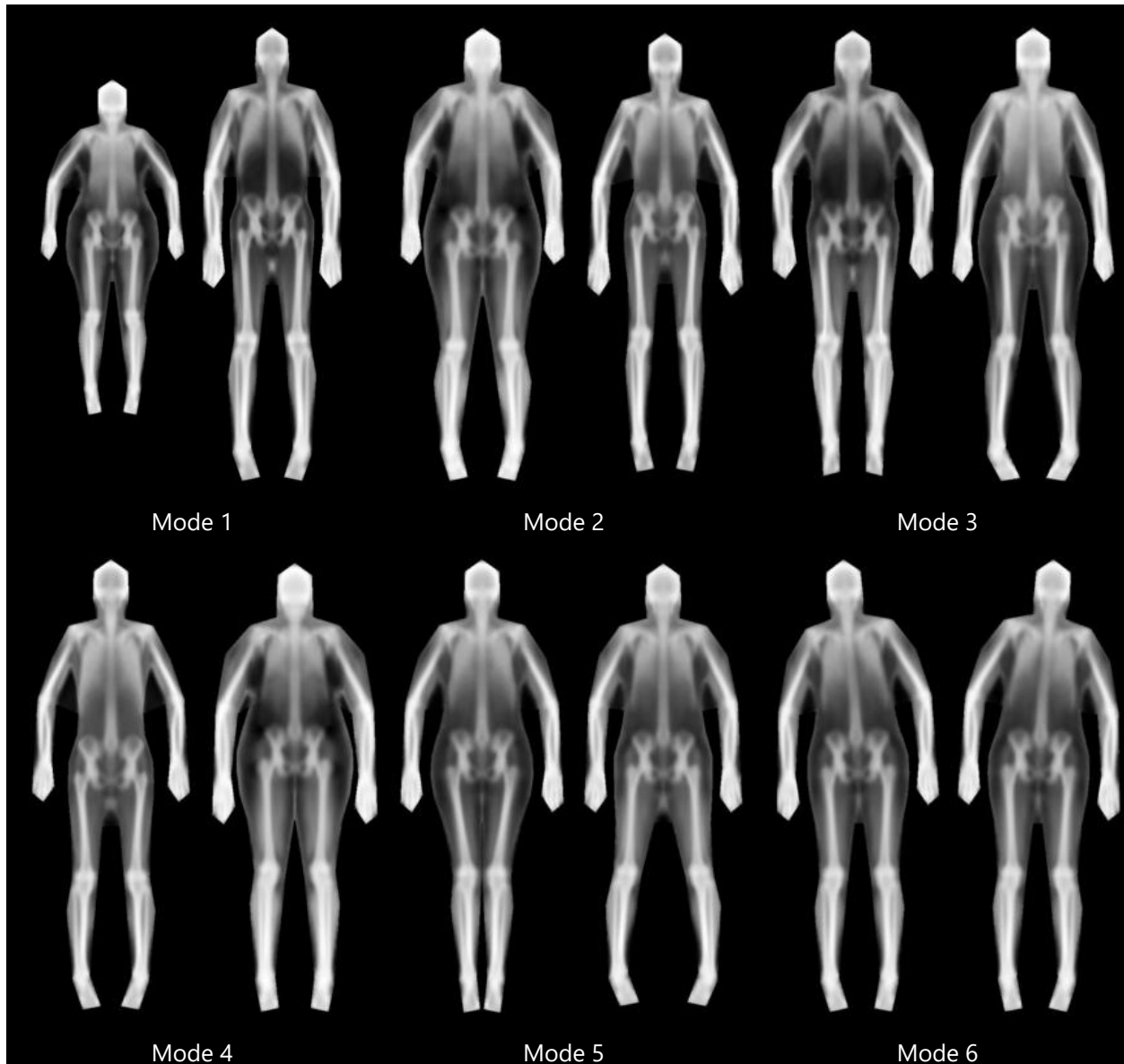


Figure 4-11: Combined appearance modes (first 6). For each mode, the ± 3 standard deviation (left and right respectively) images are shown. 237 modes explained 99% of the variance. This model captures dominant modes of variation in both texture and shape.

Alternative Representations of the Statistical Appearance Model

Several examples are given of how different appearance models can be created from different texture information found in the DXA images. Figure 4-11 shows the first 6 modes of the R-value images where white represents higher density. Figure 4-12 shows the first 8 modes of an appearance model of shape and body thickness, using a 52-point annotation excluding the forelimbs. Figure

4-13 shows a combined appearance model of shape, thickness, and leanness, where thickness is encoded as green and leanness is encoded as red in an RGB image. Linear scaling was applied to ensure the data range was in 0 to 255 range. The blue channel was not used.

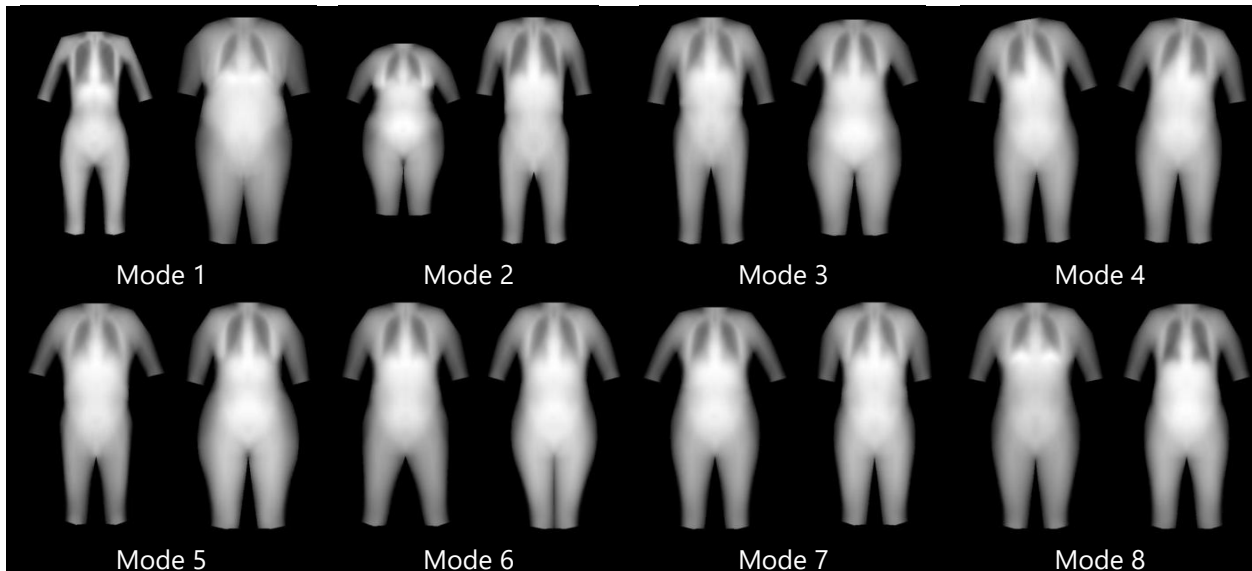


Figure 4-12: The first 8 appearance modes for a SAM of solid body thickness (lean + fat thickness) and 52-point annotation. (± 3 SD). We see significant differences in body shape roughly corresponding to weight, height, and sex in Modes 1, 2, and 3, respectively. Again, pose variation is captured in multiple modes.

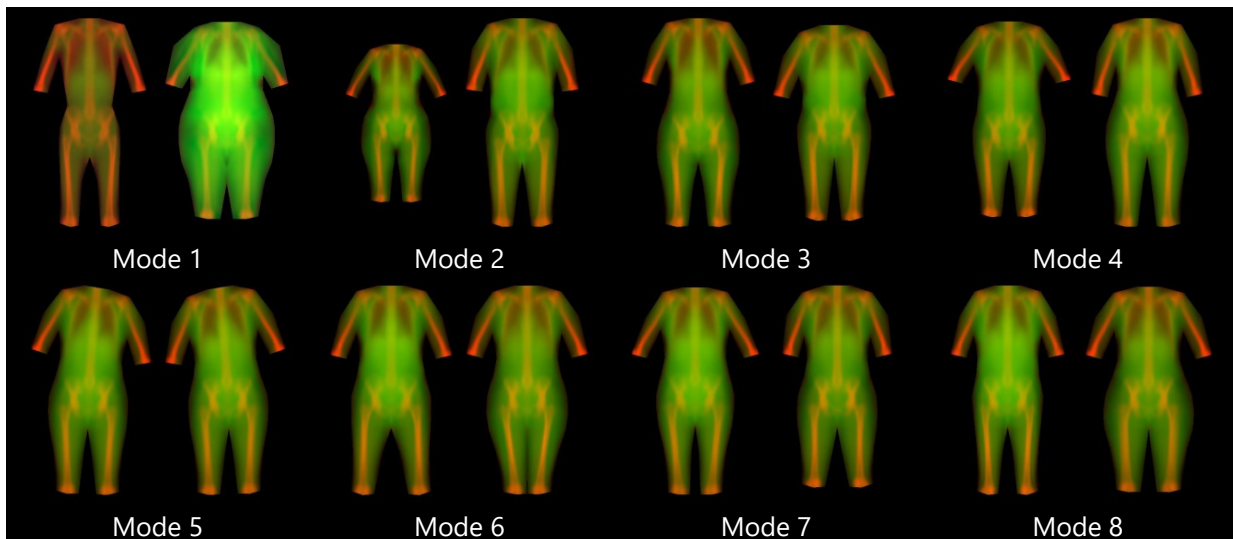


Figure 4-13: Hybrid model of shape, thickness, and leanness including bone. Total thickness is represented by green intensity and %lean by red intensity. (± 3 SD). Mode 1 captures dramatic body shape and composition variance ranging from a high-lean, low-thickness (thin) phenotype to a low-lean, high-thickness phenotype.

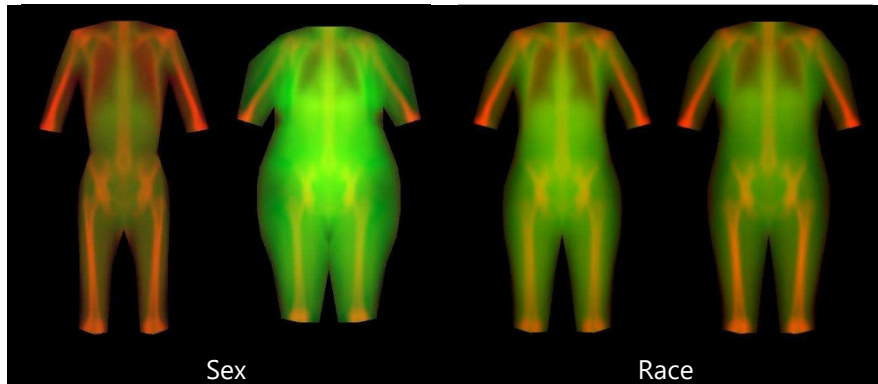


Figure 4-14: Linear regression models of sex and ethnicity using the combined appearance model of Leanness + Thickness images (± 3 S.D.s). There were 3 appearance modes used in the sex model that achieved an AUROC of 0.99. There were 6 appearance modes used in the Race model that achieved an AUROC of 0.91. These models show that statistical appearance of body shape, thickness, and leanness accurately identifies sex and race differences in the sample population.

Descriptive Models

Bivariate correlation coefficients between demographic and anthropometric variables and shape modes are found in Table 5-2. Of these variables, we found that only height predicted sex (AUC = 0.95). Body thickness and leanness, however, was more strongly predictive of sex - the final logistic model includes three shape modes (Table 5-3) and achieved AUC = 0.99. No combination of the following anthropometric or demographic variables (of sex, BMI, height, weight, sagittal diameter, nor abdominal circumference) predicted race even though this may not be universally true in all datasets. However, body thickness and leanness was a strong predictor of race – the final logistic model includes six shape modes (Table 5-3) and achieved AUC = 0.91. Visualizations of sex and race models are shown in Figure 4-14. Using a statistical appearance model of body thickness on the calibration dataset, we found that a logistic model with three SAM parameters predicted mortality with AUC = 0.66. Example images of low- and high-risk body appearances are shown in Figure 4-15. Note that the primary differences between the low and high risk were the apparent lung

volume and waist shape. The mortality model had an AUC = 0.62 when applied to the validation dataset. Regression equations for sex, race, and mortality are provided in Table 5-3.

Table 4-2: Correlation coefficients for each principal component of the shape model versus demographic and anthropometric variables

	PC1	PC2	PC3	PC4	PC5	PC6	PC9	PC10
Age								
Sex	-0.19	0.69	-0.39		0.35			
Race		0.23	0.37			0.22	-0.21	-0.26
BMI	0.93	0.27						
Height	0.22	-0.89	0.29					
Weight	0.95	-0.24					0.18	
Sagittal diameter	0.89	0.16		-0.16				-0.16
Abdominal circ.	0.86			-0.24				

These components correspond to the images in Figure 4-9. Only correlations with $P \leq 0.05$ are shown. Bold denotes $P \leq 0.01$ and shading denotes $P \leq 0.001$.

Table 4-3: Logistic regression equations for sex, race, and mortality

Model Type	Outcome	Equation	α	Train AUC
Thickness + leanness*	Sex	$P(\text{male}) = (1 + e^{-\alpha})^{-1}$	$-0.178 - 0.0026pc1 + 0.0041pc2 + 0.0027pc3$	0.99
	Race	$P(\text{white}) = (1 + e^{-\alpha})^{-1}$	$0.130 - 0.0019pc3 - 0.0008pc4 - 0.0019pc6 - 0.0009pc7 - 0.0013pc8 + 0.0042pc16$	0.91
Thickness**	Mortality	$P(\text{deceased}) = (1 + e^{-\alpha})^{-1}$	$0.0336 - 0.0015pc10 + 0.0014pc11 - 0.0026pc23$	0.66

Parameters for each model were selected using stepwise regression with a required P-value of 0.05 to stay in the model. *Visual representations of the first 8 thickness + leanness appearance modes are shown in Figure 4-14. ** Figure 4-13 shows the first 8 thickness appearance modes.

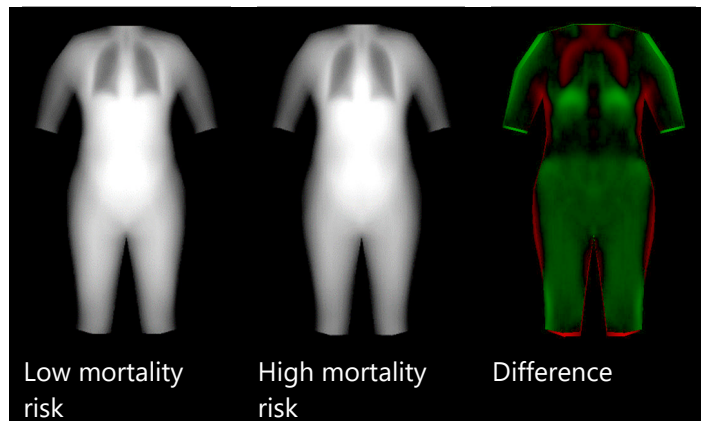


Figure 4-15: Linear regression model of mortality status using the combined appearance model of Thickness images (± 3 S.D.s). There were three appearance modes used in the model that achieved training AUC of 0.66 and validation AUC of 0.62. In the difference image, green indicates greater thickness in the low-risk image and red indicates greater thickness in the high-risk image.

4.2.4 Discussion

We have developed methods to describe and analyze the rich regional body shape and composition information captured in whole-body DXA images. We applied statistical appearance modeling techniques to body thickness and leanness images derived from raw DXA attenuation data. The resulting SAM principal components describing holistic body shape were shown to be highly predictive of race and sex, indicating that this technique is capable of distinguishing the unique shape characteristics of each group. Importantly, appearance modes of body thickness were predictive of mortality status. Inspection of the body shape differences captured by the appearance model (Figure 4-15) reveals interesting features such as apparent lung volume that differ by mortality status. These results suggest that this technique could be used to elucidate body shape and composition phenotypes that may be strongly associated with health status, provide new metrics for risk assessment in individuals, and reveal body features worthy of further research.

Previous work in this area was performed by Wilson in his PhD dissertation [157]. Wilson created whole-body principal component models that used only rigid affine-aligned thickness

images. This work did not include piecewise registration, or other image types. The preliminary models had a blurry appearance, similar to Figure 4-8(b), due to the lack of precise registration. Nonetheless, Wilson was still able to show strong correlations to patient demographic variables. Later, Wilson showed that body shape was related to mortality using trunk to leg volume ratios from DXA images [73]. In his fully adjusted models for mortality, he demonstrated strong AUC values of 0.83. Besides the representation of body shape, the Wilson study design differed from our design in population (Wilson: NHANES 1999-2004, ages 20 to 85 years; Health ABC: 75 years at baseline) and adjustments (Wilson: Age, gender, race, BMI, waist circumference, activity level, poverty index; Health ABC: none). Further future evaluations are planned in the NHANES population Wilson used to directly compare the SAM methods directly to simple measures like trunk to leg volume ratio.

Shape and appearance modeling has been applied to proximal femur DXA scans with success [150], [158], [159]. Goodyear et al. [159] showed that the combination of shape and appearance models with bone density produced the best AUC = 0.65 compared to any single measure for predicting hip fracture risk. To our knowledge, this is the first application of SAM techniques to whole-body DXA images. The models for sex, race, and mortality risk derived herein demonstrate the potential of this approach to provide novel and significant image features from standard DXA data.

This study had notable strengths. First, there was a similar number of men and women, and black and white participants. This is important because the models derived are equally weighted by sex and ethnicity. Second, because of our case and control design, we were able to increase the signal

present in the model for mortality over what would be expected in a prospective study of the same number of participants. However, this study had some limitations. First, the DXA data was acquired on one make of DXA system (Hologic). Our statistical appearance models would not be applicable to other makes without further validation. Additionally, the study population was limited to a narrow age range. A more complete analysis of body shape and appearance in a broader, representative sample of adults is warranted to ensure generalizability. Another issue was the limited data available for training the constrained local model for automatic annotation of the DXA images. All images required some degree of manual annotation point adjustment where the automated placement algorithm did not accurately detect body landmarks. Given sufficient high-quality training data, though, the automated CLM technique has been shown to achieve very good accuracy [153]. We expect that a large training dataset of DXA images across a wide range of body shapes and compositions would yield a precise and accurate active appearance model for fully-automated annotation.

Detailed models of the body shape and tissue distribution offer significantly more information than standard DXA analyses. This study demonstrates a method for describing holistic body shape, thickness, and leanness that reveals unique features by sex, race, and also predicts mortality risk. Further study is warranted to investigate body shape associations to other outcome variables of interest, across different populations. As this technique utilizes standard whole-body DXA image data, it is readily applicable to several existing study databases of DXA scans. In addition, supervised methods of feature selection beyond principal component analysis may yield more sensitive and specific predictors for clinical outcomes.

4.3: Body Composition Appearance and Metabolic Disease across Ethnicities

4.3.1 Introduction

Simple anthropometric measurements of body size such as body mass index (BMI) and waist circumference have long been shown to be significant indicators of metabolic risk for cardiovascular disease and diabetes [81], [82]. Trunk-leg-volume-ratio, a metric that assesses the general shape of the body, is a strong predictor of diabetes and mortality risk independent of BMI [73]. Body composition measurements, including holistic percent fat/lean and the quantification of visceral versus subcutaneous fat are even stronger predictors of metabolic risk [68], [160], [161]. It is evident that body size, shape, and regional composition offer significant insight into metabolic status and health risk. Whole-body Dual energy X-ray absorptiometry (DXA) imaging is a proven clinical method for total and regional body composition assessment [156], [162]–[164]. DXA provides a detailed 2D image of fat, lean, and bone mass throughout the body, however measurements are only reported for coarse regions (arms, legs, trunk). We developed statistical appearance models (SAMs) to capture 95% of the imaged variance in fat and lean tissue distribution. We hypothesized that detailed SAM descriptors of the distribution of adipose and lean tissues throughout the body would strongly predict metabolic status, across a range of different ethnicities.

4.3.2 Methods

Data from a sample of 2,000 older adult men and women across five different ethnicities were used in this analysis. We directly processed and analyzed whole-body DXA image data to construct SAMs of fat, lean, and bone tissue. Logistic regression equations were derived to predict

metabolic syndrome (MetS) status and diabetes status. We describe the details of each component of the study below.

Participants

The present analysis was performed as part of the cross-sectional Multiethnic Cohort (MEC) Obesity, Body Fat Distribution, and Cancer Risk study (NIH NCI 1P01CA168530). This study involved re-contacting 2,000 participants from the parent population-based Multiethnic Cohort study of 215,000 men and women across five different ethnicities (African American, Japanese, Latino, Native Hawaiian, and Caucasian). Re-contacted participants in the MEC Obesity study were selected to have an age between 60-72 years. Enrollment was stratified by sex, ethnicity, and six BMI categories (18.5-21.9, 22-24.9, 25-26.9, 27-29.9, 30-34.9, and 35-40 kg/m²).

Enrolled participants underwent whole-body DXA and abdominal magnetic resonance imaging, blood and stool specimen collection, as well as health and lifestyle questionnaires. Recruitment was performed at the University of Hawaii Cancer Center (UHCC, Honolulu, HI) and the University of Southern California (USC, Los Angeles, CA). Participants were scanned between May 2013 and April 2016. All participants provided informed consent, and the study protocol was approved by Institutional Review Boards at USC (#HS-12-00623), UHCC (CHS#17200), and UCSF (IRB#12-10255).

Dual Energy X-Ray Absorptiometry

Whole-body DXA scans were acquired on a Hologic Discovery/A system (Hologic Inc., Marlborough, MA, USA). All scans from both study sites were analyzed at the University of

California, San Francisco (UCSF) by a single International Society for Clinical Densitometry (ISCD) certified technologist using Hologic APEX software (version 3.3). Participants were clothed in examination gowns, without shoes, and positioned on the scanner table with arms out to the side, hands flat on table and feet in planarflex position, in accordance with the manufacturer's standard protocols. Participants with a high BMI (men $>32\text{kg}/\text{m}^2$, women $>31\text{kg}/\text{m}^2$) were systematically measured with a hemi-scan, where the participant is offset on the table such that the torso and right arm are within the scan region, and the left arm is extended off the table. For hemi scans, analysis is performed assuming symmetry of the arms.

DXA scanners were cross-calibrated using *in vivo* data of 12 individuals who underwent scans at both sites within 3 days. Each scanner was kept in regular calibration using phantom scanning protocols and according to ISCD guidelines.

DXA Image Processing

Using custom algorithms developed in consultation with the device manufacturer, we process each scan file produced by the Hologic system into separate images of bone mass, fat mass, and lean mass. These algorithms follow the method described by Blake, Wahner, and Fogelman [130]. Utilizing calibration information from known phantom scans, we quantified the mass of each tissue type at each pixel in a 654×300 whole-body image. Images were linearly scaled to a resolution of 654×1914 to have square pixels of length 1.02 cm on each side. DXA scan files have a native 16-bit depth. Processed tissue images were saved in maximum-quality JPEG format with 8-bit depth. To maximize dynamic range in the processed tissue images, we calculated the 98th percentile of tissue

mass observed at any pixel across all images. Those values were mapped to the maximum 8-bit intensity (255) for each tissue type (fat, lean, and bone).

Statistical Appearance Modeling

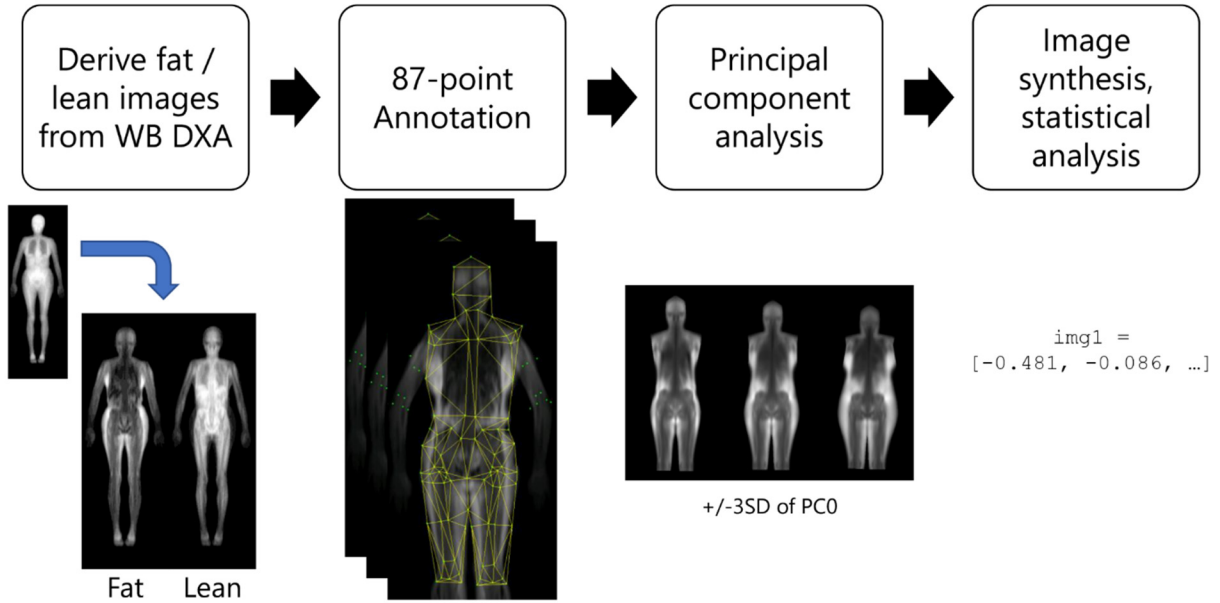


Figure 4-16: Schematic representation of the Statistical Appearance Modeling approach utilized in the present study.

Statistical shape and appearance models for the processed DXA images were constructed for each sex using the method described by Cootes [143] and am_tools version 3 software (University of Manchester, UK). A visual representation of the SAM method is shown in Figure 4-16. In brief, an 87-point shape model outlining the head, trunk, upper legs, spine, pelvis, and femurs was annotated on each image. The specific list of point definitions can be found in the shepherd-lab/dxa_sam repository (see Appendix: Code Availability). Note that this point set differs from the prior set defined in the pilot study (see section 4.2.2). Annotation was performed in a semi-automated manner using a random forest regression voting model [153] in conjunction with human review. A vector of the two-dimensional coordinates of the 87 annotation points define the “shape” of each

image. Triangles defined between these points are used to perform piecewise affine transformations to warp each image to the calculated average (mean) shape. A vector of grayscale pixel values in the warped reference frame define the “texture” of each image. “Appearance” is defined as the concatenation of shape and texture vectors. Each participant DXA image is thus processed into three different vector representations (shape, texture, appearance) for each of three different tissue types (fat, lean, and bone).

Principal component analysis was performed to reduce the high dimensionality of the shape, texture, and appearance data to a compact orthogonal space that captures 95% of the original image variance. The resulting principal components linearly define the modes of greatest variance in body shape and tissue distribution. Each image can be represented in this principal component space as a vector of principal component coefficients. These components compactly describe rich variation in body shape.

Statistical Analysis

Analyses were performed using SAS version 9.4 (SAS Institute, Cary, NC), R version 3.4.2 (The R Foundation), and MATLAB R2016a (The MathWorks Inc., Natick, MA). Mean principal component coefficient vectors were calculated for each sex and ethnicity subgroup. These mean vectors were used to synthesize the average fat and lean shape, texture, and appearance for each subgroup.

Metabolic syndrome was classified using the National Cholesterol Education Program (NCEP) Adult Treatment Panel III as described in section 1.2: [165]. Diabetes was classified as

fasting plasma glucose at or above of 126 mg/dL or A1C at or above 6.5 percent, in accordance with American Diabetes Association guidelines [166], or if the participant is currently taking antidiabetic medication. Separate models were derived for men and women.

Predictive equations were derived for metabolic syndrome and diabetes status using logistic regression with LASSO selection (`cv.glmnet` in R package `glmnet` version 2.0-13). Candidate variables for model selection were the principal components that explained up to 95% of variance in shape, texture, or appearance for whole-body fat and lean tissue. Models were trained on a random subset of 80% of the available data and validated on the remaining 20%. 5-fold cross validation was applied during model selection on the training set. Relative performance of the models was assessed by comparing area under the receiver operating characteristic curve (AUROC).

Mean shape, texture, and appearance for each sex/ethnicity subgroup was calculated. The derived MetS prediction models were applied to the mean images to estimate prevalence of MetS within each subgroup. For comparison, equivalent logistic regression models were derived using BMI as a predictor and applied to the subgroup means.

The derived logistic regression equations were used to predict risk for MetS and diabetes for the calculated mean fat appearance for each sex and ethnicity subgroup. The resulting risk estimates were compared against the observed prevalence of MetS and diabetes in the dataset.

4.3.3 Results

1,861 participants completed the study protocol. Of these, six were excluded from the present analysis due to significant DXA scan artifacts (e.g. metal implants). Statistical appearance

models were generated for each of lean and fat tissue using the 1,855 valid DXA images at a resolution of 64,000 pixels. A summary of included participant characteristics is provided in Table 4-4. Body mass index, fat mass index, and lean mass index for each subgroup are shown in Figure 4-17. 95% of body shape variance for males and females was compactly captured in 23 and 21 principal components, respectively. More modes were required to capture 95% of variance in fat and lean appearance, and over 150 were required to capture 95% of fat and lean texture. Correlations between shape, texture, and appearance principal components and metabolic markers of interest are shown in Table 4-5 and Table 4-6 for males and females, respectively.

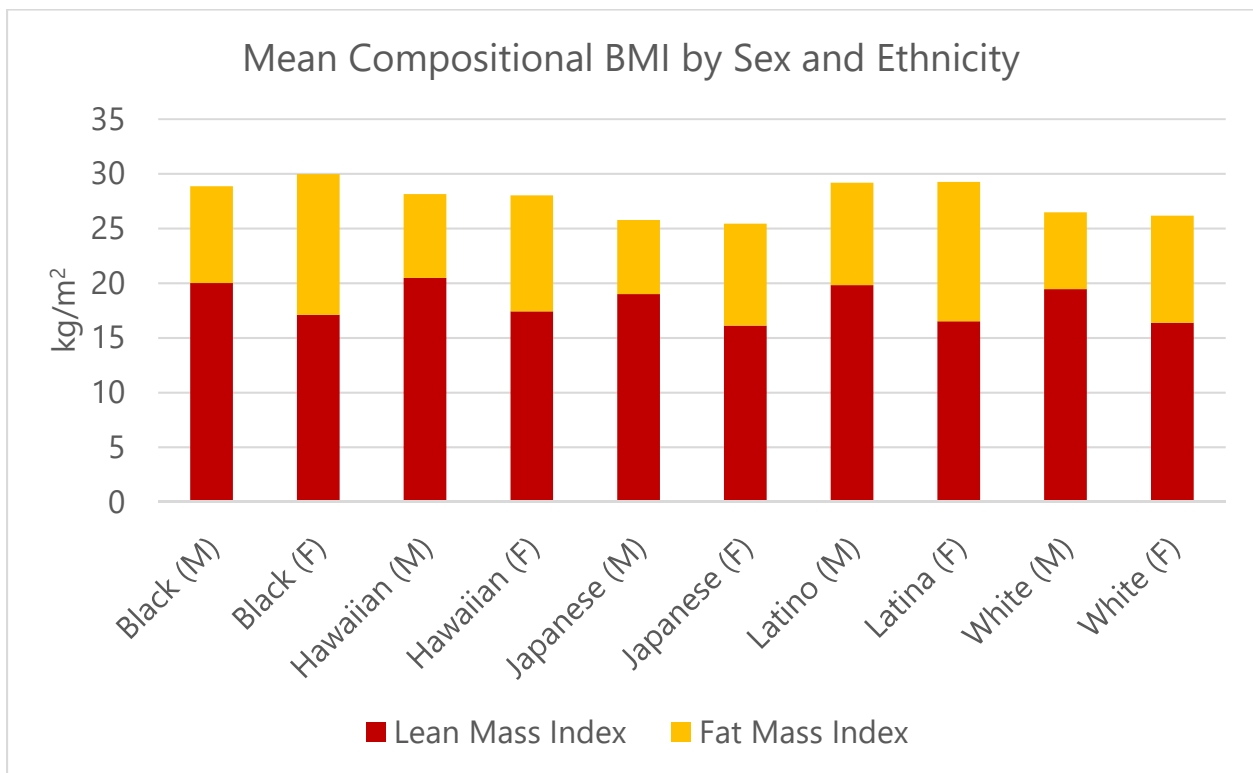


Figure 4-17: Mean body mass index and fat/lean composition by sex/ethnicity subgroup.

Mean fat texture by sex (across all ethnicities), and by sex and ethnicity subgroup were calculated. Subgroup images were subtracted from the overall sex mean and plotted in Figure 4-18.

Marked differences, particularly in the trunk versus leg regions, are apparent. For example, Caucasian individuals exhibit greater-than-average adipose deposition in the legs, but lower-than-average deposition in the trunk. The converse is apparent in the mean images for Latino individuals. Hawaiian men and women appear to have greater-than-average adipose deposition around the hips, but do not otherwise appear significantly different than the mean fat distribution. Notably, the characteristic fat distributions for each ethnicity appear consistent across sexes. Corresponding analysis was performed for the lean tissue texture. The resulting images are shown in Figure 4-19. The logistic regression models derived to predict MetS and diabetes status as a function of fat appearance modes are shown in Table 4-7. In general, models seem to perform better (in terms of higher AUROC) in the male sample than the female sample. BMI unsurprisingly remains a strong predictor of MetS (overall body size, measured by waist circumference, is one of the diagnostic criteria for MetS); it is not immediately clear that SAM analysis provides better insight. However, shape and appearance models significantly outperform BMI as predictors for diabetes status.

The derived logistic models were applied to the synthesized mean fat appearance of each sex/ethnicity subgroup, thus predicting risk of MetS for each subgroup. Risk estimates were normalized to the estimates for each sex, across all ethnicities, and compared to the actual observed prevalence of MetS in the sample population. These results are shown in Figure 4-20.

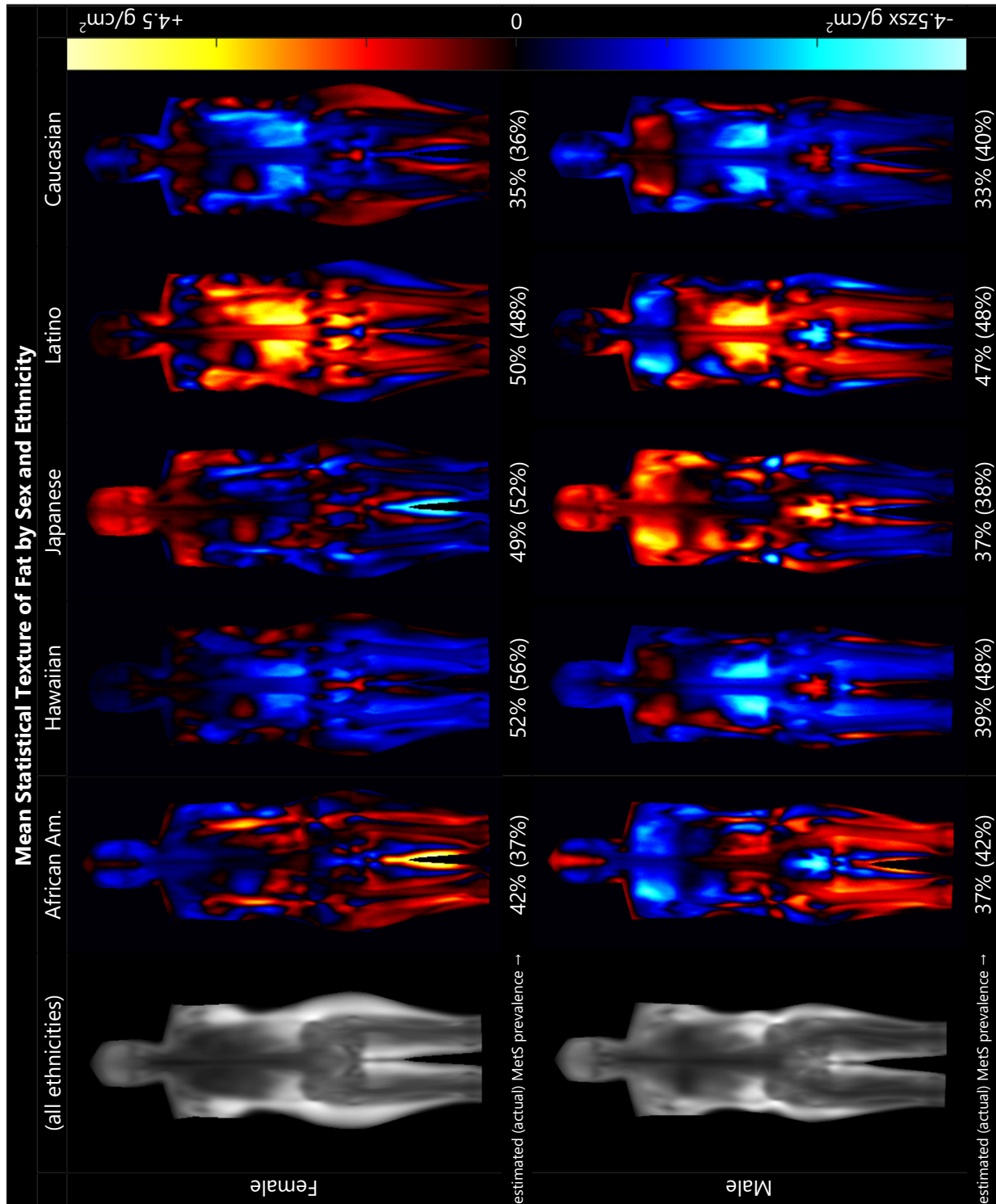


Figure 4-18: Weighted mean statistical texture of whole-body DXA fat by sex and ethnicity. The mean fat texture of each subgroup is shown relative to the overall means across all ethnicities. Marked differences, particularly in the trunk and leg regions, are apparent. Notably, fat distributions for each ethnicity are consistent across sexes.

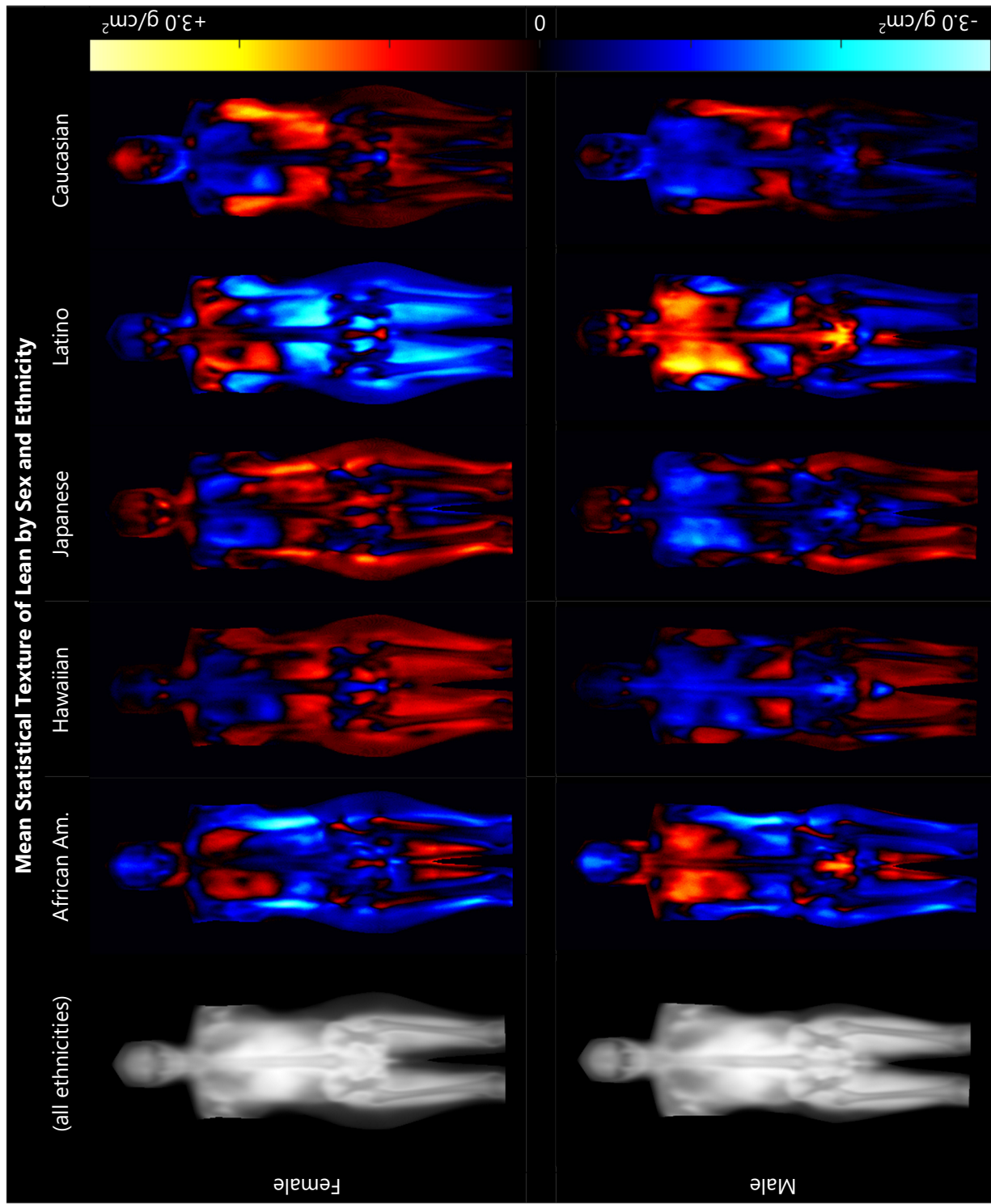


Figure 4-19: Weighted mean statistical texture of whole-body DXA lean by sex and ethnicity. The mean lean texture of each subgroup is shown relative to the overall means across all ethnicities.

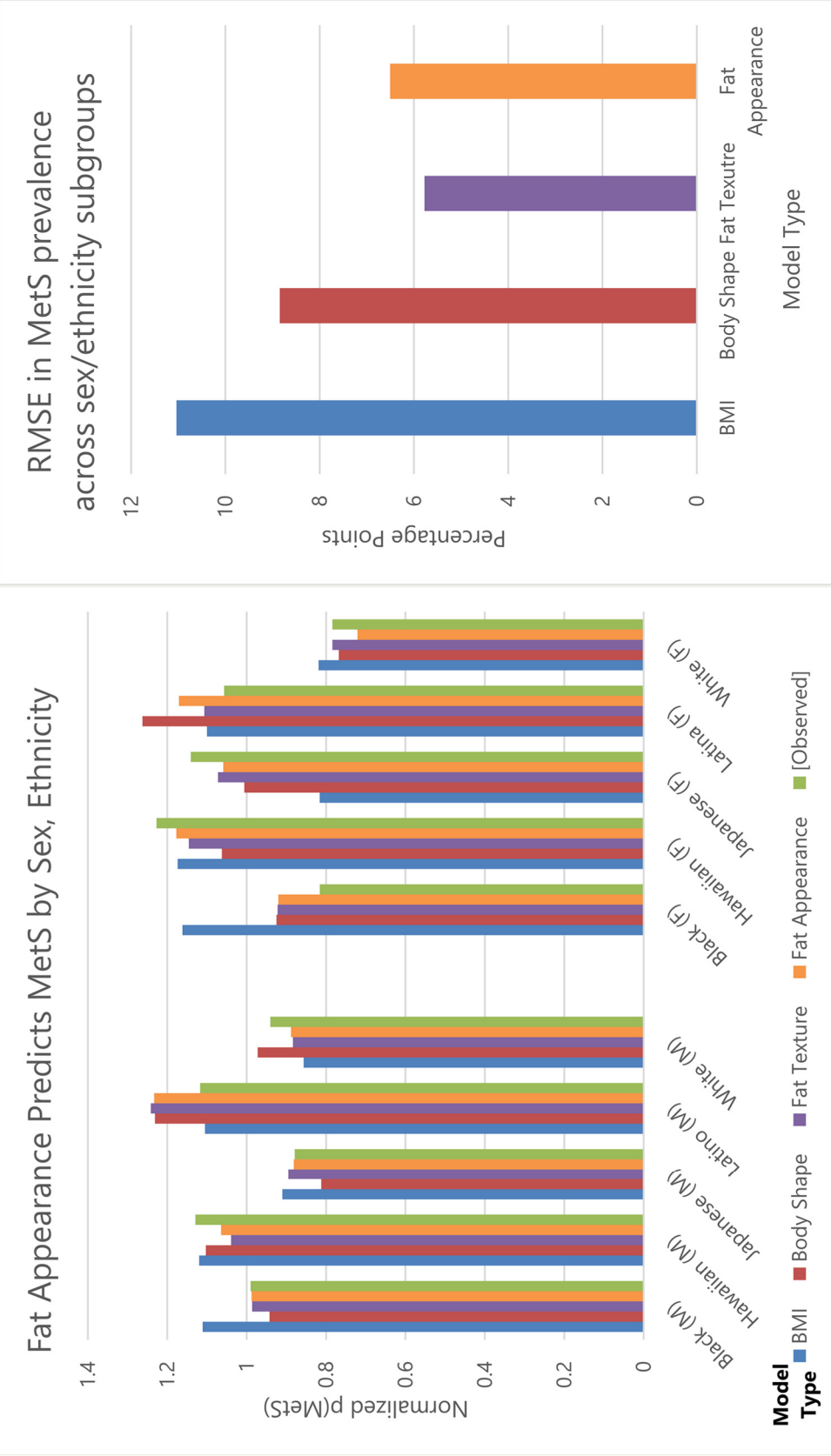


Figure 4-20: Estimated risk of MetS for each sex/ethnicity subgroup. These estimates were created by applying the logistic regression models (Table 4-7) to the weighted subgroup means of BMI, shape, and fat appearance (texture image shown in Figure 4-18 and Figure 4-19). Estimates were compared to actual observed prevalence of MetS (grey columns on left chart). It can be seen that fat appearance models produce lower RMSE in MetS risk estimates than corresponding body shape and BMI models, supporting the idea that fat appearance holds metabolically significant information beyond traditional shape descriptors.

Table 4-4: Demographic characteristics of the 1855 (916 male) participants included in this analysis. Continuous variables are reported as [mean (standard deviation)] unless otherwise noted.

Sex	Male (n=919)					Female (n=936)				
	African American	Native Hawaiian	Japanese	Latino	White	African American	Native Hawaiian	Japanese	Latino	White
Ethnicity										
Count, %	131, 14.3%	141, 15.4%	230, 25.1%	201, 21.9%	213, 23.3%	182, 19.6%	161, 17.3%	203, 21.8%	190, 20.4%	196, 21.0%
Age (yrs)	70.4 (3.0)	69.0 (3.3)	68.8 (2.5)	69.9 (2.7)	68.8 (2.4)	69.7 (2.4)	68.2 (3.5)	68.9 (2.5)	69.6 (2.7)	69.1 (2.3)
Height (cm)	176.3 (6.9)	171.8 (6.6)	167.5 (5.7)	169.5 (6.0)	175.6 (6.9)	163.1 (6.3)	158.5 (5.8)	154.2 (5.3)	155.7 (6.6)	161.5 (6.3)
Weight (kg)	88.4 (13.7)	85.2 (16.2)	74.1 (12.2)	83.5 (14.7)	83.6 (14.2)	79.6 (16.3)	72.3 (13.7)	61.9 (11.0)	70.4 (12.9)	69.8 (13.3)
BMI (kg/m ²)	28.5 (4.2)	28.9 (4.9)	26.4 (3.8)	29.0 (4.4)	27.2 (4.4)	29.9 (5.6)	28.8 (5.1)	26.1 (4.4)	29.1 (5.1)	26.8 (4.9)
Waist Circ. (cm)	97.9 (10.6)	101.2 (12.7)	94.2 (10.7)	99.6 (11.3)	99.5 (12.1)	91.7 (13.0)	96.8 (12.8)	91.7 (10.8)	90.4 (11.3)	94.1 (13.7)
Percent Fat	30.3 (4.7)	26.7 (4.7)	25.8 (4.4)	31.6 (4.4)	26.0 (5.0)	42.3 (4.7)	37.3 (4.5)	36.2 (4.2)	43.0 (4.4)	36.7 (5.3)
Fasting Glucose (mg/dL)	103.4 (27.4)	118.3 (41.8)	115.2 (25.9)	115.0 (40.4)	107.0 (24.1)	96.6 (27.3)	108.6 (28.5)	112.0 (28.1)	103.8 (36.8)	104.4 (22.3)
Insulin (μU/mL)	7.8 (5.3)	6.5 (4.4)	6.9 (4.6)	8.4 (5.2)	6.5 (4.6)	7.3 (4.5)	7.9 (6.0)	6.8 (4.9)	8.3 (5.5)	5.3 (2.9)
LDL Cholesterol (mg/dL)	116.9 (54.4)	123.2 (52.3)	119.4 (45.4)	120.3 (45.7)	124.5 (48.5)	129.0 (47.7)	132.0 (51.8)	127.2 (50.9)	135.2 (49.4)	143.7 (52.5)
Systolic BP (mmHg)	141.0 (19.0)	142.8 (15.9)	137.2 (15.4)	138.1 (16.0)	135.4 (17.3)	137.3 (15.5)	142.8 (20.0)	136.7 (18.3)	137.5 (19.1)	132.4 (17.6)
Diastolic BP (mmHg)	82.4 (11.6)	81.3 (10.8)	79.0 (10.0)	78.4 (9.7)	76.6 (9.9)	79.6 (10.7)	79.8 (11.5)	77.0 (11.3)	74.3 (9.6)	74.4 (10.6)
Visceral Adipose Area (cm ²)	150.2 (47.2)	141.0 (56.4)	144.0 (55.3)	186.9 (56.0)	142.7 (66.1)	133.1 (53.2)	130.5 (57.7)	124.3 (53.0)	159.4 (57.7)	110.7 (54.1)

Table 4-5: Correlations between shape, texture, and appearance modes and metabolic markers of interest (male)

Sex	Model Type	PC Number	Waist Circ.	Percent Fat	Fasting Glucose	Insulin	LDL Cholesterol	Systolic BP	Visceral Adipose	
Male	Shape 23 PCs capture 95% of variance	1	0.551	0.505	0.117	0.456	-0.077	0.104	0.524	
		2	0.277	0.267		0.117			0.144	
		3		0.086	0.092	0.069				0.171
		4	0.126	0.216	0.078	0.076				0.152
		5	-0.392	-0.385		-0.172			-0.121	-0.304
		6	-0.219						-0.084	
	Fat Texture >150 PCs capture 95% of variance	1	0.738	0.918	0.107	0.524			0.201	0.759
		2	-0.260	0.083	0.095					0.231
		3	0.390		0.177	0.297			0.127	0.352
		4		0.066		-0.113				
		5			-0.143			0.079		
		6		-0.080						-0.068
	Fat Appearance 52 PCs capture 95% of variance	1	-0.752	-0.850	-0.123	-0.560		0.073	-0.182	-0.748
		2	0.125	0.324						0.139
		3		0.134	0.138	0.071			0.074	0.236
		4	0.108	0.084						
		5			-0.078					-0.072
		6	-0.312	0.083					-0.083	0.085
Lean Texture >150 PCs capture 95% of variance	1	-0.878	-0.459	-0.132	-0.523		0.071	-0.209	-0.642	
	2	0.222	0.748		0.254				0.437	
	3			0.122					0.192	
	4		-0.082		-0.093			-0.081		
	5			0.100	0.070			-0.072	0.206	
	6	0.078		-0.070			-0.186			
Lean Appearance 77 PCs capture 95% of variance	1	0.836	0.586	0.141	0.570		-0.086	0.183	0.685	
	2	-0.306	0.108					-0.089	-0.067	
	3	0.143	0.515		0.110				0.236	
	4		-0.236	-0.143	-0.110			-0.076	-0.286	
	5	0.119	0.336		0.073				0.157	
	6									

Significant correlations (p<0.05) shown. Shading denotes (p<0.01)

Table 4-6: Correlations between shape, texture, and appearance modes and metabolic markers of interest (female)

Sex	Model Type	PC Number	Waist Circ.	Percent Fat	Fasting Glucose	Insulin	LDL Cholesterol	Diastolic BP	Visceral Adipose	
Female	Shape 21 PCs capture 95% of variance	1	0.582	0.624	0.087	0.367		0.145	0.609	
		2	0.154	0.344	-0.099					
		3	0.105	0.124	0.175	0.163			0.201	
		4				0.096				
		5	-0.170	-0.222			-0.080		-0.064	-0.103
		6		0.127						0.136
	Fat Texture >150 PCs capture 95% of variance	1	-0.668	-0.892			-0.388		-0.218	-0.712
		2	-0.183		-0.223		-0.325		0.102	-0.392
		3	0.410	-0.143			0.139		0.207	
		4								-0.117
		5	-0.109				0.106			0.151
		6			0.114				-0.140	
	Fat Appearance 50 PCs capture 95% of variance	1	-0.681	-0.837	-0.071		-0.407		-0.200	-0.716
		2		0.297	-0.090				0.081	
		3	-0.154		-0.247		-0.304			-0.382
		4					0.079		-0.098	
		5	0.067				0.081			0.146
		6							-0.137	0.137
Lean Texture >150 PCs capture 95% of variance	1	-0.850	-0.393	-0.190		-0.428		-0.279	-0.651	
	2	0.174	0.768			0.182			0.409	
	3			0.093		0.092			0.120	
	4			0.077		-0.077		-0.094		
	5	0.071	-0.163	0.214		0.280		-0.150	0.303	
	6	-0.077	0.117	-0.107					0.114	
Lean Appearance 77 PCs capture 95% of variance	1	-0.814	-0.615	-0.152		-0.453		-0.240	-0.726	
	2	-0.281	0.298	-0.108				-0.145		
	3		0.486	-0.071					0.115	
	4	-0.082	-0.093	-0.222		-0.200			-0.273	
	5					-0.126				
	6		-0.248			-0.078			-0.187	

Significant correlations (p<0.05) shown. Shading denotes (p<0.01)

Table 4-7: Logistic regression equation performance for MetS and diabetes status as a function of fat shape, texture, and appearance modes. Data were randomly assigned to training (80%) or validation (20%) sets.

Outcome Variable	Sex	Model Type	# of selected PCs	Training AUC	Validation AUC
Metabolic Syndrome	Male	Shape	41	0.86	0.82
		Fat Texture	69	0.89	0.84
		Fat Appearance	63	0.90	0.83
		Lean Texture	60	0.89	0.85
		Lean Appearance	47	0.89	0.85
		Combined	29	0.87	0.87
	Female	Shape	26	0.83	0.78
		Fat Texture	13	0.84	0.80
		Fat Appearance	30	0.86	0.80
		Lean Texture	43	0.88	0.81
		Lean Appearance	46	0.88	0.82
		Combined	7	0.84	0.82
Diabetes	Male	Shape	31	0.74	0.69
		Fat Texture	43	0.78	0.70
		Fat Appearance	76	0.80	0.70
		Lean Texture	2.	0.74	0.71
		Lean Appearance	49	0.79	0.73
		Combined	29	0.77	0.75
	Female	Shape	38	0.76	0.66
		Fat Texture	22	0.75	0.63
		Fat Appearance	7	0.70	0.66
		Lean Texture	79	0.82	0.67
		Lean Appearance	65	0.82	0.68
		Combined	47	0.80	0.68

Parameters for each model were selected using stepwise regression subject to minimization of the Schwarz-Bayesian Information Criterion

4.3.4 Discussion

In this work we demonstrate statistical appearance modeling of whole-body fat and lean distribution from whole-body DXA images. Using unsupervised principal component analysis, we identify metabolically-significant modes of variation in fat and lean distribution. These models reveal sex- and ethnicity-specific fat distribution phenotypes that are likely the product of genetic and lifestyle characteristics. Further analysis against other -omic variables may provide insight into the complex mechanisms that dictate the macroscopic manifestation of body shape and composition. That these unsupervised models produce predictive indicators of metabolic syndrome and diabetes status suggests that the spatial distribution of body tissues is metabolically significant. This supports several previous works that have demonstrated the significance of visceral fat versus subcutaneous fat, as well as android adiposity versus gynoid adiposity. Holistic analysis of high-resolution whole-body compositional images provides a means of identifying new markers for metabolic health.

This study had a few limitations. First, the recruitment was limited to a narrow age range and was not evenly distributed across sex and ethnicity subgroups. Analysis of a larger distribution of ages, ethnicities, and BMIs would produce models that better represent the wide variation in body shapes and size. Further investigation of special populations such as those affected by sarcopenia or lymphedema would yield valuable insight into unusual body compositions and metabolic states. A second issue was slight pose variations in the DXA images. This introduced positioning noise that could be seen in a number of statistical appearance modes. Careful positioning at the time of scanning, as well as careful image registration should ameliorate this issue. In future studies we plan

to investigate the metabolic significance of specific sub-regions of the body, registered across all individuals in the sample.

A significant advantage of the presented technique is that it utilizes conventional whole-body DXA data. No additional measurements are required to perform this analysis. Thus, it is possible to apply this technique to numerous large DXA datasets from various studies on numerous populations. Coupled with advanced methods of supervised learning and computer vision, this provides a platform for identifying new biomarkers from established imaging techniques.

5 | 3D Surface Scanning for Metabolic Health Assessment

5.1: Clinical Anthropometrics from Commercial 3D Body Scanners

5.1.1 Introduction

Regional body shape and composition provide stronger indicators of obesity-related metabolic risk than body mass index (BMI). Goodpaster et al. showed that normal weight men with high visceral adipose levels were twice as likely to have metabolic syndrome [167]. Wilson et al. showed that the individuals in the highest quintile of trunk to leg volume ratio are at 6.8 times greater risk for diabetes [73]. Common methods for body composition assessment include bioelectrical impedance analysis (BIA), air displacement plethysmography (ADP), and dual-energy X-ray absorptiometry (DXA). Of these, DXA is the only method that provides regional information, but DXA is not suitable for large populations due to its relatively high cost and use of ionizing radiation. There is an unmet need for accessible tools for accurate regional body composition assessment.

We investigated the use of 3D whole-body surface scanning for clinical anthropometry as well as total and regional body composition measurement. These systems generate surface renderings and automated circumference and length measurements across the entire body. Several studies have assessed their ability to accurately and precisely quantify clinically-relevant measures. Wells, et al. reported 0.5 cm precision on body circumferences (chest, waist, hips, etc.) using a six-camera structured light scanner [114]. Wang, et al. reported precise (%CV=0.38) whole-body volume measurements using a four-camera laser-triangulation scanner [115]. Lin, et al. reported correlations between 3D anthropometric measures and metabolic risk factors [168], [169]. Lee, et al.

demonstrated accurate prediction of whole-body and regional fat mass and percent fat from regional volume and length measures from an eight-camera structured illumination scanner [128].

Development of low-cost light-coding technology has enabled more affordable 3D scanners such as the TC² KX-16 (Cary, NC) [170] and the Fit3D ProScanner (Redwood City, CA).

In summary, 3D body surface scanning is a compelling tool for metabolic status assessment that offers inexpensive, radiation-free, and automated collection of hundreds of measurements that would otherwise require significant time and personnel resources to collect. The objective of this study was to validate direct anthropometric and derived body composition measurements from 3D whole-body surface scans against criterion methods.

5.1.2 Methods

We conducted a cross-sectional stratified study of healthy adults. 3D scan measurements (circumferences, surface areas, and volumes) were systematically compared to manual anthropometry, DXA, and ADP. Predictive equations were derived to estimate DXA body composition using 3D scan measurements.

Participants

There were two participant groups: a calibration group and field validation group. Calibration participants were recruited using flyers posted around UCSF between January 2014 and May 2015. Calibration group recruitment was stratified by age (20-40, 40-60, 60+ years), sex, and BMI (normal < 25 kg/m², 25 kg/m² ≥ overweight < 30 kg/m², obese ≥ 30 kg/m²). Eligible participants were identified as ambulatory individuals within the study strata. Exclusion criteria included current

pregnancy, missing limbs, non-removable metal in the body (e.g. joint replacements), a history of body-altering surgery (e.g. liposuction), and significant hair that cannot be contained within a swim cap. Each calibration participant underwent a whole-body DXA scan and two 3D optical scans, with repositioning. Weight, height, and waist and hip circumferences (each in duplicate) were recorded. All measures were acquired at the UCSF Clinical and Translational Science Institute (CTSI) Body Composition, Exercise Physiology and Energy Metabolism Laboratory (San Francisco, CA). Calibration participants gave informed consent and the study protocol was approved by the UCSF Committee on Human Research.

Participants in the field validation group were scanned at one of eight fitness centers in the United States and Australia for body shape self-assessment purposes between July and November 2014. Each participant had a BIA percent fat measurement and a 3D body scan on the same day. Validation participants were selected to have height, weight, BMI, and age measurements within the minimum-maximum ranges of the calibration dataset. It should be noted that BIA measurements were user-reported, and the BIA hardware and acquisition protocols were uncontrolled. All field validation participants signed a waiver of consent authorizing the use of their anonymized scans by the investigators.

3D surface scans

3D surface scans were acquired on a Fit3D ProScanner (Fit3D Inc., Redwood City, CA) according to a standard protocol. The device consists of a rotating platform and a 3D optical light-coding camera mounted in a tower two meters from the center of the platform. Users grasp adjustable handles mounted on the platform such that their arms are straight and relaxed, abducted

from the body. When buttons on the scanner handles are depressed by the user, a 360-degree 3D image is acquired while the platform rotates once around in approximately 40 seconds. Although only 11 circumferences (chest, waist, and hips; as well as left/right biceps, forearm, thigh, and calf) are reported to end users, 476 anthropometric measurements from the neck down to the ankles and wrists are automatically derived and stored in a proprietary database. In general, the head, hands, and feet are excluded from all circumference, surface area, and volume calculations. The Fit3D system was chosen for this study over other models because approximately 100 of these systems are available to the public at fitness centers across the US.

Each calibration participant was scanned twice, with repositioning. Form-fitting boxer briefs and a swim cap were provided for each participant. Male participants were scanned topless while female participants wore a sports bra. Each validation participant was scanned once, in personal form-fitting clothing, with long hair tied above the neck. 3D scan data and measurements were transferred securely from Fit3D to UCSF.

For quality control we performed 41 scans of a female mannequin (part #DSPEFAMW, Display Warehouse, San Diego, CA) with repositioning over a two-month period (data not included). Chest, hip, thigh, and waist circumference as well as total body volume showed high long-term stability with coefficients of variation between 0.25 and 1.2%.

DXA

Only calibration participants received a DXA scan as the criterion method for body composition. Whole-body scans were acquired on a Hologic Discovery/W or Horizon/A system

(Hologic Inc., Marlborough, MA). All scans were centrally analyzed at UCSF by a single ISCD-certified technologist using Hologic Apex software (version 13.5.2.1) and NHANES calibration [132]. Participants were scanned in examination gowns, without shoes. Participants were centered on the scanner table with arms out to the side, hands flat on table, and feet in planarflex position, in accordance with the manufacturer's standard protocols. The standard DXA output includes percent fat, fat mass, lean mass, and total mass for the whole body as well as the arms, legs, torso, and head. In addition, total and regional body volumes were derived for each region on the DXA report (arms, legs, trunk, whole body) using the equations of Wilson et al. [151].

ADP

Only calibration participants received an ADP measurement as the criterion method for total body volume. Measurements were performed using a Bod Pod (COSMED USA, Inc., Chicago, IL). Before each measurement, the instrument was calibrated by placing a hollow cylinder with known volume into the Bod Pod. Participants wore the same outfit for the ADP measure as for the 3D optical scan (swim cap, boxer briefs, and a sports bra for females). Body volume is measured by the body's air displacement with corrections for residual lung volume and surface area artifacts. Details of the standard ADP protocol are described elsewhere [90].

Statistical Methods

All analyses were performed using SAS version 9.4 (SAS Institute, Cary, NC). Univariate linear regressions were performed to assess agreement of selected clinically-relevant anthropometric measurements acquired on the 3D scanner versus criterion methods: hip and waist circumference tape measurements, body surface area estimated using the Du Bois model (12), and whole/regional

body volumes calculated from ADP and DXA, respectively. Student's t-tests were performed to detect significant measurement biases between 3D measurements and criterion methods.

Measurements were assumed to be normally distributed. A critical P-value of 0.05 was considered significant. Coefficients of variation (%CV) and root mean square error (RMSE) were calculated for the matched test-retest measurements from the 3D optical scanner. Coefficients of determination (R^2) reported in this study are adjusted for multiple variables where applicable.

Predictive equations were derived for whole-body and regional DXA body composition variables, including percent fat, fat mass, and visceral fat mass. Where available, we derived linear regression equations using the parameters described by Lee [128], [171]. The ratio of waist girth to waist width was used as a surrogate for “central obesity depth” defined by Lee. Waist girth and width were likewise used as surrogates for “central obesity width” as defined by Lee. We further derived predictive equations for fat free mass in each compartment (whole body, legs, and trunk) using the same parameters as the fat mass equations. Equations were derived using linear regression (proc GLM). Additional equations were derived for fat and lean mass in the arms, by using stepwise linear regression (proc GLMSELECT, selection=STEPWISE) and over 18 length, area, and volume measurements of the arms and trunk. Selection was performed subject to minimization of the Schwarz-Bayesian Information Criterion, with 5-fold cross validation on the calibration data.

Since DXA scans were acquired on two different systems (Horizon/A and Discovery/W), we performed covariate analysis on each equation to determine whether cross calibration was necessary. Adjusting for age, height, and weight, no significant differences were found between the two scanners for all predicted variables except visceral fat. Consequently, all measurements except visceral

fat were pooled directly between the two scanners. Visceral fat measurements acquired on the Discovery/W were calibrated to the Horizon/A using a linear calibration equation derived from a separate study of 13 participants who underwent sequential whole-body scans on the two scanners (unpublished work).

Whole-body prediction equations were applied to the field validation data. Estimated whole-body percent fat, fat mass, and fat free mass were compared to the reported values from bioelectrical impedance analysis using simple linear regression.

5.1.3 Results

39 individuals (20 male) completed the calibration study. 37 individuals (18 male) were included in the validation group. Summary statistics of the calibration and validation populations are provided in Table 5-1. Example 3D optical and DXA images are shown in Figure 5-1.

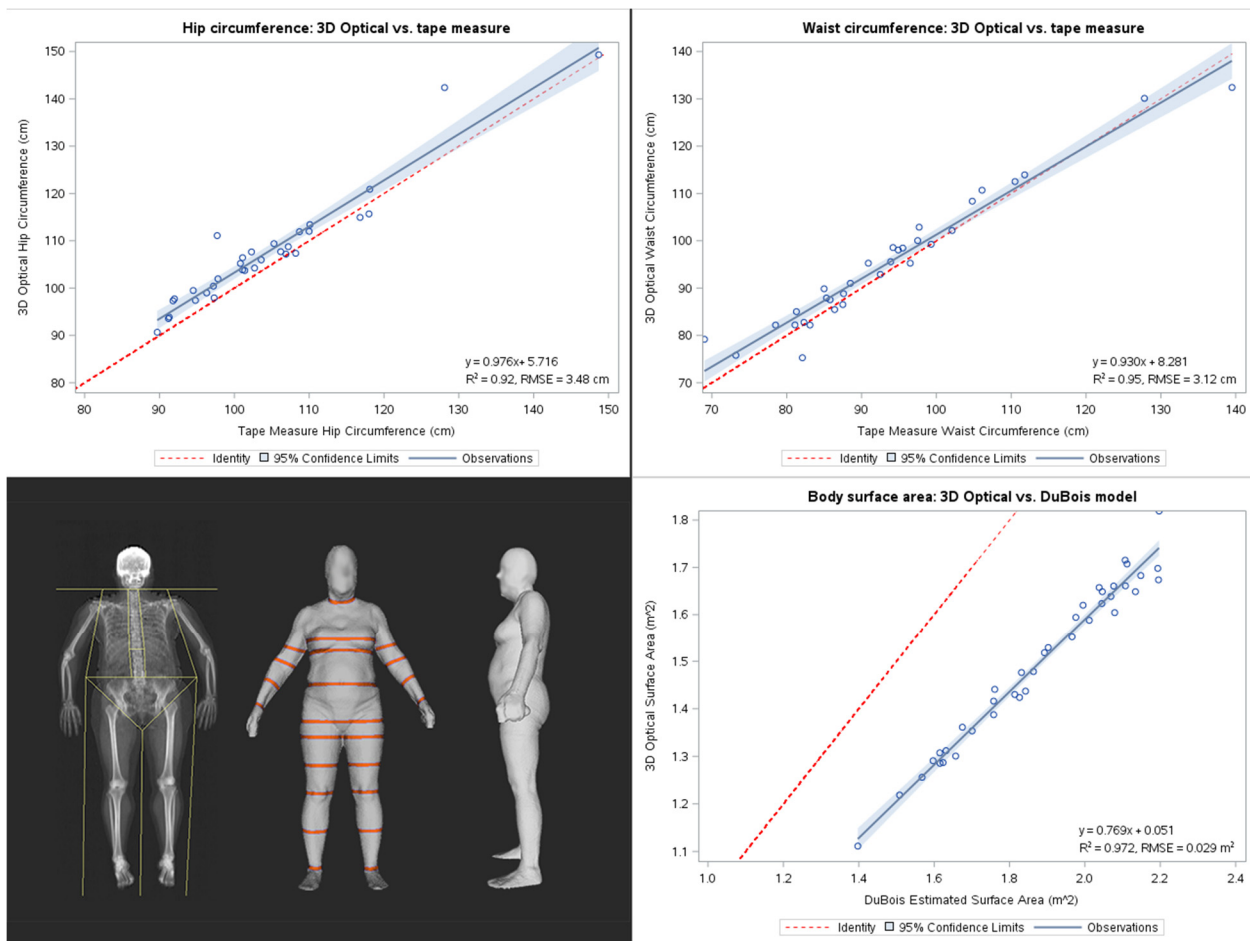


Figure 5-1: 3D scanner body circumferences and surface area vs. criterion methods. Clockwise from top left: hip circumference, waist circumference, and body surface area comparisons, then sample matched DXA and 3D optical images with annotated landmarks. 3D circumferences and surface area show high correlation with manual tape measures. Biases may be the result of non-identical landmark positioning between the methods. Of note, body surface area shows significant bias that may be explained by the fact that the 3D scanner software does not report surface area of the head and neck. This omission is not a technical shortcoming, but a design decision by the manufacturer to avoid inaccuracies introduced by voluminous hair.

Regression plots are shown in Figure 5-1 for 3D optical measurements against tape measure circumferences and Du Bois-estimated body surface area. Figure 5-2 shows 3D measurements against DXA and ADP whole-body volumes, and DXA regional volumes. Strong association was observed for waist and hip circumferences ($R^2=0.95$ and 0.92 , respectively). T-tests showed significant mean differences of 1.75 cm (95% CI: [0.58, 2.91]) for waist circumference and 3.17 cm (95% CI: [1.93, 4.41]) for hip circumference between the 3D scanner and tape measurements.

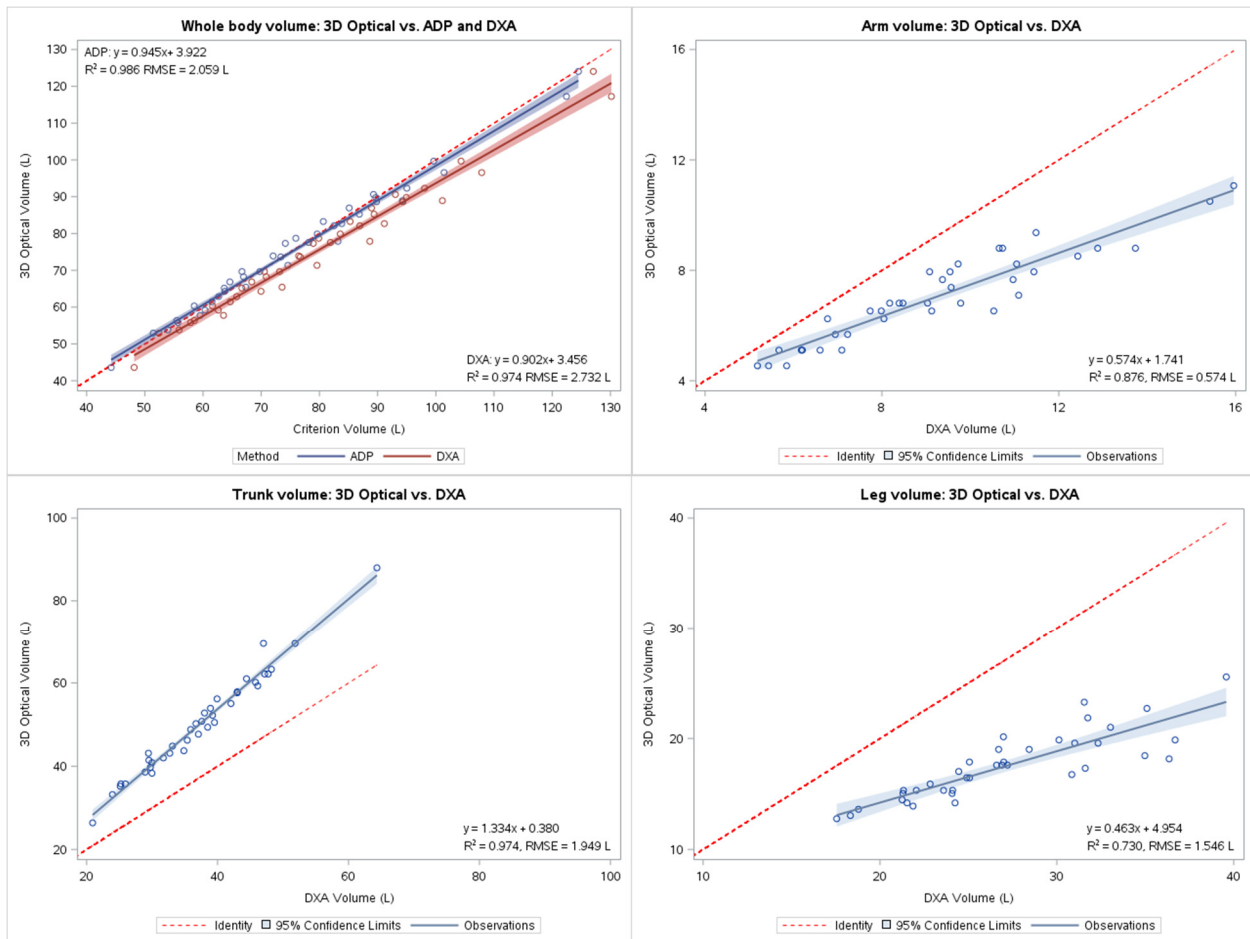


Figure 5-2: 3D scanner body volume vs. criterion methods. Clockwise from top left: total volume vs. ADP and DXA, arms vs. DXA, legs vs. DXA, and trunk vs. DXA. High precision and accuracy is observed for whole-body volume. Due to differences in partition locations, regional measurements are not directly comparable between the 3D scanner and DXA. For instance, the legs are partitioned horizontally at the crotch in the 3D optical system, but diagonally from the crotch up to the top of the hip in the DXA system. Consequently, reported leg volumes are lower on the 3D system than the DXA system. Refinement of the regional partitions is necessary before cross-modality comparisons can be performed.

Surface area and volume measurements from the 3D scanner showed high test-retest precision (Table 5-2). Strong association to the Du Bois model was observed for whole-body surface area ($R^2=0.97$), although this 3D system significantly underreports surface area (mean difference -0.38 m^2 , 95% CI: $[-0.40, -0.36]$). Similarly, strong associations to ADP- and DXA-measured whole-body volumes were observed ($R^2=0.99$ and 0.97 , respectively) with a significantly smaller 3D scan measured volume relative to ADP (mean difference -4.15 L, 95% CI: $[-5.13, -3.17]$). Regional 3D scan volume estimates were highly correlated to similar measures derived from the DXA scans

($R^2=0.73 - 0.97$). In general, the 3D scanner includes less volume in the arm and leg compartments than DXA, and correspondingly more volume in the trunk compartment (all $P < 0.001$).

Table 5-1: Summary statistics of the model calibration population and validation groups. Reported circumferences, areas, and volumes were derived from the 3D optical scans. Unpaired two-tailed t-tests were performed to detect significant mean differences in the direct 3D measurements between the two groups (P-values shown in the right-most column, * denotes $P \leq 0.05$). Note that body composition was measured using DXA on the calibration group and BIA on the validation group.

Variable	Calibration (N=39, 20 male)			Validation (N=37, 18 male)			P-val.
	Mean (SD)	Min	Max	Mean (SD)	Min	Max	
Age (years)	44.3 (15.5)	21.6	72.5	42.6 (11.5)	23.1	62.9	0.60
Height (cm)	169.5 (9.7)	152.4	190.5	174.1 (8.3)	160.0	190.5	0.03*
Mass (kg)	78.0 (17.6)	46.8	123.6	80.0 (10.5)	61.0	100.0	0.56
BMI (kg/m²)	27.5 (6.5)	20.3	51.0	26.4 (3.2)	22.2	34.2	0.36
3D Optical Measures							
Circumferences (cm)							
Waist	94.4 (13.6)	66.8	132.4	92.5 (7.2)	80.0	106.8	0.45
Hips	106.2 (11.8)	89.7	149.3	105.3 (7.1)	94.6	122.2	0.70
Biceps	34.3 (4.4)	26.6	45.2	35.0 (3.1)	28.9	41.8	0.44
Forearm	27.9 (2.7)	23.0	34.4	28.3 (2.5)	23.9	36.7	0.49
Thigh	61.8 (6.3)	53.1	80.4	62.4 (5.9)	53.4	80.4	0.67
Calf	39.6 (3.5)	32.0	49.7	39.5 (2.2)	34.3	44.6	0.87
Areas (m²)							
Torso	0.662 (0.095)	0.453	0.834	0.669 (0.076)	0.513	0.839	0.75
Left arm	0.129 (0.016)	0.102	0.153	0.135 (0.019)	0.068	0.164	0.11
Right arm	0.129 (0.015)	0.100	0.159	0.137 (0.013)	0.116	0.154	0.02*
Left leg	0.268 (0.029)	0.217	0.335	0.281 (0.027)	0.235	0.359	0.05*
Right leg	0.270 (0.029)	0.212	0.340	0.282 (0.028)	0.233	0.358	0.06
Volumes (L)							
Whole-body	75.8 (17.1)	43.7	124.3	76.9 (10.1)	57.6	98.5	0.74
Left arm	3.59 (0.87)	2.27	5.96	3.71 (0.68)	2.27	4.82	0.49
Right arm	3.50 (0.77)	2.27	5.39	3.74 (0.58)	2.55	4.82	0.12
Left leg	8.83 (1.56)	6.53	12.77	9.28 (1.52)	7.10	14.76	0.20
Right leg	8.82 (1.58)	6.24	12.77	9.35 (1.47)	7.10	14.47	0.14
Obesity indices							
Waist-Hip Ratio	0.89 (0.07)	0.73	1.00	0.88 (0.05)	0.76	0.99	0.56
Waist-Height Ratio	0.56 (0.08)	0.43	0.84	0.53 (0.05)	0.47	0.65	0.11
Body composition							
FMI (kg/m²)	9.0 (4.4)	3.9	25.1	6.4 (3.1)	2.1	13.5	<0.01*
FFMI (kg/m²)	18.4 (3.0)	12.9	26.8	20.0 (2.1)	15.7	24.5	0.01*
%Fat	31.7 (7.8)	17.8	50.0	23.7 (9.4)	8.0	39.5	<0.01*

The derived body composition equations for percent fat, fat mass, lean mass, and visceral fat mass are shown in Table 5-3. Validation results for the whole-body measurements is included. Fat

and fat free mass models exhibited strong fit to the calibration data ($R^2=0.95$ and 0.96) and a reasonable fit to the validation data ($R^2=0.76$ and 0.85). The visceral fat prediction equation showed moderately strong association ($R^2=0.75$). Predictive models for regional fat and lean mass showed generally strong associations on the calibration set ($R^2=0.79-0.94$), however no validation data was available for these regional models.

Table 5-2: Test-retest precision of measurements derived from the 3D optical scanner. Each participant in the calibration data set was scanned twice, with repositioning.

Measurement Type	Variable	%CV	RMSE
Circumference [cm]	Waist	1.50	1.41
	Hips	0.75	0.79
	Biceps	2.24	0.77
	Forearm	1.93	0.54
	Thigh	0.95	0.59
	Calf	0.92	0.36
Area [m ²]	Whole-body surface	1.38	0.0168
Volume [L]	Whole-body	0.74	0.57
	Average (L/R) arm	4.49	0.16
	Average (L/R) leg	2.61	0.23
	Trunk	0.99	0.51
Derived fat / fat free mass [kg]	Whole-body fat	1.96	0.50
	Whole-body fat free	0.94	0.50
	Whole-body percent fat [%]	2.16	0.68
	Visceral fat mass	6.69	0.03
	Trunk fat	2.38	0.30
	Trunk fat free	0.50	0.13
	Arms fat	11.63	0.34
	Arms fat free	6.67	0.42
	Legs fat	1.25	0.11
	Legs fat free	1.99	0.36

Table 5-3: Derived fat mass, fat free mass, and percent fat prediction equations from 3D optical measurements. Models were trained using gold-standard measurements from whole-body DXA scans. Whole-body models were validated against an external dataset that included scale weight and bioelectrical impedance measurements. Parameters were selected to validate previous work by Lee, et al. (11, 18).

Region	Variable	Prediction equation	Train R ² adj	Train RMSE	Valid R ² adj	Valid RMSE
Whole body	Fat mass [kg]	-19.06 + 4.05 (waist circumference / waist width) – 11.78 (average leg volume) - 10.48 (is male) + 22.29 (torso volume)	0.95	2.36	0.76	3.72
	Fat free mass [kg]	(measured mass) - (predicted fat mass)	0.96	2.24	0.85	3.14
	Percent Fat	(predicted fat mass) / (measured mass)	0.84	3.06	0.72	3.75
	Fat mass index [kg/m ²]	(predicted fat mass) / (measured height) ²	0.95	0.90	0.83	1.13
	Fat free mass index [kg/m ²]	(predicted fat free mass) / (measured height) ²	0.93	0.84	0.64	1.04
	Visceral fat mass [kg]	9.93 - 0.10 (is male) – 3.93 (waist circ / waist width) - 0.91 (waist width) + 1.31 (waist circumference / hip circumference) + 0.33 (waist circumference)	0.75	0.11		
Trunk	Fat mass [kg]	-22.49 + 5.67 (waist circ / waist width) + 11.71 (torso volume) - 4.71 (is male)	0.94	1.49		
	Fat free mass [kg]	11.00 - 0.65 (waist circ / waist width) + 7.31 (torso volume) + 5.31 (is male)	0.88	1.72		
Arms	Fat mass [kg]	0.54 - 1.01 (is male) - 0.0097 (torso surface area) + 6.25 (torso volume) + 47.92 (arm volume / body volume)	0.90	0.53		
	Fat free mass [kg]	-1.44 + 2.93 (is male) + 0.46 (average upper arm circumference)	0.92	0.55		
Legs	Fat mass [kg]	-3.72 + 0.51 (waist circ / waist width) + 8.61*(average leg volume) - 3.90 (is male) + 5.82 (torso volume)	0.79	1.69		
	Fat free mass [kg]	-8.46 + 3.26 (waist circ / waist width) + 44.17 (average leg volume) + 0.55 (is male) + 0.39 (torso volume)	0.84	1.60		

5.1.4 Discussion

In this study of automated anthropometric measures from 3D whole body surface scans, we found strong associations of waist and hip circumference to tape measured-values, body surface area to the Du Bois model, and body volumes to DXA volume estimates. 3D measures were used to derive whole-body and regional body composition estimates for both sexes across a wide range of ages and BMI values. The accuracy of these body composition estimates was validated in a separate dataset using BIA. Although some biases were found in the anthropometric measures, this study supports the use of 3D surface scanning as an accurate, precise, and automated substitute to other methods such as measuring tape, ADP, and DXA.

Notably, 3D scanning is a more direct measure of surface area than the criterion method (height/weight equation) available. In practice, there is no established gold standard for body surface area measurement. We found strong correlation between surface area measurements from the present 3D scanner and the clinically-prevalent Du Bois model ($R^2=0.97$). Tikuisis reported high precision and accuracy of a 3D laser scanner to six different height and weight equations for body surface area [172], but again, no gold standard comparison method was available. This measure is clinically relevant for modeling evaporative water loss, in particular for burn injuries [173] and calculating chemotherapeutic medication dosages [174].

Whole-body volume measurements from 3D scans exhibited high precision (%CV=0.74) comparable to ADP (%CV=0.10) [175]. Differences in landmark and partition positioning in the 3D surface scan analysis algorithms led to significant biases in regional volume measurements compared to DXA. For example, the present trunk/leg partition defined by the ProScanner is a

horizontal plane at the crotch. Whereas on a standard Hologic DXA, the trunk/leg partitions run diagonally from the crotch to the hips, such that the femur is completely in the leg compartment. Calibration to DXA compartments would enable direct assessment of trunk-to-leg volume ratio (2), a strong independent indicator of metabolic health and disease risk.

Body composition models from 3D features calibrated using DXA data validated well, similar to those reported by Lee [128], [129], especially in light of the different body composition measurement methods employed (DXA calibration data and BIA validation data in our study, and DXA and MRI data in Lee's studies). In particular, our whole-body fat mass prediction model showed strong fit to the calibration data ($R^2=0.95$), matching the equivalent Lee model ($R^2=0.95$) [128]. Our visceral fat prediction model showed moderately strong association ($R^2=0.75$), similar to Lee ($R^2=0.72$) [171].

This study had a few limitations. Small sample size ($n=39$) limits the statistical power of our models. However, all age/BMI/sex strata defined for this study were represented. Another issue was that the validation data contained only BIA body composition data rather than DXA data. This BIA data was reported by users rather than trained technicians with a defined protocol. Despite these limitations, the strong validation results suggest good predictive model stability across a range of body shapes in a real consumer environment. Lastly, our findings were derived from a healthy population without any known conditions that may alter the relationship between 3D body shape and body composition such as sarcopenia, anorexia, or malnutrition.

We conclude that 3D surface scanning presents a compelling modality for clinical anthropometry. This method provides an accessible platform for rapid body measurement as well as total and regional body composition analysis. Due to low cost, high precision, and a lack of ionizing radiation, 3D surface scanning is uniquely suitable for routine clinical use to monitor longitudinal metabolic health. This study shows feasibility of broad clinical use of 3D surface scanning to estimate body composition in a wide range of body shapes. Larger follow-up studies are justified to better understand the relationships of 3D body shape and composition across various sex, BMI, age, and ethnicity groups, as well as in special populations with metabolic conditions and potentially abnormal body composition.

5.2: The Shape Up! Studies

The pilot investigation reported in the preceding section formed the preliminary results that were submitted as part of the Shape Up! Adults and Shape Up! Kids studies (funded by NIH R01 DK109008 and R01 DK111698, respectively). These studies are currently underway to measure 3D body shape and a variety of metabolic markers in 1440 children and adults from age 18-80. Some of the first findings from this study are reported below.

5.2.1 Introduction

Excess adiposity plays a central role in the development of type 2 diabetes, cardiovascular disease, and several cancers [140], [176], [177]. Distinguishing between adipose tissue and functional lean tissues is vital to understanding overall health and the risk of developing chronic diseases. Body mass index (BMI) is a widely used proxy for body composition that fails to independently estimate the two major body compartments, fat mass (FM) and fat-free mass (FFM)

[178]. Clinicians and investigators have long used anthropometric assessments to estimate body fat mass and FFM. A typical assessment may include manual measurement of height, weight, waist, trunk, and extremity circumferences, and multiple skin-fold thicknesses [74]. These measurements provide information about the regional distribution of tissues across the body to more accurately separate body mass into fat and fat-free mass components.

In practice, manual anthropometry assessment relies on well-trained technicians to produce accurate results. Tests can be time-consuming and data may not be comparable between clinical sites or measurement protocols [84]. Dual-energy X-ray absorptiometry (DXA) is commonly used in clinical research settings to estimate body composition as it allows precise measurement of regional and total body fat, bone mineral, and lean soft tissue mass [98]. However, the cost, radiation exposure, and relative inconvenience of DXA make it unsuitable for regular clinical visits and unrealistic for home use.

Recently, three-dimensional (3D) laser and optical (3DO) scanners have been investigated as an alternative to manual anthropometry for health assessment [179]. Three-dimensional optical scanners are becoming widely available in clinics, recreational facilities, and even in the home setting. Lengths, girths, and circumferences can be extracted automatically from 3DO scans, allowing direct comparison to the manual measurements traditionally used to quantify human body shape and size. Several studies have investigated the use of 3D body shape to estimate body composition [128], [168], [171], [179]–[181]. However, the simplification of rich 3D body scan data into a few coarse measurements results in the loss of high-fidelity shape features that offer additional information

about tissue composition. Thus, a more advanced approach to 3D body shape modeling may provide superior estimates of body composition.

Statistical shape modeling using Principal Component Analysis (PCA), a technique for dimensionality reduction, can capture complex shape features from 3D scans that may better correlate to actual body composition than traditional approaches. The aim of this study was to first develop body composition prediction models based on 3D body shape PCA and to then compare the predictive accuracy of these models to those developed using the traditional regression modeling approach. A secondary aim was to determine the test-retest precision and 3D PCA and DXA body composition estimates.

5.2.2 Methods

Experimental Design

This analysis is part of Shape Up! Adults, an ongoing stratified cross-sectional observational study supported by the National Institutes of Health (R01 DK109008). Participants underwent two whole-body DXA and 3DO scans, each with repositioning. Statistical shape models were built from 3DO surface scans and compared to previously-published automated anthropometry techniques [180], using DXA as the criterion body composition method. Test-retest precision for body composition variables were determined from the duplicate DXA and 3D optical scans.

Participants

Recruitment for this sample took place between October 2015 and March 2017. Participants were stratified by age (18-40, 40-60, >60 years), ethnicity (non-Hispanic (NH) white, NH black,

Hispanic, and Asian), sex, BMI (<18, 18-25, 25-30, >30 kg/m²), and geographic location (San Francisco, CA or Baton Rouge, LA). Participants were excluded if they could not stand without aid for two minutes, could not lie flat for 10 minutes without movement, had metal objects in their body, or had significant body-shape-altering procedures (liposuction, amputations, etc.). Female participants were also excluded if they were pregnant or breast feeding. All participants were examined at either the University of California, San Francisco (UCSF) Clinical and Translational Science Institute (CTSI) Body Composition, Exercise Physiology, and Energy Metabolism Laboratory or the Pennington Biomedical Research Center (PBRC). The study protocol was approved by the UCSF Committee on Human Research and the PBRC Institutional Review Board. All participants gave written informed consent.

Dual-energy X-ray Absorptiometry

Each participant underwent two whole-body DXA on either a Hologic Horizon/A system at UCSF or a Discovery/A system at PBRC (Hologic Inc., Marlborough, MA, USA). Participants were scanned according to the manufacturer's guidelines. The DXA scans were analyzed at UCSF by an ISCD-certified technologist using Hologic Apex version 5.6 with the National Health and Nutrition Examination Survey (NHANES) Body Composition Analysis (BCA) calibration option disabled. DXA systems were cross-calibrated according to standard Hologic procedures [182]. Body composition measurements from DXA included total body mass, total and regional (trunk, arms, legs) fat mass, bone mineral content, and FFM.

Whole-body surface 3DO scanning

Each participant underwent two 3DO whole-body surface scans on a Fit3D ProScanner v1.0 (Fit3D, Inc., Redwood City, CA, USA). Participants followed a standard positioning protocol and wore skin-tight undergarments to minimize the effects of clothing on observed body shape. The ProScanner v1.0 uses a single light-coding PrimeSense Carmine 1.08 depth sensor that oscillates vertically as participants rotate 360 degrees horizontally on a moving platform. Each scan takes approximately 40 seconds to complete. The Iterative Closest Point (ICP) algorithm was used to spatially align point clouds captured by the sensor as the subject rotates [183]. The final point cloud was converted to a triangle mesh with approximately 300,000 vertices and 900,000 faces representing the human body shape. All 3D scan data were transferred securely from Fit3D to UCSF for statistical analysis.

Statistical Analysis

The goal of this study was to derive prediction equations for body composition from detailed shape measured by 3DO. To achieve this, statistical models of 3D body shape were constructed as follows. A standardized 60,000-vertex body template was warped to fit each participant 3DO scan using the methods of Allen et al. [113]. This registration process ensures vertex correspondence to specific anatomic locations across the dataset, allowing for direct 3D body shape comparison across the whole sample. To initialize registration, seventy-five markers were manually placed on physiological landmarks defined by the Civilian American and European Surface Anthropometry Resource Project (CAESAR) [184]. The landmarks used are described in section 5.2.5. Marker placement was performed by a licensed exercise physiologist using MeshLab version 1.3.2 (Consiglio

Nazionale delle Ricerche, Rome, Italy). The template marker locations were transformed to align with the participant mesh markers, then the remaining template mesh vertices were warped to the participant mesh surface using a minimization process that preserved overall smoothness [113]. After registration, PCA was performed to produce a statistical shape model that captured 95% of shape variation in the 60,000-vertex template space with only a small number of principal components (PCs). Each detailed 3D body scan could be then represented in the 3D PC space as a short vector of weights.

The 3D principal components were used as input variables for stepwise linear regressions to predict DXA-measured total and regional body composition measurements. Regressions were performed subject to minimization of the Schwarz-Bayesian Information Criterion, with five-fold cross validation. PCA and mesh processing were performed using Python version 2.7 (Python Software Foundation, DE, USA). Regression analysis was performed in R version 3.3.3 (R Core Team, Vienna, Austria).

Measurement accuracy was assessed using coefficient of determination (R^2) and root mean square error (RMSE). Measurement precision was quantified using RMSE and coefficient of variation (%CV). To benchmark the performance of body composition estimation equations using the 3D PCs, body composition was also estimated using previously-published equations that use 3DO-derived traditional anthropometrics (e.g. lengths, circumferences, and volumes) [180].

5.2.3 Results

Participants

Two hundred and four healthy adults were recruited at the time of this analysis. Thirty-two participants were excluded for invalid DXA scans (17 missing sub regional results, 7 too large for scan area, 7 high density object in scan area, 1 movement artifact) and 14 participants were excluded for invalid 3DO scans (10 non-form fitting attire, 2 scanner malfunction, 1 positioning error, 1 movement artifact). Thus, complete data were available on 158 healthy adults (67 males and 91 females). Summary demographics of the sample participants can be found in **Table 5-4**.

Table 5-4: Subject Characteristics.

	Male (N=67)			Female (N= 91)		
	Mean (SD)	Min	Max	Mean (SD)	Min	Max
Age [years]	41.1 (15.8)	19	77	45.5 (14.8)	20	74
Height [cm]	176 (6)	163	187	163 (7)	149	181
Mass [kg]	85.3 (18.3)	56.7	148.7	69.3 (14.2)	45.0	118.0
BMI [kg/m ²]	27.5 (5.4)	19.4	49.4	26.1 (5.5)	16.7	46.3
Percent Fat	22.2 (6.1)	10.5	38.8	34.3 (6.2)	21.3	48.3
FMI [kg/m ²]	6.3 (2.7)	2.2	14.7	9.2 (3.5)	4.0	19.3
FFMI [kg/m ²]	21.2 (3.3)	15.2	36.3	16.9 (2.5)	12.2	27.0
Fat Mass [kg]	19.6 (8.7)	6.9	47.5	24.4 (8.7)	11.5	49.5
Fat Free Mass [kg]	65.9 (11.8)	43.7	108.6	45.0 (6.9)	28.8	69.2
Visceral Fat [kg]	0.43 (0.26)	0.19	1.60	0.42 (0.27)	0.09	1.53

BMI = Body Mass Index, FFM = Fat Free Mass, FMI = Fat Mass Index, FFMI = Fat Free Mass Index

Shape Models

PCA on registered 3D scans produced unique statistical shape models for males and females. Twelve components captured 95% of the variance in male body shape while nine components captured 95% of the variance in female body shape. Visualizations of the principal component modes of body shape variation (± 3 standard deviations for each) are shown in **Figure 5-3** and **Figure 5-4** for males and females, respectively. Univariate correlations of principal components to

body composition measurements are presented in **Table 5-5** and **Table 5-6** for males and females, respectively. For men, PC3 significantly correlated ($p < 0.001$) with all 12 body composition measures presented while PC8 and PC12 significantly correlated ($p < 0.05$) with 7 out of the 12 measures. For women, PC3 significantly correlated ($p < 0.001$) with all 12 measures while PC4 significantly correlated ($p < 0.05$) 10 out of the 12 measures.

Table 5-5: Correlation of principal modes to measurements, male.

	PC1	PC3	PC6	PC7	PC8	PC9	PC11	PC12
Percent Fat (%)		0.53**		0.27	-0.43**			
Fat Mass (kg)	0.24	0.75**			-0.30			0.24
FFM (kg)	0.56**	0.71**						0.56**
FMI (kg/m ²)		0.77**			-0.31			
FFMI (kg/m ²)	0.25	0.83**						0.25
Visceral Fat Mass (kg)		0.46**	0.30	0.27	-0.33*			
Trunk Fat Mass (kg)		0.76**	0.26		-0.32*			
Trunk Fat Free Mass (kg)	0.55**	0.74**						0.55**
Arms Fat Mass (kg)		0.73**			-0.27			
Arms Fat Free Mass (kg)	0.47**	0.62**						0.47**
Legs Fat Mass (kg)	0.30	0.63**			-0.21		0.25	0.30
Legs Fat Free Mass (kg)	0.55**	0.62**						0.55**

Only significant correlations are shown, $p < 0.05$. * denotes $p < 0.01$, ** denotes $p < 0.001$. FFM = Fat Free Mass, FMI = Fat Mass Index, FFMI = Fat Free Mass Index, PC = principal component.

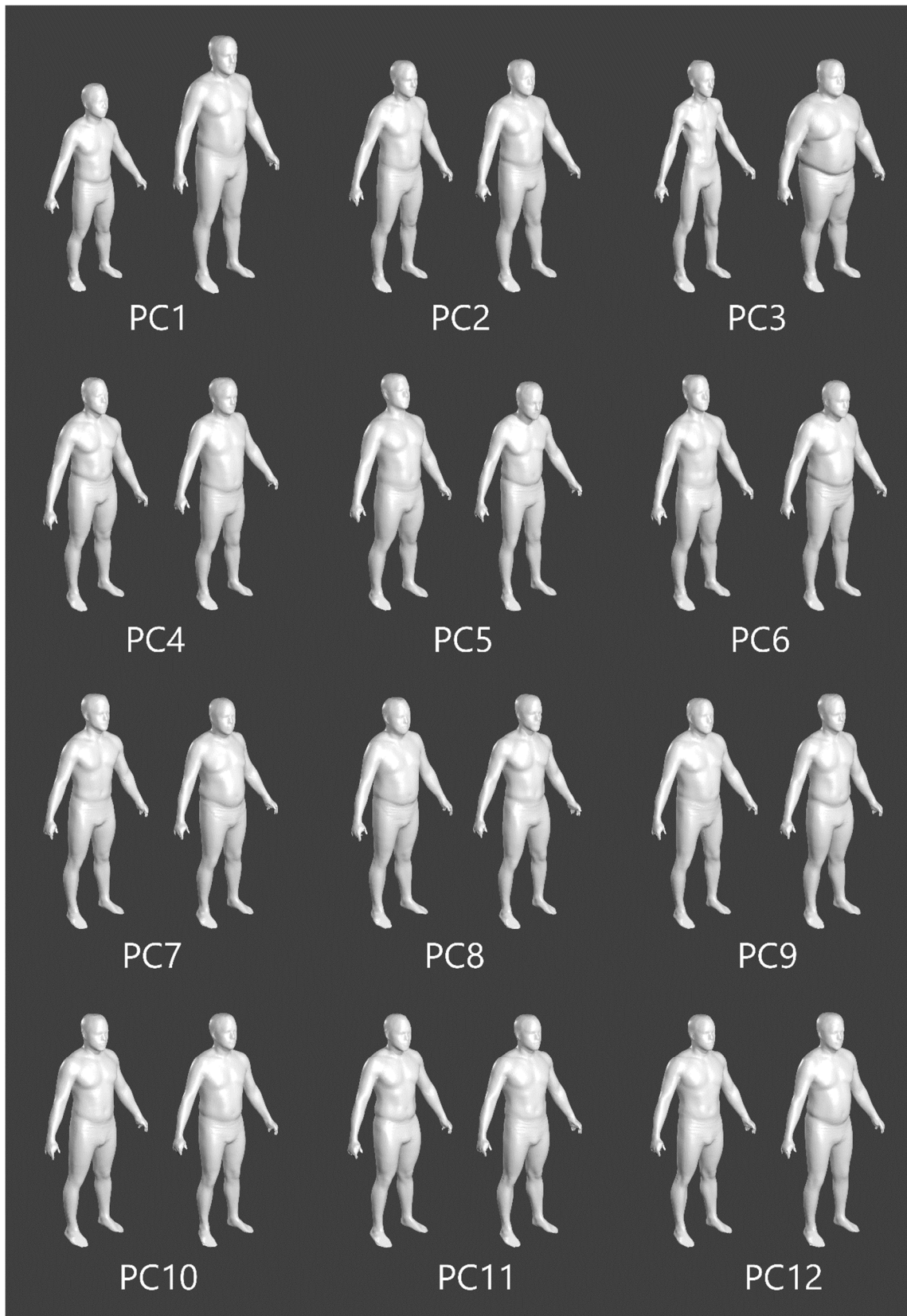


Figure 5-3: The first 12 principal components that captured 95% of shape variance in males. Each component displays -3 SD to the left and +3 SD to the right.

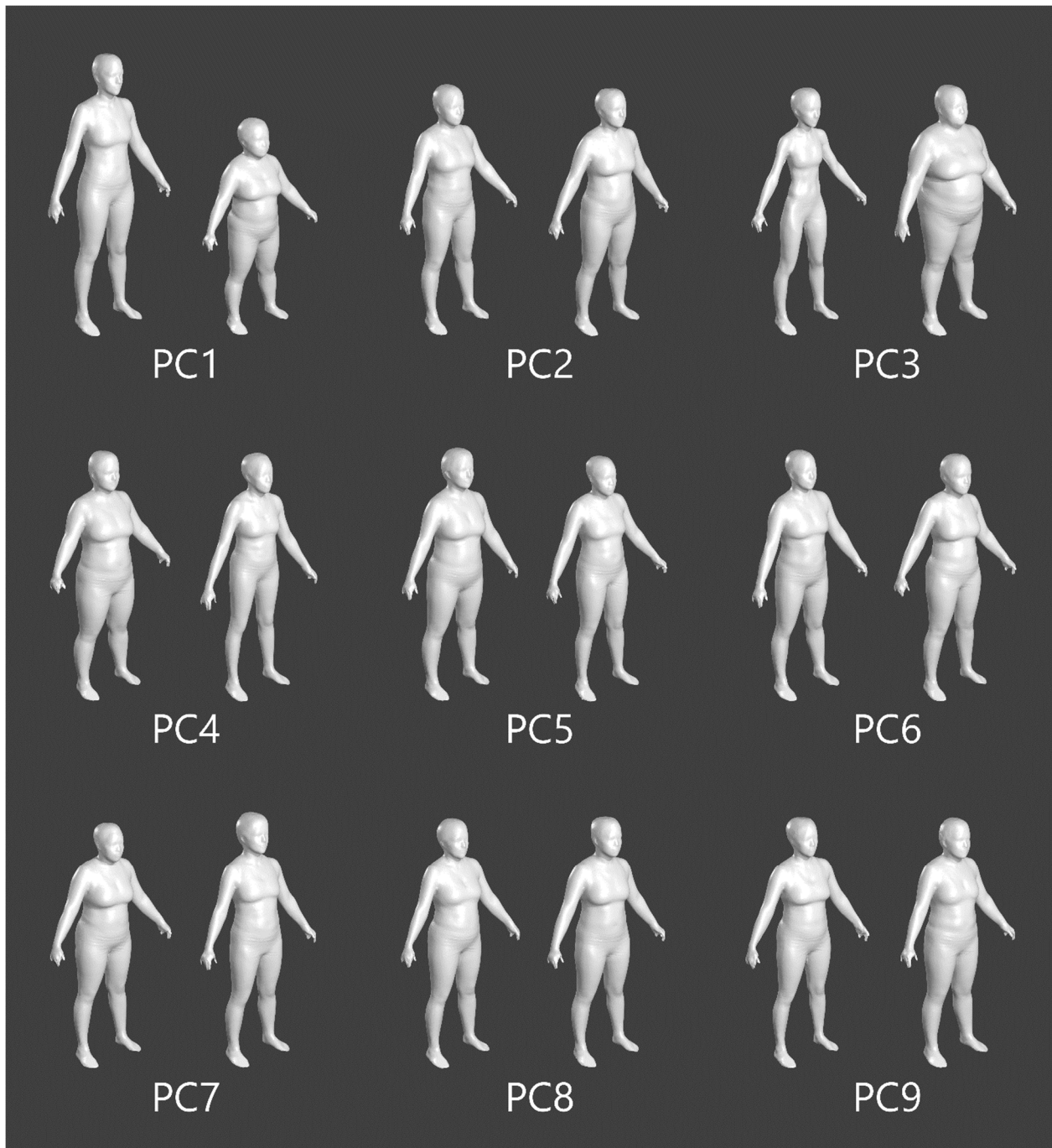


Figure 5-4: The first 9 principal components that captured 95% of shape variance in females. Each component displays -3 SD to the left and +3 SD to the right.

Table 5-6. Correlation of principal modes to measurements, female

	PC1	PC3	PC4	PC5	PC6
Percent Fat (%)	0.23	0.64**	-0.25		
Fat Mass (kg)		0.87**	-0.32*		
Fat Free Mass (kg)	-0.36**	0.72**	-0.26		
FMI (kg/m ²)	0.23	0.84**	-0.31*		
FFMI (kg/m ²)		0.79**	-0.27*		
Visceral Fat Mass (kg)		0.77**	-0.31*		
Trunk Fat Mass (kg)		0.87**	-0.33*		
Trunk Fat Free Mass (kg)	-0.32*	0.72**	-0.33*	-0.27*	
Arms Fat Mass (kg)		0.86**	-0.27		
Arms Fat Free Mass (kg)	-0.26	0.68**			
Legs Fat Mass (kg)		0.71**	-0.28*		0.23
Legs Fat Free Mass (kg)	-0.43**	0.64**			

Only significant correlations are shown, $p \leq 0.05$. Bold denotes correlations significant with the Bonferroni correction, $P \leq 0.00029$. * denotes $p < 0.01$, ** denotes $p < 0.001$. FFM = Fat Free Mass, FMI = Fat Mass Index, FFMI = Fat Free Mass Index, PC = principal component.

Linear models selected from the 3D PCA stepwise regressions are shown in **Table 5-7**. The lists of PCs in each model are provided, along with the sex-combined R^2 and RMSE accuracy metrics to DXA reference values. For total body models, we directly regressed to predict fat mass, then used that equation along with scale weight and measured height to produce predictions of fat free mass, FMI, and FFMI. R^2 and RMSE metrics for the simple anthropometric model [180] are provided as a benchmark. Coefficients of determination for the 3D PCA models ranged from $R^2 = 0.71$ for visceral fat to $R^2 = 0.95$ for total body fat free mass. For the simple anthropometric model, the corresponding values were $R^2 = 0.56$ and 0.91 , respectively. Across all variables tested, the 3D PCA models outperformed (i.e. had greater coefficients of determination and lower RMSEs) than corresponding simple anthropometric models. Generally, fat free mass prediction models had higher

coefficients of determination than corresponding fat mass prediction models, likely since FFM typically represents a larger component of mass within each region than FM.

Repeatability

Test-retest precision was calculated in subsets of 30 males and 30 females for whom complete duplicate DXA and 3DO scan analysis was available. Precision metrics for male and female models are presented in

Table 5-8. RMSE in total body percent fat was 1.11 units for males and 0.92 units for females. Precision was generally better (lower coefficients of variation, %CV) for female 3D PCA models than for male models. FFM measurements had lower coefficients of variation than corresponding fat mass measurements at both total body and regional levels. 3D PCA measurement precision metrics were generally about 3-4x larger than corresponding DXA metrics.

Table 5-7. Predictions of body composition from 3D scans. Linear models were trained using 5-fold cross validation.

	3D PCA and Stepwise Regression				Simple Anthropometric Model	
			R ²	RMSE	R ²	RMSE
Fat Mass (kg)	Male	PC1, 3, 5, 6, 7, 8, 12	0.89	2.80	0.84	4.06
	Female	PC3, 4, 5, 6, 7, 9				
Fat Free Mass (kg)	Male	(scale weight) - (predicted FM)	0.95	3.02	0.91	4.22
	Female					
Percent Fat (%)	Male	((predicted FM) / (scale weight)) * 100	0.80	3.58	0.67	5.14
	Female					
Fat Mass Index (kg/m ²)	Male	(predicted FM) / (height) ²	0.91	0.99	0.86	1.44
	Female					
Fat Free Mass Index (kg/m ²)	Male	(predicted FFM) / (height) ²	0.91	1.04	0.83	1.51
	Female					
Visceral Fat Mass (kg)	Male	PC3, 4, 6, 7, 8, 9	0.71	0.12	0.56	0.19
	Female	PC1, 3, 4, 5				
Trunk Fat Mass (kg)	Male	PC1, 3, 4, 5, 6, 7, 8, 11, 12	0.90	1.43	0.83	2.07
	Female	PC1, 3, 4, 5, 7, 9				
Trunk Fat Free Mass (kg)	Male	PC1, 3, 5, 11	0.94	1.52	0.88	2.17
	Female	PC1, 3, 4, 5, 6				
Arms Fat Mass (kg)	Male	PC1, 3, 5, 7, 8, 12	0.83	0.51	0.46	0.90
	Female	PC1, 3, 4, 5, 6, 7, 8, 9				
Arms Fat Free Mass (kg)	Male	PC1, 3, 4, 5, 10	0.89	0.79	0.55	1.70
	Female	PC1, 3, 6, 8				
Legs Fat Mass (kg)	Male	PC1, 3, 5, 7, 8, 9, 12	0.73	1.50	0.70	1.94
	Female	PC1, 3, 4, 5, 6, 7, 9				
Legs Fat Free Mass (kg)	Male	PC1, 3, 4, 5, 10, 11	0.88	1.60	0.47	3.55
	Female	PC1, 3, 4, 9				

Table 5-8. Test-retest precision of body composition predictions from 3D scans

	3D PCA				DXA			
	Male (n=30)		Female (n=30)		Male (n=29)		Female (n=30)	
	RMSE	%CV	RMSE	%CV	RMSE	%CV	RMSE	%CV
Fat Mass [kg]	1.02	5.0	0.67	2.7	0.30	1.42	0.23	0.86
Fat Free Mass [kg]	1.02	1.5	0.67	1.5	0.28	0.42	0.28	0.63
Percent Fat [%]	1.11	--	0.92	--	0.30	--	0.31	--
Fat Mass Index [kg/m ²]	0.33	5.0	0.26	2.7	0.10	1.42	0.08	0.83
Fat Free Mass Index [kg/m ²]	0.33	1.5	0.26	1.5	0.09	0.43	0.11	0.63
Visceral Fat Mass [kg]	0.05	12.3	0.01	3.2	0.03	6.38	0.03	5.88
Trunk Fat Mass [kg]	0.53	5.5	0.26	2.3	0.25	2.47	0.28	2.37
Trunk Fat Free Mass [kg]	0.34	1.1	0.37	1.6	0.32	1.00	0.20	0.91
Arms Fat Mass [kg]	0.17	6.7	0.12	3.6	0.08	3.12	0.07	2.02
Arms Fat Free Mass [kg]	0.25	2.8	0.12	2.5	0.17	1.85	0.10	2.21
Legs Fat Mass [kg]	0.43	6.1	0.38	4.2	0.17	2.33	0.11	1.12
Legs Fat Free Mass [kg]	0.62	2.8	0.24	1.7	0.23	1.03	0.11	0.80

3D and DXA scans were each performed with repositioning. 30 participants per sex, 2 scans per participant. One male participant had only one DXA scan available and was excluded from this precision analysis. %CV: coefficient of variation. RMSE: root-mean-square error.

5.2.4 Discussion

In this study, we found that shape information extracted from 3D optical scans by PCA provided moderately strong estimates of DXA body composition measurements in healthy adults. We demonstrated the feasibility of an advanced statistical shape modeling technique for relating shape components from whole-body surface 3D scans to body composition without relying on traditional anthropometric measurements. Across whole-body and regional body composition measurements, statistical shape analysis outperformed the previous best method of body composition assessment from 3D scans that utilizes simple anthropometrics. The R^2 of 0.91 for estimating fat mass index from the 3D shape model also compares favorably to both skinfold anthropometry (SFA) and bioelectrical impedance analysis (BIA), as a 2013 study by Hronek et al. comparing DXA to SFA ($R^2 = 0.86$) and DXA to BIA ($R^2 = 0.88$) [185].

Previous studies report that 3D optical scanners offer precise measurements of body shape and composition. Lee, et al. reported accurate prediction of total fat mass (training $R^2 = 0.95$, RMSE = 3.39 kg) using one length and two volumes from a custom-built 3D optical scanner, along with sex [128]. Ng et al. demonstrated accurate prediction of total body composition (fat mass validation $R^2 = 0.76$, RMSE = 3.72 kg; fat free mass validation $R^2 = 0.85$, RMSE = 3.14 kg) using a combination of four length and volume measurements from a commercial 3D optical scanner, along with sex as a covariate [180]. These previous studies have been limited to linear, circumferential, volumetric, and surface area measurements extracted from scans using scanner manufacturers' proprietary, often non-standard, algorithms. This limitation can lead to incompatibility between datasets and fragile statistical models that apply only to specific scanner hardware/software combinations. By contrast, our study used the entire 3D space of human shape data to create PCA-based body shape models. This technique eliminates the need for inconsistent anthropometry measures for prediction of health status. With proper preprocessing and registration, 3D body shape models can be agnostic to scanning technology, allowing comparison across a wide array of 3D body scanning systems. Further studies may use more advanced supervised statistical shape modelling techniques to investigate health predictions that require more localized or fine-grained shape characteristics not captured by PCA, such as those caused by edema or cellulite.

This study had a few limitations. The study population was restricted to healthy adults, in whom body shape is relatively stable over time. Children, by contrast, undergo significant skeletal and overall body shape changes as they grow. The adult shape models derived here may not accurately interpret the unique body shapes and shape dynamics observed in children. Shape

variation of children is an active area of research, and child-specific body shape models are currently under development in the Shape Up! Kids study (NIH R01DK111698). Another limitation of this study was the requirement for manual landmark placement. There are significant research efforts to accurately register point sets without the need for picked landmarks, and robust to variations in pose [186]–[188]. Validation of a robust landmark-free registration method would automate the analysis process and enable broad implementation of these modeling techniques.

In conclusion, PCA of 3DO scans provides compact shape features that describe detailed individual body shape. These 3D PCs can be used to predict body composition with greater accuracy than traditional anthropometric modeling approaches and good repeatability. 3DO body scanning is safe, accessible, and increasingly affordable. Consequently, this technology is uniquely attractive for longitudinal body shape and composition monitoring at the individual level.

5.2.5 Supplement: Descriptions of 75 Body Landmarks for 3D Shape Registration

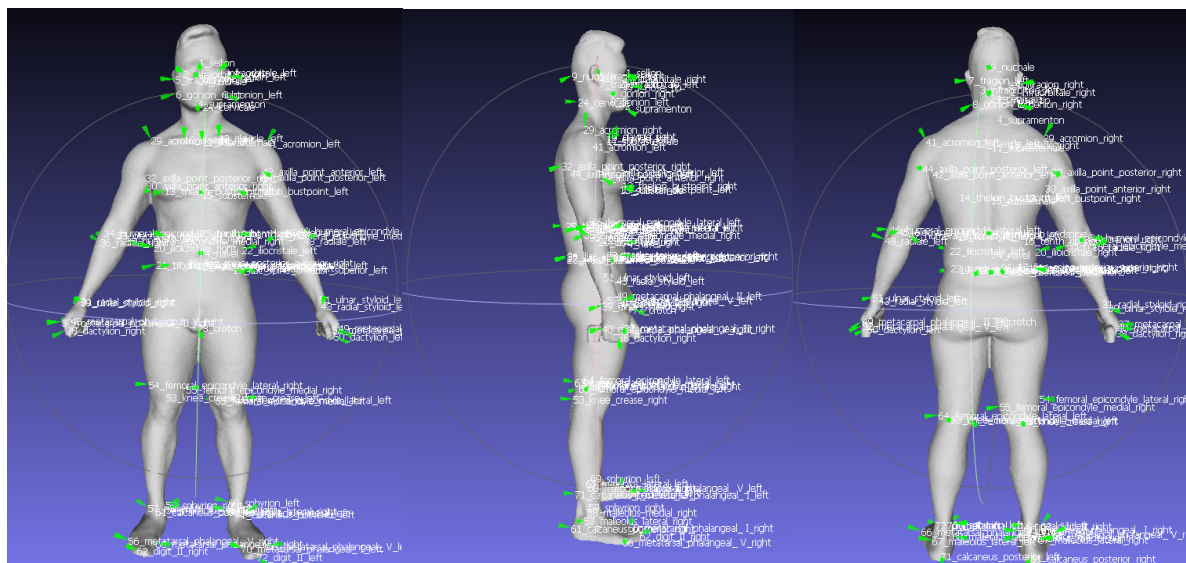


Figure 5-5: Annotated 3D body scan with 75 landmarks shown. Mesh annotation and visualization was performed in MeshLab version 1.3.2.

A set of 75 markers is annotated on each 3D body scan, based on the protocol defined for the CAESAR study [184]. The list of markers is reproduced in Table 5-9 and visualized in Figure 5-5. These points are used to initialize registration of a standardized 3D body mesh template to fit each target participant 3D body scan.

Table 5-9: List of markers for 3D body scans. Adapted from [184].

1_sellion	26_iliac_spine_posterior_superior_right	51_ulnar_styloid_left
2_infraorbitale_right	27_iliac_spine_posterior_superior_left	52_metacarpal_phalangeal_V_left
3_infraorbitale_left	28_waist_preferred_posterior	53_knee_crease_right
4_supramenton	29_acromion_right	54_femoral_epicondyle_lateral_right
5_tragion_right	30_axilla_point_anterior_right	55_femoral_epicondyle_medial_right
6_gonion_right	31_radial_styloid_right	56_metatarsal_phalangeal_V_right
7_tragion_left	32_axilla_point_posterior_right	57_malleolus_lateral_right
8_gonion_left	33_olecranon_right	58_malleolus_medial_right
9_nuchale	34_humeral_epicondyle_lateral_right	59_sphyrion_right
10_clavicle_right	35_humeral_epicondyle_medial_right	60_metatarsal_phalangeal_I_right
11_suprasternale	36_radiale_right	61_calcaneus_posterior_right
12_clavicle_left	37_metacarpal_phalangeal_II_right	62_digit_II_right
13_thelion_bustpoint_right	38_dactylion_right	63_knee_crease_left
14_thelion_bustpoint_left	39_ulnar_styloid_right	64_femoral_epicondyle_lateral_left
15_substernale	40_metacarpal_phalangeal_V_right	65_femoral_epicondyle_medial_left
16_tenth_rib_right	41_acromion_left	66_metatarsal_phalangeal_V_left
17_iliac_spine_anterior_superior_right	42_axilla_point_anterior_left	67_malleolus_lateral_left
18_tenth_rib_left	43_radial_styloid_left	68_malleolus_lateral_right
19_iliac_spine_anterior_superior_left	44_axilla_point_posterior_left	69_sphyrion_left
20_ilioicristale_right	45_olecranon_left	70_metatarsal_phalangeal_I_left
21_trochanterion_right	46_humeral_epicondyle_lateral_left	71_calcaneus_posterior_left
22_ilioicristale_left	47_humeral_epicondyle_medial_left	72_digit_II_left
23_trochanterion_left	48_radiale_left	73_crotch
24_cervicale	49_metacarpal_phalangeal_II_left	74_navel
25_tenth_rib_midspine	50_dactylion_left	75_nose_tip

5.3: Manifold Regression to Predict Compositional Shape Change

Over half of all participants discontinue diet and exercise programs within one year. Value placed on personal aesthetics is a powerful predictor of compliance to weight-loss regimes [189].

Thus, providing a realistic target for body shape may improve treatment compliance. Whereas simple body shape models may attempt to vary body circumferences uniformly, or shrink the body along one dimension, we used the Shape Up! 3D optical and DXA information to create data-driven models for predicting realistic body shape changes in response to specific gains and losses in fat and lean mass.

In order to generate shape changes for specific body composition adjustments (i.e. decrease in fat mass with fixed lean mass), we performed multivariate manifold regression over the set of principal component representations of body shape. As described by Allen [190], this is performed by preparing an attribute matrix A and a PCA weight matrix W . Each vector a_i in A contains the measured variables of interest (here: fat mass, lean mass, height, and age) for participant i . Each vector w_i in W contains the specific PC weights that define participant i 's body shape in the PCA body shape model. We then calculate the relationship M between attributes and body shape as:

$$M = WA^+$$

where A^+ is the pseudoinverse of A . For a given vector of attributes a , we can then calculate a probable body shape using the weights $w = Ma$. We can also calculate differential changes in body shape for differential changes in attributes as $\Delta w = M\Delta a$. These Δw vector can be added to a participant shape vector w to visualize body shape changes for that specific person.

For this analysis, variables included in the manifold regression were fat mass, fat free mass, age and height. Age and height were held fixed while fat mass and fat free mass were adjusted independently. Regression was performed in Python 2.7 (Python Software Foundation, DE, USA)

and scikit-learn version 0.19.0 [191]. Synthesized body meshes were created and visualized in 3D using Blender version 2.78 (Blender Foundation, Amsterdam, Netherlands).

We performed separate regressions for the male and female datasets. Example male and female participants at their current shape and fat and lean mass increases and decreases of up to ± 20 kg (male) and ± 10 kg (female) are shown in Figure 5-6. These predicted bodies represent a BMI range of 16 to 40 kg/m^2 .

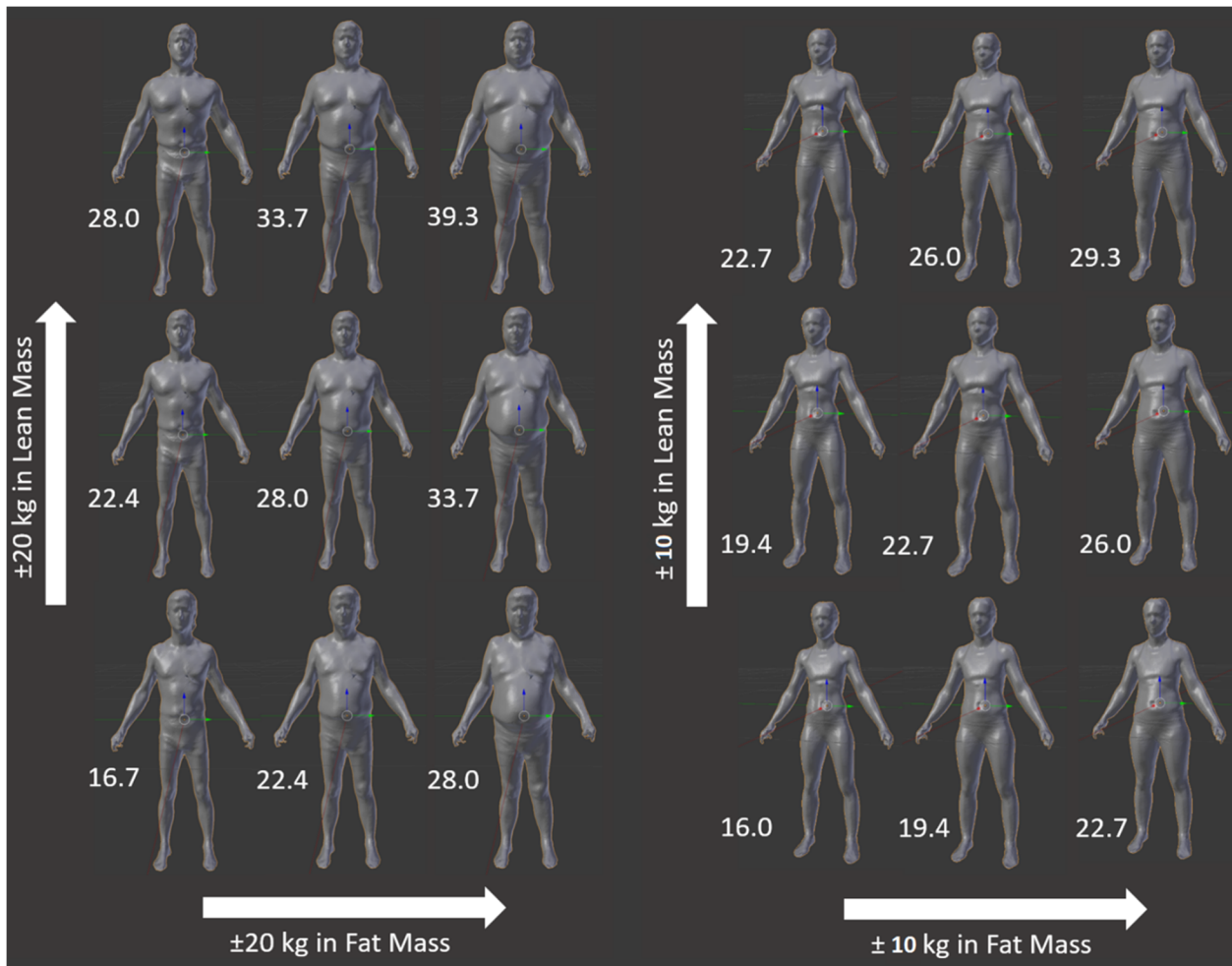


Figure 5-6: Predicted 3D body shape changes for individual male (left) and female (right) participants. Actual participant scans are shown in the middle of each set. Height and age were held constant while fat mass and lean mass, were varied independently using manifold regression. Numbers next to each body represent BMI.

6 | Novel Multi-Modality Clinical Assessment Techniques

6.1: Validation of DXA + BIA for Clinical 4C Body Composition Assessment

6.1.1 Introduction

Over 1.9 billion adults worldwide are overweight, and of those some 650 million are obese. Obesity now affects about 13% of the world's population – a figure that has nearly tripled since 1975 [192]. Low- and middle-income countries that have historically faced challenges of undernutrition now increasingly face a double burden of malnutrition marked by simultaneous prevalence of obesity and undernutrition [193], [194]. These conditions are associated variety of metabolic diseases and stunted growth in children. Malnutrition leads to altered states of body composition. Accurate measurement of body composition is important for the diagnosis of nutritional and metabolic disorders and monitoring of associated treatments [53].

Four component (4C) models of body composition – those that divide the body into fat, water, protein, and mineral masses – are considered the reference within the research community. Importantly, 4C models do not assume a fixed hydration as is the case in simpler body composition models [195]. This is important for assessment of undernutrition in children, which is often associated with dehydration [196], as well as assessment of lean mass in older adults, which has been shown to have significantly different hydration than found in younger adults [197]. Altered lean mass hydration in older adults may explain why DXA-measured lean mass (which assumes fixed hydration) is a poor predictor of mortality and functional strength compared to simple handgrip strength [29]. Direct measurement of lean mass water and protein content is therefore particularly

useful in the presence of wasting conditions associated with aging such as sarcopenia and cachexia [198].

Despite its advantages, 4C body composition is seldom used in the clinic because it requires several different measurements that are time consuming and costly. The Lohman 4C model, for example, includes bone mineral measurements from DXA, body mass from a scale, total body volume, and total body water from labeled water dilution [199]. Wilson proposed a simplified model for clinically-viable 4C body composition that uses DXA-calculated body volume in place of ADP and BIA-calculated total body water in place of labeled water dilution [200]. We sought to validate this rapid, simplified 4C method against the reference Lohman method as well as to 2-component (BIA, ADP, and TBW) and 3-component models (DXA) of percent fat.

6.1.2 Methods

A cross-sectional convenience sample of healthy adults underwent whole-body DXA, multifrequency BIA, air displacement plethysmography (ADP), height and weight, and total body water deuterium dilution measurements. Four-component body composition was calculated using the Lohman method [201] and the simplified DXA+BIA approach of Wilson [200]. Linear regression analysis was performed to determine agreement between body composition methods. We describe the details of each part of the study below.

Participants

Thirty-one healthy adults over the age of eighteen were enrolled in a prospective open recruitment during the time period of November 2016 and April 2017. Each participant received

duplicate measures with repositioning for whole-body DXA and segmented multifrequency BIA scans, and singleton measures of deuterium dilution and air-displacement plethysmography (due to time considerations for these techniques). Exclusion criteria included a history of body-altering surgery, significant non-removable metallic implants, height over 73 inches (185 cm) and weight over 250 pounds (113 kg) (to ensure whole-body fit within the dimensions of the DXA scan table). Recruitment was performed using flyers posted around the UCSF Parnassus campus. All participants provided informed consent. The study protocol was approved by the UCSF Committee on Human Research (IRB #16-19342).

Dual Energy X-Ray Absorptiometry

Whole-body DXA scans were acquired on a Hologic Discovery/W system (Hologic Inc., Marlborough, MA, USA). All scans were analyzed at Hologic, Inc. by a single International Society for Clinical Densitometry (ISCD) certified technologist using Hologic APEX software (version 4.6.0.4) with NHANES body composition correction disabled. Participants were clothed in form-fitting undergarments, without shoes, and positioned on the scanner table with arms out to the side, hands flat on table and feet in planarflex position, in accordance with the manufacturer's standard protocols. The scanner was kept in regular calibration using daily and weekly quality control protocols scanning spine and soft tissue phantoms according to ISCD guidelines.

Bioelectrical Impedance Analysis

Whole-body segmented multifrequency BIA measurements were acquired on an InBody S10 system (InBody Inc., Cerritos, CA, USA). Measurements were performed with the participant in supine position immediately after DXA scans. Contact sites on the fingers and ankles were cleaned

prior to measurement with a sterile antimicrobial tissue provided by the manufacturer. Touch type electrodes were used in accordance with standard protocols. Participants were scanned a total of three times to allow for assessment of measurement precision with and without repositioning. TBW and %Fat measurements were recorded directly from the device. The average of two TBW measurements (with repositioning) was used for 4C analysis.

Air Displacement Plethysmography

Whole-body volume measurements were taken using air displacement plethysmography (ADP) in a BodPod (v5.4.1, COSMED USA, Inc., Concord, CA). Measurements were taken using the manufacturer's standard protocol. Participants were clothed in form-fitting clothing and a swim cap. Lung volume was measured directly using the built-in breathing tube system. The BodPod was regularly calibrated using a known-volume cylinder and known-mass weights in accordance with manufacturer guidelines. The BodPod provided body volume measurements for the 4C models as well as its own estimate of %Fat.

Deuterium Dilution

Total Body Water was assessed using a four-hour deuterium (D_2O) dilution protocol as defined in the International Atomic Energy Agency standards by Schoeller, et al. [92]. In summary, participants were provided with a measured dose of deuterium in local drinking water (100 mL total volume) to achieve 0.05 grams of excess 2H per kilogram of body weight. Three 2.5 mL saliva samples were collected – one at baseline (before dose consumption), one 3 hours post dosing, and one 4 hours post dosing. Participants were allowed to void and/or drink small amounts (< 500 mL) of water during the four-hour protocol; all fluid changes were measured and recorded as change in

body weight using a high precision scale. Total body water was calculated by measuring deuterium enrichment in the saliva samples versus baseline dose and drinking water samples [92] which included the correction factor of 1.041 for non-aqueous exchange of deuterium. Fat mass was estimated from TBW using a fixed hydration constant of 0.732 for lean mass: $FatMass = TotMass - TBW/0.732$. All samples were analyzed at the University of Wisconsin Biotechnology Center.

4-Component Models

Four component models divide the body into fat, water, protein, and mineral masses. We calculated 4C composition using the model of Lohman, et al. [53], [199], [202], reproduced below.

$$FatMass_{4CLohman} = 2.747TotVolume - 0.714TBW + 1.146TotMineral - 2.0503TotMass$$

$$TotMineral = BoneMineral + SoftTissueMineral$$

$$TotMineral = BMC + 0.0105TotMass$$

$$ProteinMass_{4CLohman} = TotMass - (FatMass_{4CLohman} + TBW + BMC)$$

ADP, D₂O dilution, DXA, and scale weight measurements were used for TotVolume, TBW, BMC, and TotMass, respectively. The Lohman model served as criterion method for fat and protein measurements. It may be noted that this model is often misrepresented to include only bone mineral mass instead of total mineral mass, which includes mineral in both bone and soft tissues. Bartok-Olson described the discrepancy and its implications here [202]. Note also that the residual mass ($ProteinMass_{4CLohman}$) contains a small amount of carbohydrate in addition to protein.

The simplified DXA+BIA 4C model described by Wilson [200] uses the same form as the Lohman 4C model, but body volume calculated from DXA instead of ADP, and water mass measured by BIA instead of D₂O. Specifically, Wilson showed that body volume could be accurately calculated using calibrated fat, lean, and bone densities along with the measured masses from whole-body DXA scans [152].

$$TotVolume_{DXA} = v_{lean}LeanMass_{DXA} + v_{fat}FatMass_{DXA} + v_{BMC}BMC_{DXA} + v_{residual}$$

where inverse density coefficients v are calibrated for each make of DXA scanner. These coefficients were published in earlier cross-sectional studies with matched DXA and ADP measurements using multiple linear regression with the three-component DXA masses as input and ADP volume as output. Wilson derived separate volume coefficients for Hologic [152] and GE DXA systems [200], and reported test-retest precision of RMS-%CV = 1.1 in total body DXA-volume. In the present study, Hologic calibration values were used ($v_{lean} = 0.95$, $v_{fat} = 1.14$, $v_{BMC} = 0.21$, $v_{residual} = 0.01$). We sought to validate Wilson's DXA+BIA 4C model and demonstrate hardware independence by using an independent recruitment and different devices (Hologic DXA and InBody BIA, versus GE DXA and Impedimed BIA).

Statistical Analysis

Linear regressions were performed to assess agreement between different modalities. Total body water from BIA was compared against deuterium dilution criterion measurement. Percent body fat was compared between DXA, ADP, BIA, D₂O, and the proposed 4C DXA+BIA model against the 4C Lohman criterion method. Constant intercepts were included in linear models only if

significant at $P < 0.05$. Test-retest precision was quantified using root mean square coefficient of variation (%CV) for mass and volume measurements, and root mean square standard deviation (RMS-SD) for percent fat measurements as described elsewhere [203]. Outlier detection thresholds for test-retest measurements were conservatively defined at six standard deviations σ away from zero, where σ was estimated by the sample median absolute difference (MAD) between repeat measurements [204]. Statistical analyses were performed using pandas 0.20.1 (Python Software Foundation, Wilmington, DE), SAS version 9.4 (SAS Institute, Cary, NC), and MATLAB R2017a (The MathWorks Inc., Natick, MA).

6.1.3 Results

Table 6-1: Summary demographic statistics of the 23 participants included in the present analysis (11 male). Total BMC, TBW, and Body Volume measures are reported from DXA, deuterium dilution, and air displacement plethysmography, respectively.

Variable	Mean (SD)	Min	Max
Age [years]	33.8 (12.3)	22	63
Height [cm]	168.4 (11.0)	148.7	188.6
Mass [kg]	73.2 (12.6)	54.1	104.1
Body Mass Index [kg/m ²]	25.6 (4.1)	20.2	36.9
Total Bone Mineral Content (DXA) [kg]	2.40 (0.43)	1.57	3.29
Intracellular Water (BIA) [kg]	25.1 (5.7)	15.5	39.0
Extracellular Water (BIA) [kg]	14.9 (3.1)	9.7	22.5
Total Body Volume [L]			
ADP	70.4 (12.0)	56.9	104.9
DXA	70.9 (12.1)	57.4	104.7
Total Body Water [kg]			
D ₂ O	38.4 (7.9)	26.1	53.9
BIA	40.0 (8.8)	25.1	61.5
Percent Fat			
DXA	26.9 (10.7)	9.9	45.1
ADP	26.0 (11.2)	13.0	50.0
BIA	25.1 (11.8)	8.9	52.3
D ₂ O	27.9 (10.0)	11.2	47.0

Of the 31 participants that completed the study protocol, 23 had complete valid measurements. There was an error in the dose preparation for the first batch of 8 participants that invalidated measurements; these participants' data were used for precision analysis only. Summary demographics of the participants included in the analysis are shown in Table 6-1.

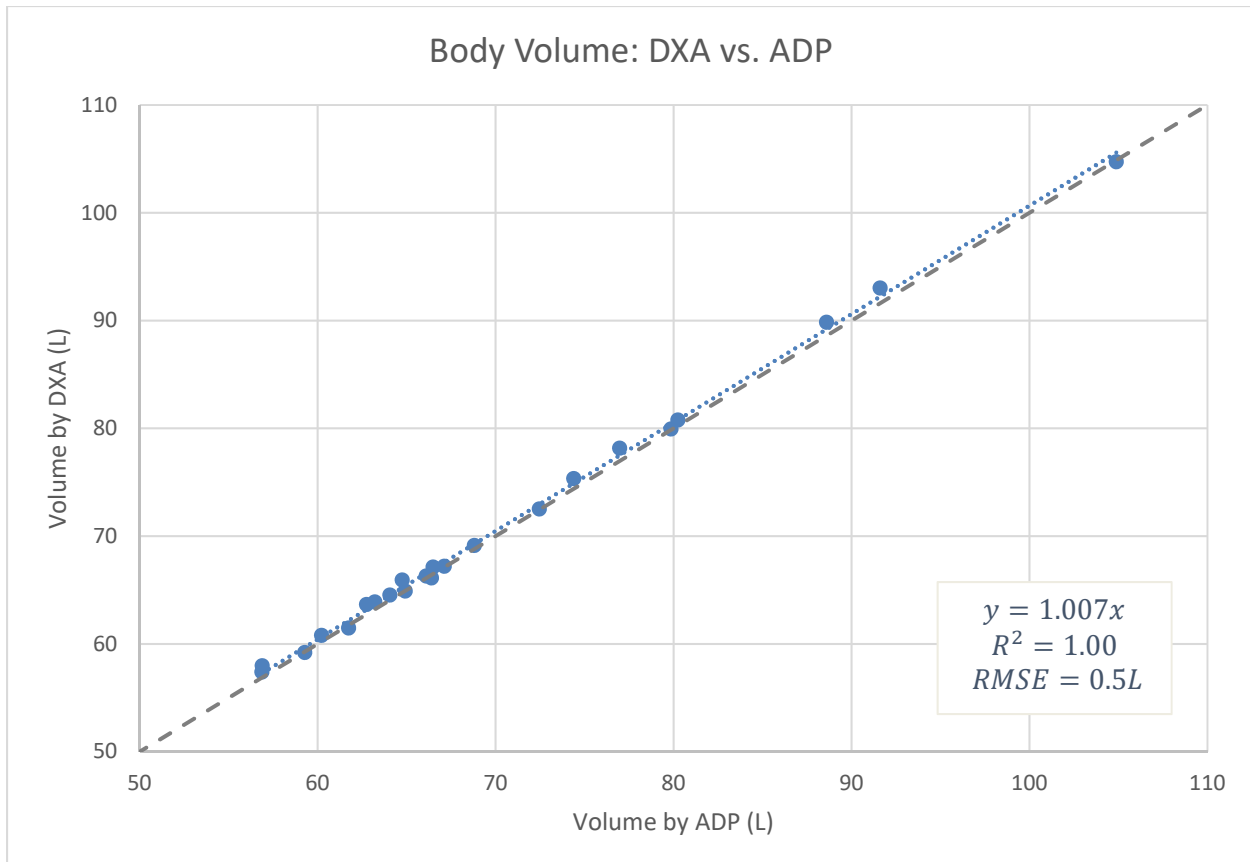


Figure 6-1: Linear regression between body volume measurements from DXA and ADP (n=23). High correlation was observed, though a slope significantly different from 1 was detected. These data were used to determine a linear correction equation for body volume from DXA: $BV_{ADP} = 0.993 BV_{DXA}$ (95% CI: [0.990, 0.996]). The dashed line is the line of identity.

Body volume measurements calculated from DXA showed excellent agreement with ADP (Figure 6-1), $BV_{ADP} = 0.993 BV_{DXA}$ (95% CI: [0.990, 0.996]). Total body water measurements from

BIA also showed strong agreement to criterion measurements from D₂O (Figure 6-2), $TBW_{D_2O} = 0.956 TBW_{BIA}$ (95% CI: [0.932, 0.979]).

Whole-body percent fat was calculated using the 4C Lohman model as presented above after correcting for the small biases in the DXA volume and BIA water measures using the equations in Figure 6-1 and Figure 6-2. Regression results for the 2-, 3-, and 4-component methods are shown in Figure 6-3. Each of DXA, BIA, ADP, and D₂O estimates of percent fat showed strong agreement with the Lohman model, with $R^2 \geq 0.90$. D₂O dilution was the only modality to exhibit a significant bias. BIA exhibited the highest RMSE at 3.83 percentage units, while ADP had the lowest at 1.71; however, this is likely due to the fact that 4C Lohman %Fat equation is dominated by body volume (here measured by ADP). Note that the Hologic DXA percent fat results were calculated with NHANES correction [132] disabled. Enabling the NHANES correction resulted in overestimated DXA fat values compared to the 4C Lohman model (see 6.1.5 Supplement).

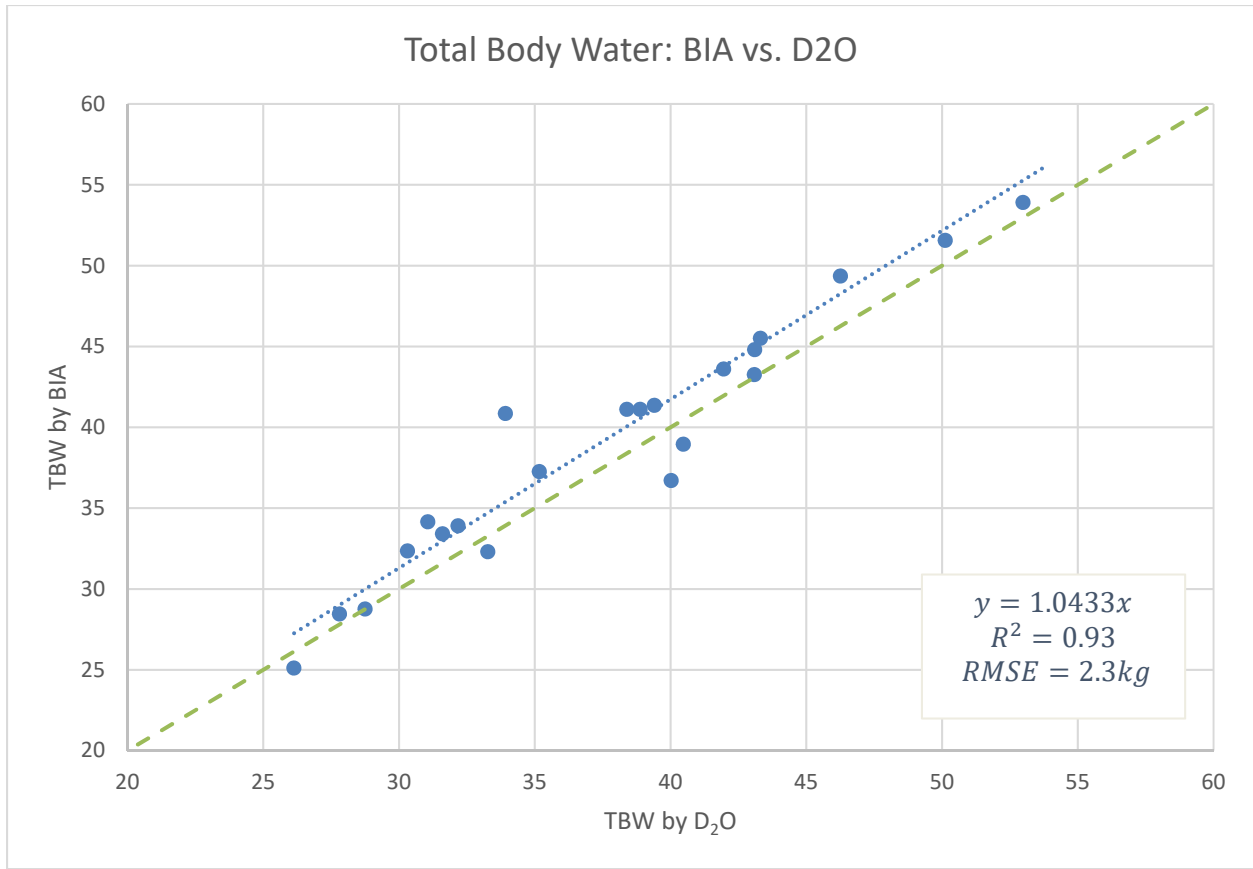


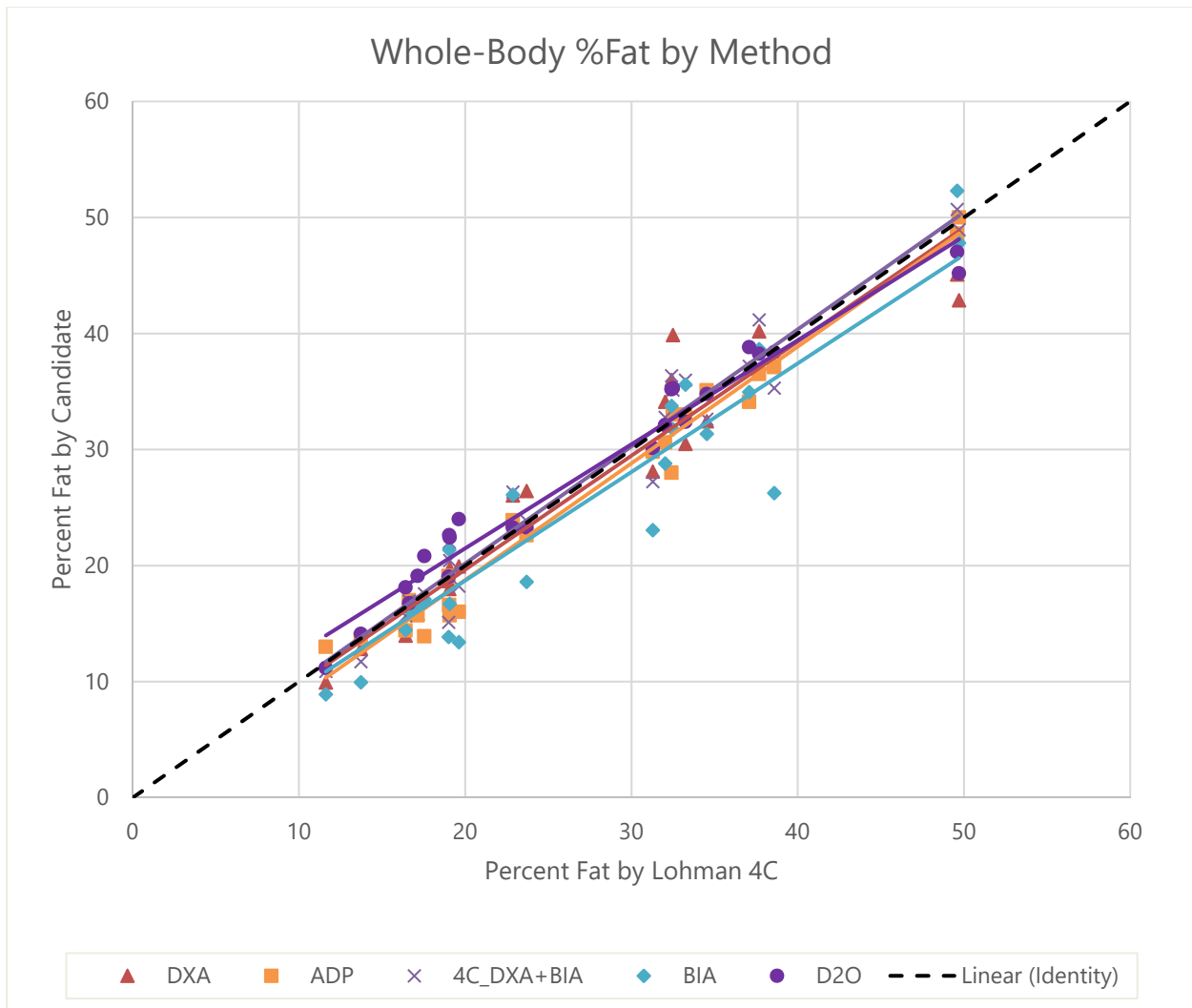
Figure 6-2: Linear regression between total body water measurements from BIA and D2O (n=23). High correlation was observed, though a slope significantly different from 1 was detected. These data were used to determine a linear correction equation for total body water from BIA: $TBW_{D2O} = 0.956 TBW_{BIA}$ (95% CI: [0.932, 0.979]). The dashed line is the line of identity.

The simplified 4C DXA+BIA model closely agreed with the Lohman 4C reference. The 4C DXA+BIA model can be generalized using the equation below.

$$\begin{aligned}
 FatMass_{4C} = & 2.747 * DXA_{corr} (v_{lean}LeanMass_{DXA} + v_{fat}FatMass_{DXA} + v_{BMC}BMC_{DXA}) \\
 & - 0.714 * BIA_{corr}(TBW_{BIA}) + 1.146(BMC_{DXA} + 0.0105TotMass) \\
 & - 2.0503TotMass
 \end{aligned}$$

where $v_{lean} = 0.95$, $v_{fat} = 1.14$, $v_{BMC} = 0.21$, and $DXA_{corr} = 0.993$ for the present Hologic DXA system, and $BIA_{corr} = 0.956$ for the present InBody BIA system.

Residual protein measurements from the 4C DXA+BIA model versus the Lohman model are shown in Figure 6-4. Whole-body 4C protein measured by DXA+BIA closely approximates the Lohman reference method.



Method	Slope [95% CI]	Intercept [95% CI]	R ²	RMSE
DXA	0.98 [0.94, 1.03]	n.s.	0.93	2.97
ADP	0.96 [0.94, 0.99]	n.s.	0.98	1.71
BIA	0.94 [0.88, 0.99]	n.s.	0.90	3.83
D₂O	0.90 [0.82, 0.97]	3.56 [1.45, 5.68]	0.97	1.80
4C DXA + BIA	1.01 [0.97, 1.04]	n.s.	0.96	2.33

Figure 6-3: Linear regression between whole-body percent fat from the 2-, 3-, and 4-component body composition assessment methods in this study versus the reference 4C Lohman model (n=23). "n.s." indicates that the regression intercept was non-significant (P > 0.05) and set to zero.

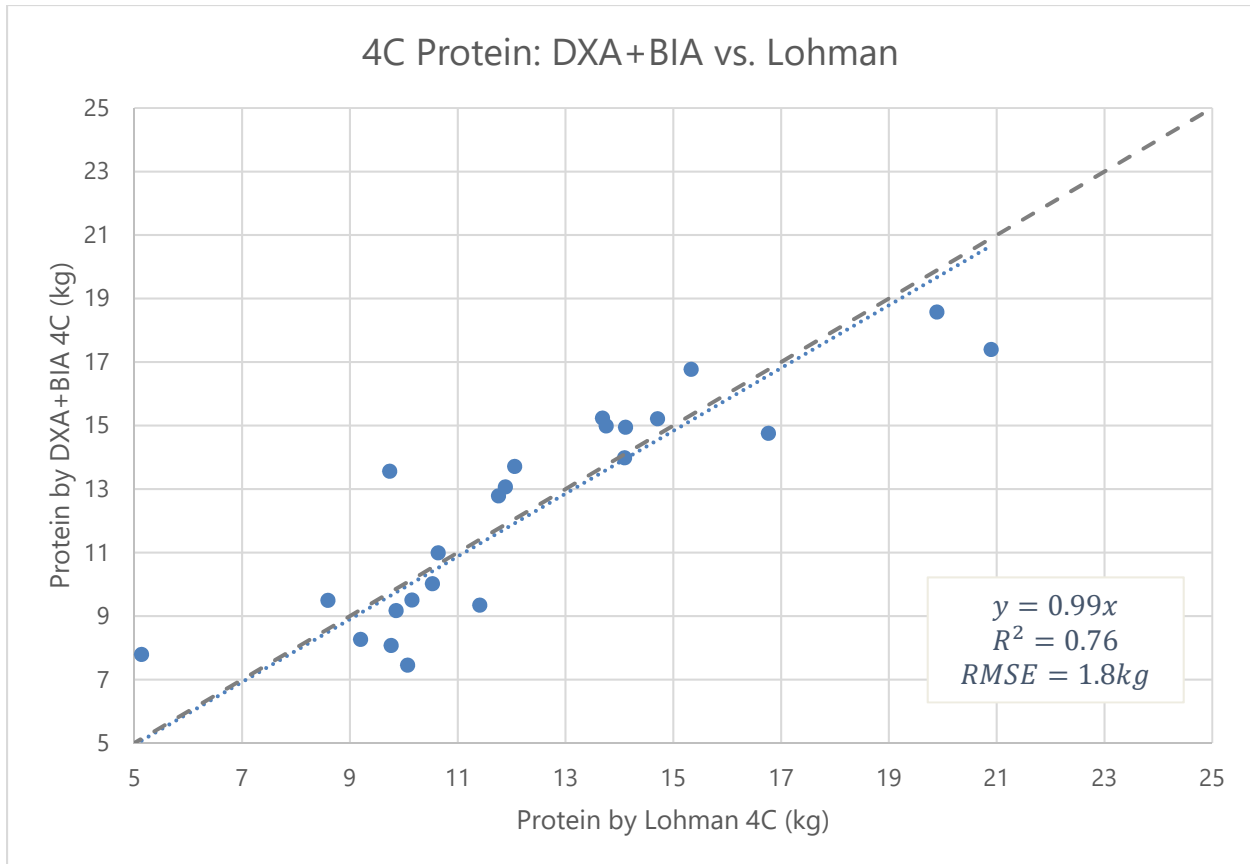


Figure 6-4: Linear regression of whole-body 4C residual protein measured by DXA+BIA method versus Lohman reference method (n=23). The equation for the line of best fit is $Prot_{DXA+BIA\ 4C} = 0.99 Prot_{Lohman\ 4C}$ (95% CI: [0.93, 1.05]). The dashed line is the line of identity.

Duplicate DXA and BIA measurements were available for all 31 participants. Test-retest precision results for BIA total body water and fat mass, DXA fat mass and volume, and 4C DXA+BIA fat mass and protein mass are shown in Table 6-2. Repeat TBW_{BIA} measurements (with immediate repositioning) showed a coefficient of variation of $\%CV = 5.2$. The median absolute difference (MAD) in the test-retest data was 0.3 kg. Outliers were defined conservatively as the test-retest difference exceeding six times the MAD, or 1.8 kg. Four outlier pairs were identified in the set of 31 test-retest measurements. Excluding these outliers results in $\%CV = 1.1$. As shown in Table 6-2, precision in TBW_{BIA} significantly affects the precision of 4C DXA+BIA fat and protein measurements. Observed test-retest RMS-SD for BIA, DXA, and 4C DXA+BIA percent fat (after

BIA TBW outlier removal) were 0.9, 0.6, and 0.8 percentage units, respectively. Least significant changes implied by these intra-method errors (approximately 2.77 times the test-retest precision, per [205]) are smaller than the corresponding inter-method errors versus Lohman 4C percent fat of 3.83, 2.97, and 2.33 percentage units, respectively (Figure 6-3).

Table 6-2: Test-retest precision for the BIA and DXA measurements utilized in the study. Duplicate measurements were collected using each modality, with repositioning. High variability in BIA Total Body Water measurements leads to imprecision in BIA fat mass and 4C DXA+BIA fat and protein masses. Removal of outlier BIA TBW measurements as described in the text results in significantly improved precision for each of those measurements.

Variable	Before BIA Outlier Removal (n=31)	After BIA Outlier Removal (n=27)
BIA Total Body Water (%CV)	5.2	1.1
DXA Total Body Volume (%CV)	0.2	0.3
BIA Percent Fat (RMS-SD)	3.8	0.9
DXA Percent Fat (RMS-SD)	0.6	0.6
4C DXA+BIA Percent Fat (RMS-SD)	1.9	0.8
4C DXA+BIA Protein Mass (%CV)	6.1	4.4

Lean mass hydration was calculated as $TBW / LeanMass_{DXA}$ where TBW was measured using either D₂O or BIA. Histograms of participants' lean mass hydration levels are shown in Figure 6-5. Greater mean lean mass hydration was observed when using TBW_{BIA} (mean = 0.755) than TBW_{D2O} (mean = 0.726). Greater spread in lean mass hydration levels was observed in TBW_{BIA} (SD = 0.047) than TBW_{D2O} (SD = 0.027). Hydration results generally agree well with a review of cadaver studies by Wang, et al. [195] in which the hydration mean and standard deviation was found to be 0.737 ± 0.036 . The range of D₂O hydration values is relatively narrow, with only a single data point more than one standard deviation away from the 0.737 mean reported by Wang. However, the range of BIA hydration values was much larger, with five data points more than one standard deviation away from 0.737.

Histogram of Lean Mass Hydration (TBW/DXA Fat Free Mass)

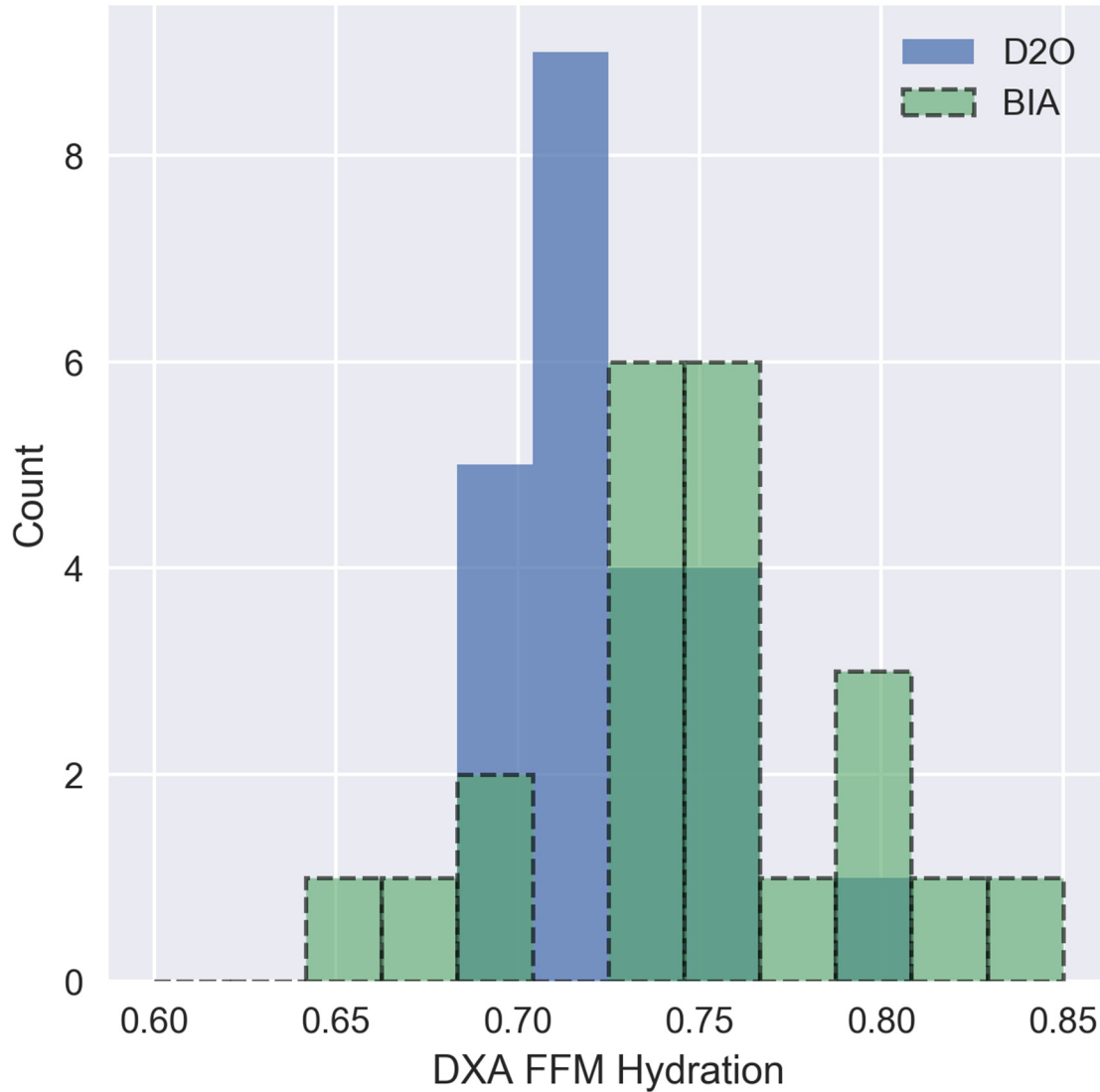


Figure 6-5: Histograms of fat-free mass hydration (defined as total body water divided by fat-free mass from DXA) (n=23). More variance was observed when using BIA for TBW than when using D2O for TBW. The observed range of hydration values extends beyond physiological bounds for healthy adults in the sample; definition of thresholds on plausible hydration levels may provide criteria to validate BIA TBW measurements.

6.1.4 Discussion

Four-component body composition is a well-established method for assessment of metabolic status and health. In this study we found that percent fat measurements from several different technologies using both 2-component (ADP, BIA, and D₂O) and 3-component (DXA) models

agreed well with the criterion 4C Lohman model. Each of these devices should provide accurate, reliable measurements of adiposity in the clinical setting when normal hydration is expected. The best agreement with the Lohman model for both %Fat and protein measures was found to be with the rapid 4C DXA+BIA method.

The agreement between the two 4C methods relies on the agreement of BV_{DXA} with BV_{ADP} , and TBW_{BIA} with TBW_{D2O} . Although we found high agreement between the two BV measurements, a small but significant difference was observed ($TBW_{D2O}/TBW_{BIA} = 0.993$). BV is highly weighted in the Lohman 4C model, so it is important that BV measures are accurately calibrated. The two methods have very different underlying assumptions and it is unclear which method most accurately measures volume in an individual. The BodPod is calibrated using a reference object periodically so that accuracy on solid volumes is assured. However, *in vivo* error sources include uncertainty in the lung and gastric volumes. DXA systems only measure solid volume and are unaffected by lung and gastric voids. Potential errors in the DXA volume include the extrapolation of the lean and soft tissue masses over regions containing bone and the lack of existing quality assurance methods to validate soft tissue mass accuracy (standard phantoms and protocols exist only for calibration of bone mineral mass). Clearly, a quality control method for DXA that assures mass accuracies to better than 0.5% is warranted to ensure agreement between DXA systems in the field.

In a similar but larger study, Smith-Ryan, et al. [206] re-derived coefficients for BV_{DXA} calibrated to BV_{ADP} using the same make and model DXA system. Smith-Ryan also did not use the NHANES correction, and found coefficients ($v_{lean} = 0.971$, $v_{fat} = 1.19$, $v_{bone} = 0.086$) similar to those originally published by Wilson: ($v_{lean} = 0.95$, $v_{fat} = 1.14$, $v_{BMC} = 0.21$). In this

study, we found that BV_{DXA} derived using Wilson's coefficients agreed with BV_{ADP} within 0.3%. The difference seen by Smith-Ryan were likely due to slight calibration differences in the DXA systems and could have been corrected using a reference quality control phantom for soft tissue masses.

We found high agreement between the two TBW measurements with a small but significant difference ($TBW_{D_2O}/TBW_{BIA} = 0.956$). Although we used a trained laboratory for D_2O spectroscopy and clinical staff to measure and administer the doses, there was still one measurement that appeared outside realistic biological bounds. Potential errors in D_2O TBW measurements include subject noncompliance with the fasting and resting requirements before and during the protocol. Strenuous activity or significant food and drink consumption, particularly in the hours immediately before dose consumption and sample collection, can significantly affect accuracy of D_2O TBW measurements [92]. Potential sources of BIA error include electrode placement inaccuracy, poor electrode contact, and significant variability in body shape [207]. Nonetheless, BIA is an appealing method for clinical TBW measurement due to its low cost, rapid results, and amenability to field calibration using stable phantoms. Significant outliers in TBW_{BIA} can be detected by applying thresholds of agreement between duplicate TBW_{BIA} measurements, or comparison to reference physiological hydration ranges for singleton measurements. Using these outlier exclusion methods, the TBW_{BIA} test-retest precision was 1.1%. If the difference between the two measurements exceeds 1.8 kg, we recommend collecting a third measurement and averaging of the two closest measurements. Further validation of TBW_{BIA} precision in different models and using different electrodes (adhesive gel pads vs. touch type) might be useful to expand the utility of this method. Without these outlier detection methods, the observed TBW_{BIA} test-retest precision was 5.2%. Vaché et al. reported precision of 4.1 %CV for test-

retest measurements collected eight hours apart [208]. Further precision studies would be needed to assess the long-term precision of BIA for TBW.

Precision of %Fat measurements from the 4C DXA+BIA method (RMS-SD = 0.8 percent units after BIA outlier removal) was found to be comparable to that of DXA (RMS-SD = 0.6 percent units), suggesting that the method may be suitable for monitoring individual percent fat in longitudinal studies. Precision of 4C DXA+BIA protein measurements was somewhat lower (%CV = 4.4) since protein is a smaller fraction of total body mass. This suggests that 4C DXA+BIA protein may be more suitable for population analysis and individual classification than monitoring of individual protein mass changes.

Our results on the accuracy of 4C DXA+BIA protein measurements versus a reference Lohman model ($R^2 = 0.76$, RMSE = 1.8 kg) are nearly identical to the results found of Wilson [200] who compared 4C DXA+BIA protein versus neutron activation analysis ($R^2 = 0.77$, RMSE = 1.8 kg).

This study had several strengths. To our knowledge, our study is the first to validate the use of BIA for total body water measurements in a 4-component model, and the first to quantify test-retest precision of 4C DXA+BIA measurements. Notably, the present study validates the use of specific DXA and BIA systems (from Hologic and InBody) whereas Wilson's seminal study used systems from different manufacturers (GE and Impedimed). Smith-Ryan used a Hologic DXA system and Impedimed BIA system. While the equations presented herein are specifically calibrated to the particular devices (Hologic DXA and InBody BIA) in this study, the success of this validation

demonstrates the hardware agnosticism of the 4C DXA+BIA approach. Second, we showed how BIA and DXA can be combined to measure hydration. Third, we showed how total body protein can be estimated independently of water status.

However, there were also limitations. Namely, the limited sample of participants included only healthy and normally hydrated individuals. Recruitment was not stratified to target a wide range of body sizes, ethnicities, and ages. We also did not include strength metrics that could have shown if protein is a superior estimate of function than DXA lean mass. Future studies may investigate the robustness of the 4C DXA+BIA model in populations with impaired metabolic and functional profiles, older ages, and abnormal hydration status.

In summary, this work validates the accuracy and precision of a clinically-viable technique incorporating DXA and BIA technology for 4C body composition. Translation to clinical practice would enable fast, accessible 4C assessment including fat, protein, and hydration status - measures important for monitoring of wide variety of conditions including dieting, sarcopenia, cachexia, and performance training. Validation in such special populations is warranted.

6.1.5 Supplement: Effect of the NHANES calibration on DXA %Fat accuracy

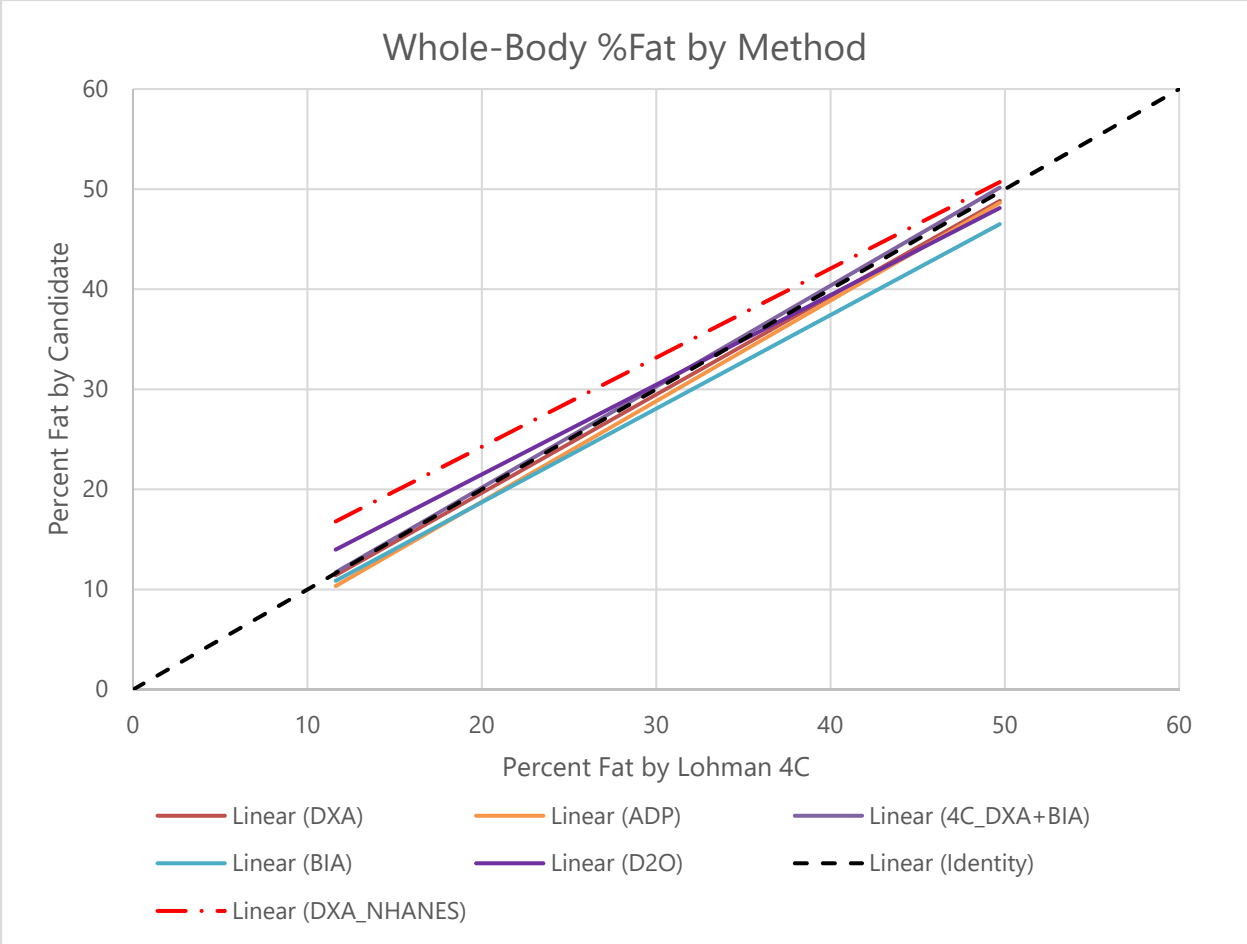
We evaluated percent fat results from DXA with and without the NHANES calibration setting enabled. This calibration was implemented in response to a 2005 publication by Schoeller, et al. that found that DXA underestimated fat mass compared to a few criterion methods (TBW dilution, densitometry, and 4-component analysis) across 7 different studies [132]. The recommendation of

this report was that DXA lean mass measurements be reduced by 5.4% and that fat mass measurements be increased by a corresponding amount of mass.

In the present study, NHANES calibrated-DXA measurements did not agree well with the criterion Lohman 4C model (Figure 6-6). Specifically, NHANES-calibrated DXA percent fat was significantly higher than the Lohman 4C criterion measurement, particularly in leaner individuals: $[PFAT_{DXA, NHANES} = 0.89 * PFAT_{Lohman\ 4C} + 6.45]$. Disabling the NHANES calibration resulted in higher accuracy with the criterion Lohman 4C model: $[PFAT_{DXA} = 0.98 * PFAT_{Lohman\ 4C}]$.

It may be noted that D₂O dilution in the present study, similar to the NHANES-calibrated %Fat, was the only other percent fat measurement that produced a significant bias ($P < 0.05$) versus the Lohman 4C. Four of the seven studies that were used to derive the NHANES calibration used D₂O as the criterion measurement. This is consistent with the present finding of a significant bias in NHANES-calibrated DXA percent fat. However, NHANES-calibrated DXA overestimated percent fat even relative to D₂O (dashed red and solid purple lines in Figure 6-6, respectively).

The small sample size of this study limits the strength of conclusions that can be drawn from these data, however the finding that DXA agrees with the Lohmann 4C and other methods except when the NHANES-calibration is applied, is unexpected. The NHANES-calibrated DXA overestimates fat versus all other methods, including D₂O. These results support re-evaluation of DXA body composition calibration standards to optimize the accuracy of the method.



Method	Slope [95% CI]	Intercept [95% CI]	R ²	RMSE
DXA (NHANES)	0.89 [0.78, 1.00]	6.45 [3.11, 9.78]	0.93	2.83
DXA	0.98 [0.94, 1.03]	n.s.	0.93	2.97
ADP	0.96 [0.94, 0.99]	n.s.	0.98	1.71
BIA	0.94 [0.88, 0.99]	n.s.	0.90	3.83
D₂O	0.90 [0.82, 0.97]	3.56 [1.45, 5.68]	0.97	1.80
4C DXA + BIA	1.01 [0.97, 1.04]	n.s.	0.96	2.33

Figure 6-6: Whole-body percent fat from various body composition assessment methods versus the reference 4C Lohman model. "n.s." indicates that the regression intercept was non-significant and set to zero. This figure matches Figure 3 but includes DXA percent fat with NHANES correction enabled. It can be seen that DXA (NHANES) significantly overestimates percent fat versus all other methods tested, particularly in leaner individuals.

6.2: Ultra DXA + 3D Optical Imaging for True 3C and 4C Whole-Body Imaging

6.2.1 Motivation

As previously mentioned, DXA technology cannot simultaneously resolve more than two tissue types. Lean/fat soft tissue composition is thus estimated at all pixels containing bone by inferring composition from the nearest bone-free pixels. This results in significant interpolation in up to about 60% of all pixels in a whole-body image (Figure 6-7). Because of this significant interpolation, DXA measurements of all three compartments (3C: bone, fat, lean) are highly sensitive to positioning. This limits accuracy and precision of the method and prohibits true measurement of the spatial distribution of fat over the ribcage within the torso.

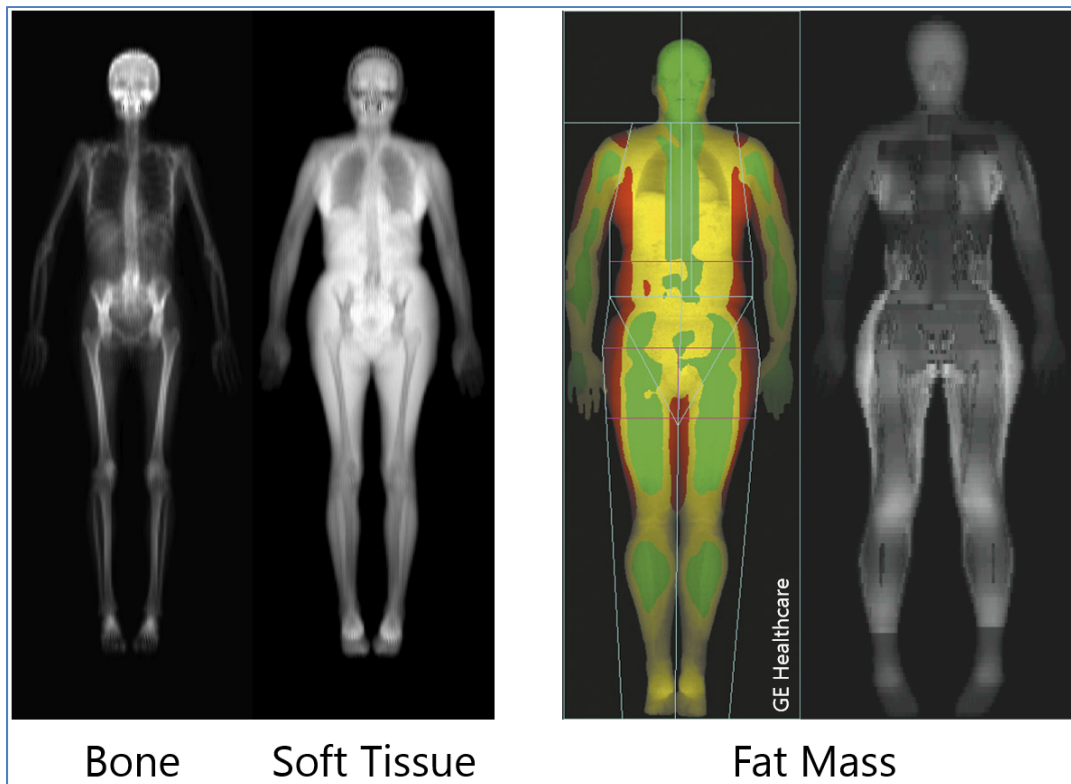


Figure 6-7: DXA can simultaneously resolve two tissue compartments (bone and homogenous soft tissue, left), but not three (bone, lean, and fat). Consequently, soft tissue composition must be interpolated in all pixels containing bone (right).

6.2.2 Theory

To overcome the two-compartment limitation of DXA, body thickness at each pixel will be directly measured using 3D surface scanning. Specifically, body thickness will be measured using a set of 3D depth sensing cameras mounted adjacent to the X-ray detector array and source of the DXA system. To facilitate imaging of the subject's posterior surface, the scanner table will be replaced with an optically-transparent acrylic tabletop. Depth streams from the cameras will be processed using temporal fusion to construct a high-resolution 3D model of the patient's body as the C-arm sweeps across the table [209]. The assembled 3D depth data allows for independent estimation of X-ray path lengths corresponding to each DXA pixel.

Using the low-energy (100 kVp) and high-energy (140 kVp) X-ray attenuation measurements A_{LE} and A_{HE} , along with total thickness T , three-compartment (bone/fat/lean) composition at each pixel can be estimated using the following monochromatic model (Equation 6-1), where $\mu_{j,k}$ is the linear attenuation coefficient and t_j is single-compartment thickness for material j at energy level k . Here y is the vector of measurements used to estimate x , the vector of component tissue thicknesses.

$$A = \begin{bmatrix} \mu_{\text{bone,LE}} & \mu_{\text{lean,LE}} & \mu_{\text{fat,LE}} \\ \mu_{\text{bone,HE}} & \mu_{\text{lean,HE}} & \mu_{\text{fat,HE}} \\ 1 & 1 & 1 \end{bmatrix} \quad x = \begin{bmatrix} t_{\text{bone}} \\ t_{\text{lean}} \\ t_{\text{fat}} \end{bmatrix} \quad y = \begin{bmatrix} A_{LE} \\ A_{HE} \\ T \end{bmatrix}$$

$$y = Ax$$

Equation 6-1: Monochromatic model for 3-compartment estimation at each pixel.

For accurate measurement, corrections for beam hardening introduced by the polychromatic nature of the tungsten X-ray source in the DXA scanner must be implemented. This will be achieved by utilizing a polynomial approximation of the power series relationship (Equation 6-2) between

tissue thickness and polychromatic attenuation as defined previously for 3-compartment breast imaging [210]. We expect this technique to scale to whole-body composition assessment because target thicknesses are larger in a whole-body scan than a breast scan, and the primary components of interest (bone, lean, and fat) have greater separation in X-ray attenuation characteristics than do the components separated from breast images (water, protein, and fat).

$$t_j = \sum_{(\alpha,\beta,\gamma) \in N} a_{\alpha\beta\gamma,j} A_{HE}^\alpha R^\beta T^\gamma$$

$$t_j = a_{1,j} + a_{2,j}A_{HE} + a_{3,j}R + a_{4,j}T + a_{5,j}A_{HE}^2 + a_{6,j}R^2 + a_{7,j}T^2 + a_{8,j}A_{HE}R + a_{9,j}A_{HE}T + a_{10,j}RT$$

Equation 6-2: Power series relationship (upper) between tissue thickness and measured X-ray attenuations and thickness. Here the ratio value $R = A_{LE}/A_{HE}$. Taylor series polynomial approximations (quadratic shown, lower) were calibrated to provide tissue thickness measurements adjusted for polychromatic beam hardening.

Malkov showed conceptual phantom results using a GE Lunar Prodigy densitometer (GE Healthcare, Madison, WI, USA) and Microsoft Kinect (Microsoft, Inc., Redmond, WA, USA) suitable for whole-body imaging [211]. Imaging a phantom with 2, 4, and 6 cm steps, Malkov used experimental DXA attenuation measurements $\{A_{HE}, A_{LE}\}$ and known total thickness T to estimate phantom water, lipid, and protein thicknesses. Malkov found errors (standard deviations) of 0.09 cm (1.6 %), 0.08 cm (1.4 %), and 0.05 cm (4.1 %) for water, lipid, and protein, respectively. He then simulated errors of ± 0.1 cm in T and found that estimated 3C errors increased to 0.19 cm (3.2 %), 0.16 cm (2.7 %), and 0.3 cm (22 %), respectively. Malkov's results demonstrate feasibility and underscore the importance of highly accurate total thickness measurements to the accuracy of this method.

If successful, the Ultra DXA technique could provide true 3C imaging across the whole body, including regions with bone, to allow accurate imaging of fat and lean tissue distribution in the torso. It could also enable interpolated 4C imaging, using the same spatial approximations used to derive 3C composition from two DXA attenuation signals.

6.2.3 Prototype Device and Phantom Studies

We developed a prototype Ultra DXA device (Figure 6-8) by integrating three 3D optical cameras (Kinect, Microsoft, Redmond, WA) above and below a custom optically-transparent tabletop installed on a Hologic Discovery/W densitometer (Hologic, Marlborough, MA). Depth images from the cameras were collected in serial, cycling once every three seconds throughout the duration of the whole-body DXA scan. Measurements were performed in serial to avoid illumination pattern interference between cameras. 3D meshes were assembled using KScan3D software (LMI Technologies, Vancouver Canada) and analyzed in MATLAB R2017a (The MathWorks, Inc., Natick, MA) to estimate X-ray path lengths corresponding to each DXA pixel.

Material separation was demonstrated using multiple scans on a 6-cm step phantom of materials biologically equivalent to fat (machinable wax, McMaster-Carr, Inc., Elmhurst, IL, USA), water (Plastic Water LR, CIRS, Norfolk, VA, USA), and protein (Delrin acetal resin sheets, McMaster-Carr, Inc., Elmhurst, IL, USA). The step phantom is shown in Figure 6-9. The steps were 2, 4, and 6 cm high, at 0, 50, and 100% fat compositions. The total footprint of the step phantom is 12 cm x 12 cm. Five thicknesses of Delrin sheet (0, 3.175, 6.8, 13.5, and 20 mm) were placed under the step phantom. Including an air region of zero thickness adjacent to the step phantom, a total of 46 fat/water/protein thickness combinations were used.



Figure 6-8: Prototype Ultra DXA system with integrated transparent acrylic tabletop and 3D depth cameras.

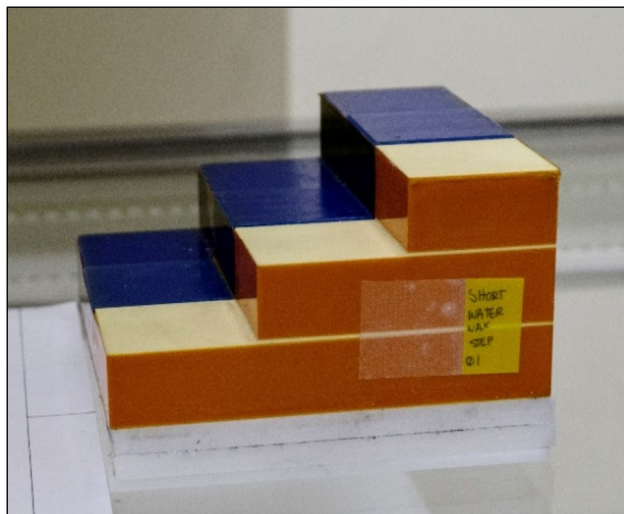
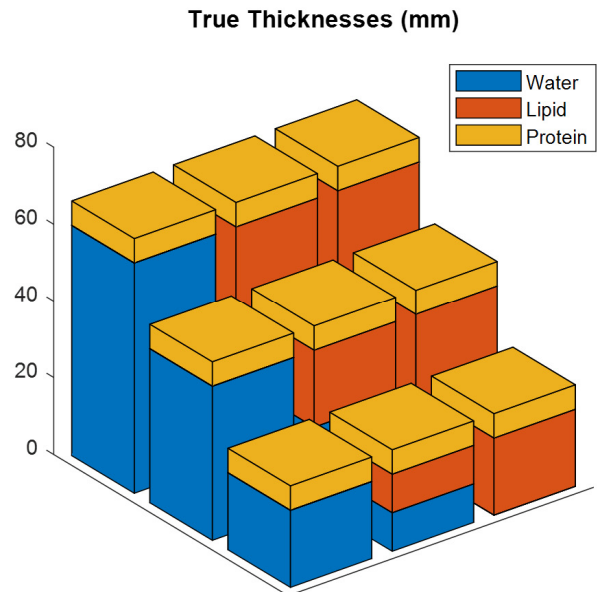


Figure 6-9: Blue wax/plastic water step phantom on Delrin sheets used to approximate water, lipid, and protein, respectively.

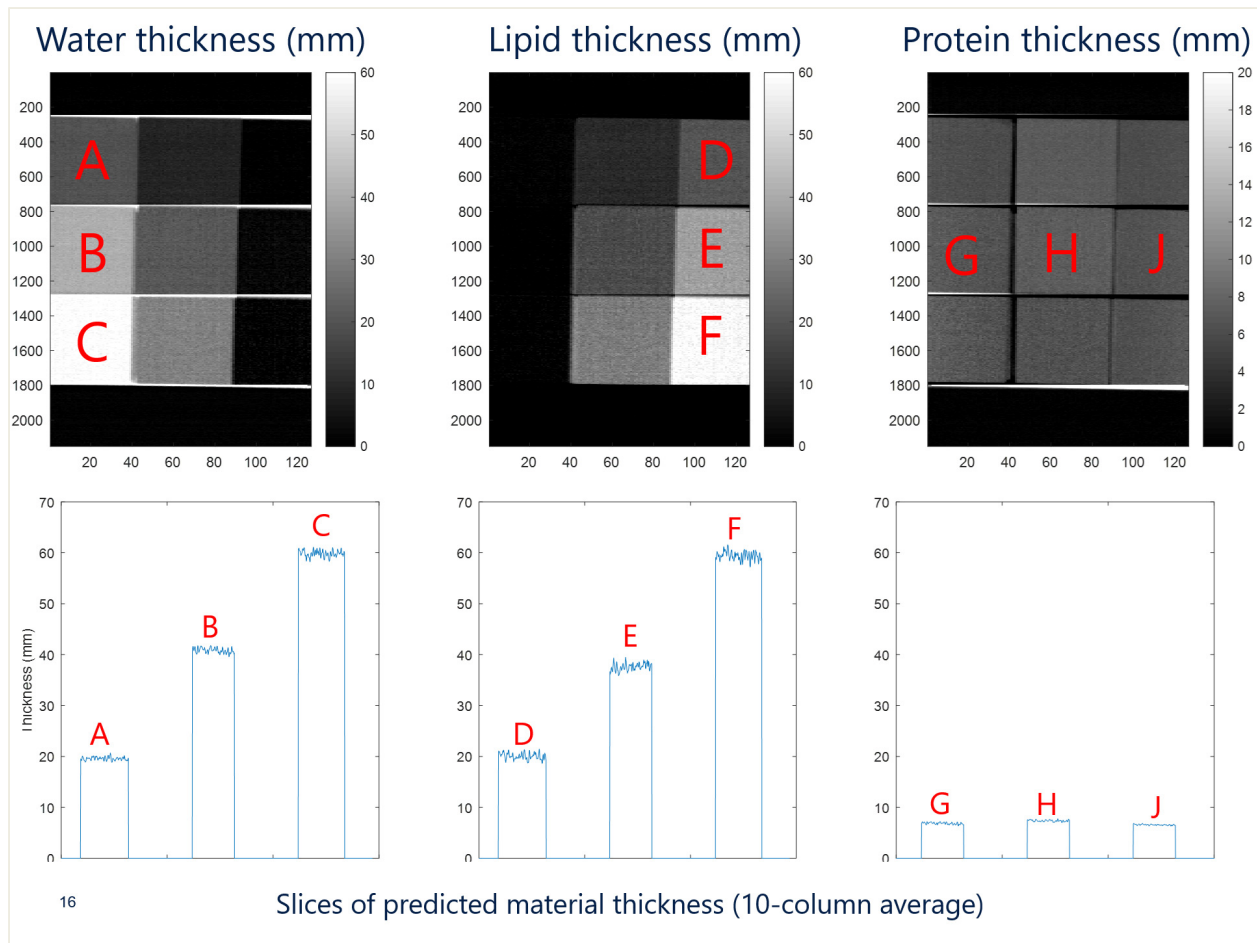


Calibration and 3C Separation

DXA scans were acquired of the step phantom with each of the five Delrin thicknesses. A special high-resolution scan mode was used that produced images with a resolution of 2151 x 126 pixels at a pixel size of approximately 0.08 x 0.90 mm. Regions of at least 33 x 20 pixels were selected in the middle of each step of the phantom object. A_{HE} and A_{LE} were averaged in each region and recorded for each of the 46 unique thickness combinations. These measurements were used with known (measured) thickness values T to calibrate the a coefficients in quadratic and cubic Taylor series polynomials as shown in Equation 6-2 (`regress` in MATLAB). Root mean square errors (RMSE) in thickness estimates across the calibration set using a cubic model were 0.97, 0.87, and 0.91 mm for water, lipid, and protein, respectively. These errors are 5.4, 4.8, and 12.3% of the average phantom thicknesses of water (18 mm), lipid (18 mm), and protein (7.4 mm), respectively.

The calibrated cubic polynomial calibration equation was used to create separate material images of the step phantom fat, water, and protein components (Figure 6-10). Thicknesses were calculated on a per-pixel basis. Median filtering with a window size of 5 pixels was applied (`medfilt2` in MATLAB) to suppress edge artifacts. Cross-sectional thickness profiles across the step phantom for an average of 10 columns are shown in the middle of Figure 6-10. Actual protein (Delrin) thickness in the image shown is 6.35 mm.

Further experiments with increased thicknesses and different materials (including a bone-equivalent phantom such as hydroxyapatite) are warranted to better approximate target materials expected in a whole-body scan, and to determine whether accuracy varies with thickness.



Region	A	B	C	D	E	F	G	H	J
True Thickness (mm)	20	40	60	20	40	60	6.35	6.35	6.35
Estimated Thickness (mm)	20.4	40.0	59.7	19.0	38.6	59.0	6.97	8.01	6.17

Figure 6-10: Isolated water, lipid, and protein images of the step phantom generated using the 3C "Ultra DXA" technique. High-resolution DXA attenuation measurements and known thicknesses were used to derive cubic polynomials to estimate water, fat, and protein composition. Cross-sectional thickness profiles are shown below each image, showing good agreement to the actual dimensions of the step phantom.

3D Mesh Assembly and Thickness Measurements

Total thickness of the 3D step phantom was measured with the depth cameras in a fixed position above and below the phantom. 500 consecutive exposures were collected in this static configuration to assess noise characteristics and quantify the effect of averaging multiple thickness measurements on measurement error. The cameras were connected to a single computer and images

were captured using a KScan3D script. (All relevant scripts for this project can be found in the shepherd-lab/ultradxa repository; see Appendix: Code Availability).

Acquired point cloud images are meshed and exported in PLY polygon file format. Each image is captured in the frame of the camera. Images from the three cameras must be rotated and translated in 3D space to align images into a single, all-around 3D point cloud of the target phantom object. Transformation matrices for each camera are generated by using the Align tool in MeshLab. Unaligned images from each of the three cameras are loaded into a single MeshLab workspace, and common points are selected on each image. One image is selected (“glued”) as the reference frame, and then successive images are aligned to that image using the selected points. In this phantom study, these camera-to-camera translations are the only required alignment transformations. On the other hand, in a whole-body scan, the motion of the system must be considered.

Once the camera-to-camera transformation matrices are derived, those camera-specific transformations are applied to all images from each camera. The transformed point clouds are loaded and merged in MATLAB. Mean \bar{x} and standard deviation s of estimated thickness is calculated at each level of the step phantom (2, 4, and 6 cm) for a single combined/aligned image (one point cloud from each camera). Mean, standard deviation, and standard error of the mean $SEM = s/\sqrt{i}$ are calculated for $i = 1 \rightarrow 500$ images.

Results for SEM of measured thickness are shown in (Figure 6-11). Using one exposure from each camera produced depth images with average thickness errors (SD) of approximately 2.3 mm at each step. Adding additional measurements reduced the SEM continuously. Averaging of 20

complete aligned images reduced error below 0.5 mm. While single exposures from commodity depth cameras such as the Kinect are noisy, multiple exposures can be collected with little additional cost. Provided the hardware supporting the 3D depth cameras is sufficiently powerful, video-rate (30Hz or greater) depth streams can be captured from each camera to easily acquire hundreds of samples in a matter of seconds.

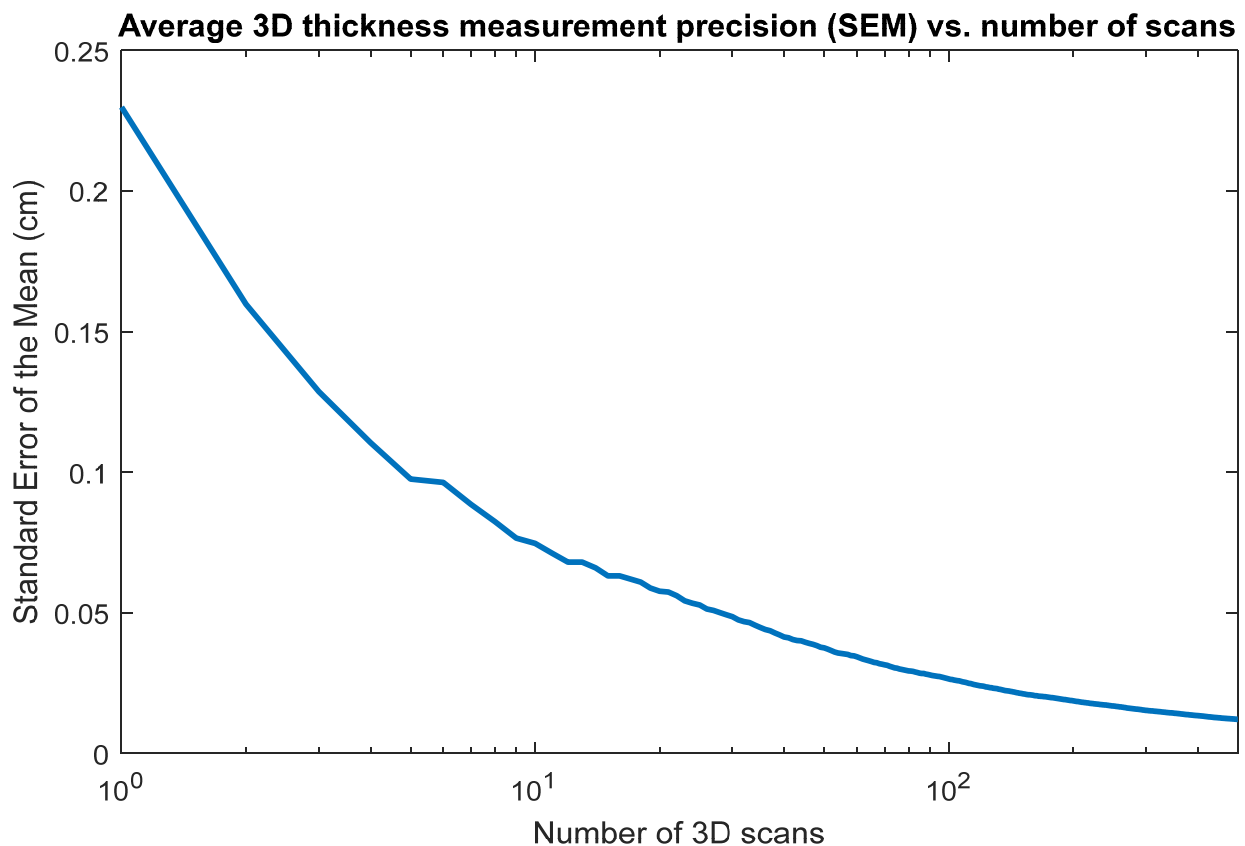


Figure 6-11: Effect of averaging multiple 3D optical depth measurements. We found that averaging of approximately 20 depth measurements reduced error below 0.5 mm.

With this phantom study we demonstrated the feasibility of 3C separation using the Ultra DXA prototype scanner. In the following section we describe a pilot study of human subjects scanned on the system and the progress in image processing as of the writing of this document.

6.2.4 *In Vivo* Pilot Study

To demonstrate the Ultra DXA technique for whole-body imaging, thirty-one healthy adults over the age of eighteen were enrolled in a prospective open recruitment as described in 6.1.2 . All provided informed consent and the study protocol was approved by the UCSF Committee on Human Research (IRB #16-19342).

Each participant was imaged on the prototype Ultra DXA system a total of six times: twice without repositioning and once again with repositioning, at each of two different X-ray energy settings (100/140 kVp standard configuration and 80/140 kVp research configuration). During each scan, depth images were collected from each of the three Kinect cameras mounted on the densitometer. Depth images were acquired in series using a KScan3D script, with a new cycle beginning every three seconds. After acquisition, each captured point cloud was converted to a connected mesh. Meshes were then aligned by camera (1-3) and pass (1-7) to create 21 groups of meshes. KScan3D features meshing and alignment tools for these operations, as well as combining and finalizing tools to clean, smooth, and simplify meshes for export. Alignment in KScan3D uses iterative closest point matching [183]. We provide example aligned and exported images from a single camera over the course of a single pass of the densitometer scan arm in Figure 6-12.

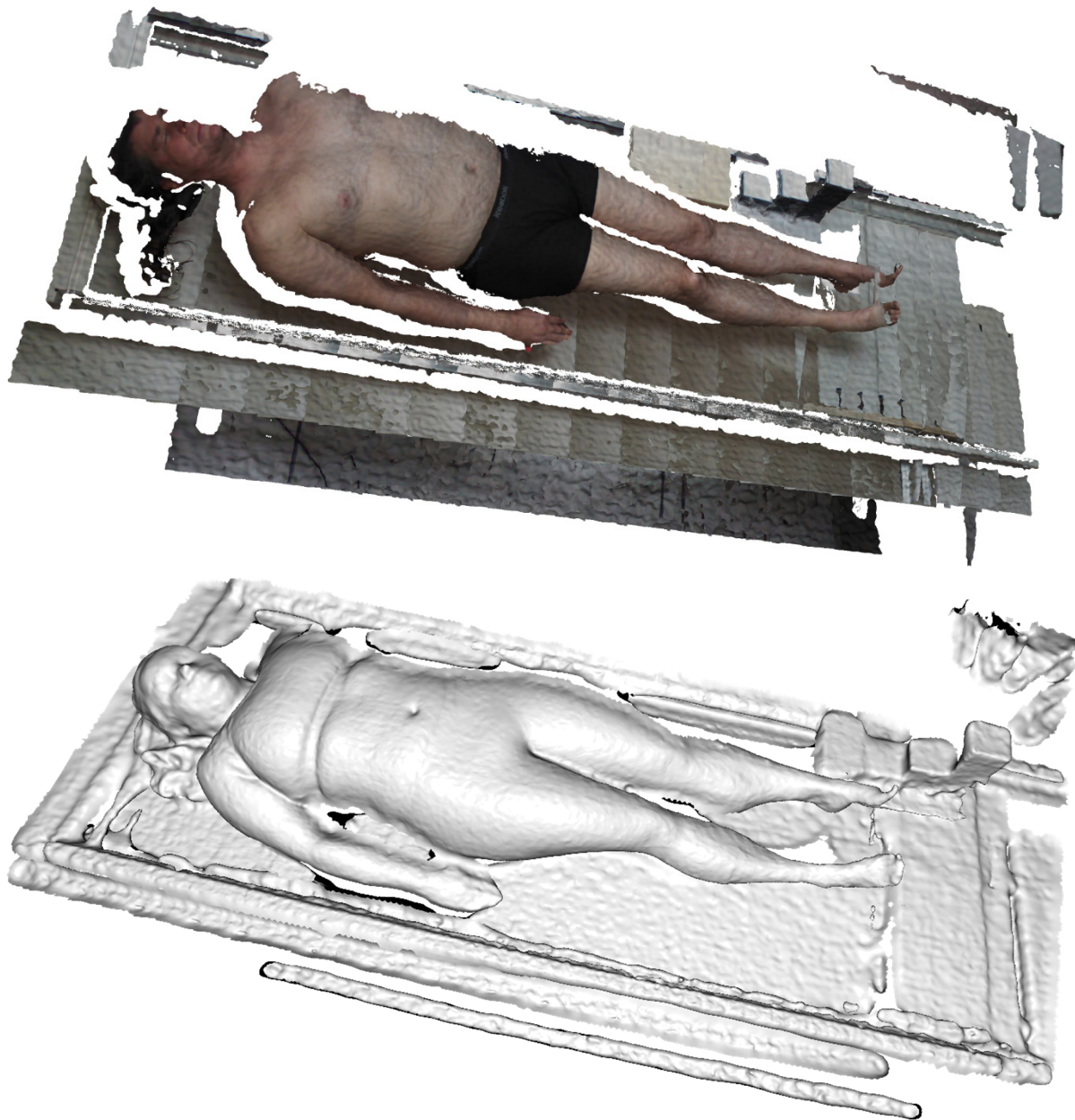


Figure 6-12: Two examples of assembled 3D meshes from depth images collected from a single depth camera over a single pass of the densitometer C arm. Images were collected approximately every 3 seconds and assembled using the Iterative Closest Point algorithm. The presence of many well-defined depth features (e.g. corners and ridges) is necessary for ICP to produce reliable alignments. Smaller participants with less shape features or smaller bodies may prove more problematic for alignment particularly near the feet end of the scanner and between scan passes.

As of this writing, significant effort has been devoted to processing the 3D depth images collected throughout all seven passes of the whole-body scans. However, we have not yet implemented robust alignment across all cameras and all passes of a scan, and as a result compositional images are yet to be calculated. While single-camera, single-pass alignment works reliably to produce images like those shown in Figure 6-12, drift in the ICP algorithm presents problems for precise alignment throughout the duration of a multi-pass scan. The configuration and dynamics of the scanner present challenges to alignment. Specifically, the table and C-arm both move during a whole-body scan, producing multiple simultaneous object movements in the field of view. This leads to errors in alignment that can quickly compound since each depth image is aligned to the last. An example of a failed alignment is shown in Figure 6-13 (left).

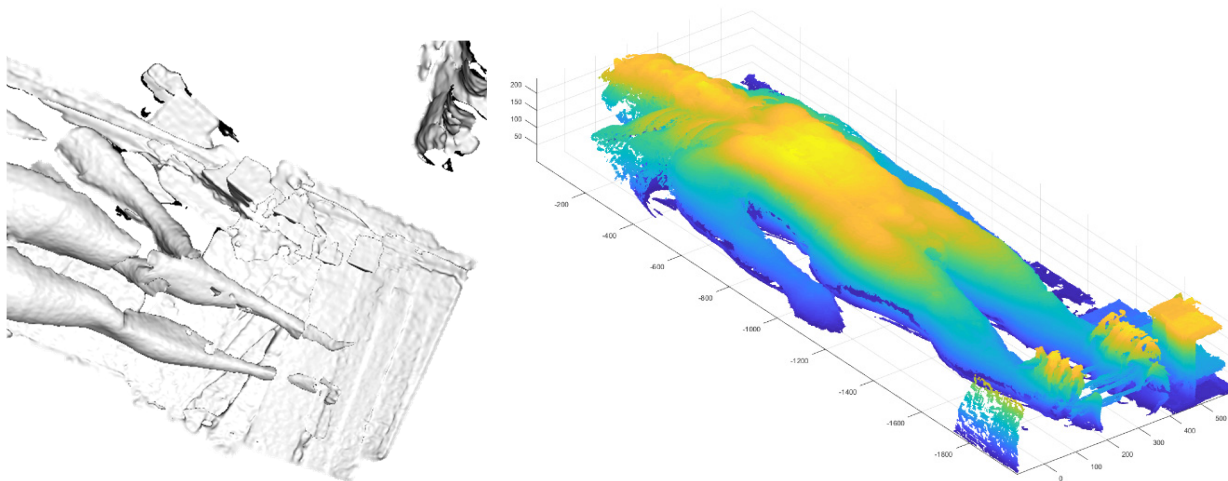


Figure 6-13: Challenges in alignment of 3D depth images. In regions with few distinct depth features (e.g. the feet shown at left), there may be insufficient correspondence for reliable alignment. One failed image alignment can then cause subsequent images to align incorrectly. Timing information can be used with the known movement of the densitometer to predict the exact location at which each image was taken (right).

6.2.5 Summary and Challenges

With this initial work we have developed a prototype system integrating depth cameras on a modified DXA system. Using high-resolution DXA attenuation measurements and caliper-measured thicknesses, we calibrated quadratic and cubic polynomial imaging equations using a 2/4/6-cm thick step phantom of water/fat/protein equivalent materials. The cubic model provided 3-component thickness separation on images of the phantom with RMSE < 1 mm for each material. We developed a protocol for acquiring depth images sequentially from three Microsoft Kinect cameras at a frequency of one complete acquisition (i.e. one image from each camera) every three seconds. Given the 45-second pass time of the densitometer in whole-body scan mode, this translates to approximately 15 depth images acquired over the 196 cm length of the scan table. Using depth images of the step phantom we found that single-image thickness error (SD) was about 2.3 mm. Averaging approximately 20 depth measurements reduced standard error of the mean (SEM) of thickness measurement below 0.5 mm. Higher depth image acquisition rates could be used to improve quality of thickness measurements. All relevant image acquisition code as well as processing and analysis scripts developed for this project can be found in the shepherd-lab/ultradxa repository (see Appendix: Code Availability).

We used the prototype system to collect *in vivo* DXA and 3D image data on thirty-one healthy participants. Processing of the image data is ongoing. The primary challenge as of this writing is development of a robust algorithm for aligning the depth images collected throughout the scan. A more robust approach to alignment would be to (1) use knowledge of the programmed movements of the densitometer to provide initial alignment for each depth image in 3D space, (2) enforce

limitations on the degrees of freedom for image-to-image transformation based upon the known geometry of the system, and (3) use ICP or similar algorithms for fine adjustments rather than coarse alignment. Additionally, fiducial markers placed along the table may provide useful landmarks to assist the registration algorithms.

We have characterized the movement of the densitometer during a whole-body scan and implemented preliminary timing-based alignment by predicting the location of the cameras at any specific time during a scan. The time of each point cloud is calculated by comparing the file creation timestamp on each depth image with the start time of the DXA scan. We use measured motion patterns of the densitometer to programmatically estimate camera position as a function of time. An example of a timing-aligned mesh is shown in Figure 6-13 (right). Note that there are artifacts due to inaccuracies in the location prediction, particularly during the lateral transition phases between passes. Additional denoising, cropping, and fine alignment are necessary to remove extraneous objects in the scene and produce a clean, closed 3D mesh amenable to slicing and thickness measurement along the X-ray paths of the densitometer. These tasks are left as future work.

At a more fundamental level, the Ultra DXA imaging technique requires very high precision thickness and X-ray attenuation measurements. Equation 6-1 encapsulates the underlying principle of the technique. A potential issue is the stability of this imaging equation, as the A matrix has a condition number on the order of 10^3 at the default tube voltages of the DXA scanner. Numerical simulations of a three-compartment phantom including 1% white noise on the measurement vector y produce a signal-to-noise ratio loss from $SNR_y = 59.3$ to $SNR_{\hat{x}} = 9.5$. This is due to limited orthogonality between 3D depth and X-ray attenuation measurements and underscores the need for

highly precise individual measurements. Potential options for improving system stability include adjustment of tube energy levels to afford greater attenuation coefficient separation, or use of a more precise 3D depth imaging hardware (e.g. laser line scanners).

Moving forward, the 3D depth imaging component of this project could be improved with integration of newer sensors such as the Intel RealSense D435 (Intel Corp., Santa Rosa, CA, USA) that provides significantly improved depth resolution (up to 1280x720p) and framerate (up to 90 Hz) as well as global shutter and more sophisticated onboard processing [212]. With appropriate software, these newer sensors may enable simultaneous 60 Hz+ acquisition and alignment of depth measurements on a single system where the present setup and protocol was limited to 0.33 Hz. Higher frequency acquisition would improve the quality of thickness measurements and may mitigate the alignment challenges due to increased image-to-image correspondence. However, with increased resolution and sampling rate it is more critical to develop a real-time alignment strategy to cope with the high data rate of acquisition. As a reference, 30 Hz 640x480p video rate acquisition of color and depth streams (RGB-D) from a single Kinect camera for seven minutes (a duration long enough to cover a whole-body scan on the prototype system) produces about 10.5 GB of data.

Tighter integration with the densitometer hardware (e.g. synchronizing with the stepper motors that drive table and scanner arm movements) could be used to more reliably align 3D thickness measurements with absorptiometry measurements and further mitigate the need for empirical post-hoc alignment. With further development to reliably match 3D optical and DXA measurements, true *in vivo* 3-component Ultra DXA imaging may be demonstrated and characterized.

7 | Future Directions

Several of the studies contained in this dissertation are built around principal component analysis of image data to produce compact representations of 3D shape or 2D tissue appearance. A logical next step would be to apply these techniques to magnetic resonance imaging data to begin to understand the key features of 3D internal body composition. Appearance modeling techniques have been successfully applied for several 3D medical image segmentation tasks [213]–[215].

Furthermore, other statistical methods beyond PCA could be explored to better detect composition features specifically indicative of selected risk and outcome variables. Methods such as linear discriminant analysis and deep neural networks have provided revolutionary performance in several image classification, segmentation, and analysis tasks [216]–[220], and the 3D and DXA data discussed herein are ripe for this type of analysis. Supervised statistical learning of course brings with it an increased risk of model overfitting, so increased data collection and diligent validation and data augmentation practices should be priorities.

One limitation of the statistical shape and appearance models described above is that they all require some degree of manual annotation to register and analyze new images. This can be a time-consuming process that requires trained readers. Additional training and careful refinement of fitting models [153] may mitigate the need for manual annotation, and more advanced fitting and segmentation algorithms may allow for further automation [219], [221]–[223]. Automation is highly desirable both for efficiency and practicality of deploying these techniques to end users. More sophisticated 3D body shape models informed by internal joint structure and tissue deformation in

motion may be investigated to provide better fitting, registration, and pose correction of 3D body scans from many different devices [224]–[226]. Estimation of 3D body shape from 2D images [227], [228] could enable even greater access to metabolic risk assessment using nothing more than a cell phone camera.

The promising validation of the rapid 4C DXA+BIA technique in healthy adults warrants further validation in target populations of growing children, older adults, and individuals with cachexia and sarcopenia. Such work would provide insight into the generalizability of the method. Analysis of 3D body shape as contained in the Shape Up! studies could be extended to include more longitudinal components and investigation of body shape changes in response to different diet and activity interventions. Understanding of shape changes in the individual would inform body shape models that can more accurately predict realistic change for a specific person.

8 | Conclusions

Over the course of this dissertation we developed techniques to capture and analyze detailed information about 3D body shape and internal tissue distribution. These studies are built around accessible 3D optical body scanners that are increasingly accessible, with products now in consumer homes, and low-dose whole-body dual energy X-ray absorptiometry. A central theme of these works is leveraging available technologies in novel ways to extract more meaningful clinical health insight.

We demonstrated algorithms for high-resolution quantitative fat, lean, and bone image derivation from standard whole-body DXA scans. We applied these algorithms and created statistical appearance models of whole-body thickness, fat, and lean tissue distribution in populations of older adults across five different ethnicities. We showed that these models can be used to classify sex (AUC = 0.99), race (AUC = 0.91), and 10-year mortality (AUC = 0.66) in a study of older black and white adults. We then applied these techniques to a study of older adults of five different ethnicities to reveal characteristic phenotypes of body fat distribution by ethnicity and show that fat distribution alone can accurately predict metabolic syndrome status (validation AUC = 0.82-0.87) and diabetes status (validation AUC = 0.68-0.75) without the need for ethnicity-specific adjustments.

As a pilot investigation, we characterized the accuracy and precision of commercial 3D optical body scanners for clinical circumference, surface area, and total body volume measurements ($R^2 \geq 0.92$) and showed that these measurements could be used to predict total and regional body composition (whole-body fat mass validation $R^2 = 0.76$, RMSE = 3.72 kg). These results were used as preliminary data to secure NIH funding for the launch of the Shape Up! Adults and Kids studies.

As part of ongoing Shape Up! analysis, we built detailed 3D statistical shape models that efficiently capture 95% of body shape variance and demonstrated that these models offer improved body composition accuracy (whole-body fat mass cross validation $R^2 = 0.89$, RMSE = 2.80 kg) over traditional techniques and test-retest precision reasonably comparable to DXA (whole-body fat mass RMSE = 1.02 kg / 0.67 kg, %CV = 5.0 / 2.7 for males/females respectively). 3D optical body scanning is a rapidly growing market and the technology is uniquely amenable to widespread and frequent individual assessment. The findings from these studies could provide enhanced metabolic health insight to clinicians and individuals all around the world.

We validated the accuracy and precision of a rapid DXA and bioelectrical impedance technique to provide four-component body composition comparable to gold-standard techniques (%Fat $R^2 = 0.96$, RMSE = 2.33 units, test-retest RMS-SD = 0.8 units; 4C protein $R^2 = 0.76$, RMSE = 1.8 kg, test-retest %CV = 4.4). We discussed implementation and calibration considerations to bring this rapid 4C method to the clinic where traditional 4C protocols are impractical. Finally, we conceptualized a novel integrated 3D optical + DXA device called “Ultra DXA” for true 3C and interpolated 4C imaging of the whole body. We built a prototype of this device, demonstrated proof of concept phantom results (separated water, fat, protein RMSE < 1 mm each), and collected *in vivo* data for preliminary analysis and development.

In total, these works provide affirmative evidence that detailed descriptors of body shape and composition reveal meaningful health risk markers beyond traditional methods. By building upon proven, accessible technologies, these findings provide enabling translatable tools for clinicians and individuals to better assess metabolic status and track progress towards improved health.

References

- [1] “WHO | Obesity and overweight,” *WHO*. [Online]. Available: <http://www.who.int/mediacentre/factsheets/fs311/en/>. [Accessed: 08-Nov-2017].
- [2] “WHO | 10 facts on obesity,” *WHO*. [Online]. Available: <http://www.who.int/features/factfiles/obesity/en/>. [Accessed: 03-Apr-2018].
- [3] Y. Wang and H. Lim, “The global childhood obesity epidemic and the association between socio-economic status and childhood obesity,” *Int. Rev. Psychiatry*, vol. 24, no. 3, pp. 176–188, Jun. 2012.
- [4] “WHO | Childhood overweight and obesity,” *WHO*. [Online]. Available: <http://www.who.int/dietphysicalactivity/childhood/en/>. [Accessed: 03-Apr-2018].
- [5] M. Arnold *et al.*, “Global burden of cancer attributable to high body-mass index in 2012: a population-based study,” *Lancet Oncol.*, vol. 16, no. 1, pp. 36–46, Jan. 2015.
- [6] E. A. Finkelstein, J. G. Trogon, J. W. Cohen, and W. Dietz, “Annual Medical Spending Attributable To Obesity: Payer-And Service-Specific Estimates,” *Health Aff. (Millwood)*, vol. 28, no. 5, pp. w822–w831, Sep. 2009.
- [7] E. A. Finkelstein *et al.*, “Obesity and severe obesity forecasts through 2030,” *Am. J. Prev. Med.*, vol. 42, no. 6, pp. 563–570, Jun. 2012.
- [8] Y. C. Wang, K. McPherson, T. Marsh, S. L. Gortmaker, and M. Brown, “Health and economic burden of the projected obesity trends in the USA and the UK,” *The Lancet*, vol. 378, no. 9793, pp. 815–825, Sep. 2011.
- [9] B. A. Swinburn, D. Jolley, P. J. Kremer, A. D. Salbe, and E. Ravussin, “Estimating the effects of energy imbalance on changes in body weight in children,” *Am. J. Clin. Nutr.*, vol. 83, no. 4, pp. 859–863, Jun. 2006.
- [10] A. H. Slyper, “The Pediatric Obesity Epidemic: Causes and Controversies,” *J. Clin. Endocrinol. Metab.*, vol. 89, no. 6, pp. 2540–2547, Jun. 2004.
- [11] E. J. McAllister *et al.*, “Ten Putative Contributors to the Obesity Epidemic,” *Crit. Rev. Food Sci. Nutr.*, vol. 49, no. 10, pp. 868–913, Nov. 2009.
- [12] R. V. Burkhauser and J. Cawley, “Beyond BMI: The value of more accurate measures of fatness and obesity in social science research,” *J. Health Econ.*, vol. 27, no. 2, pp. 519–529, Mar. 2008.
- [13] WHO Expert Consultation, “Appropriate body-mass index for Asian populations and its implications for policy and intervention strategies,” *Lancet Lond. Engl.*, vol. 363, no. 9403, pp. 157–163, Jan. 2004.
- [14] E. M. Evans, D. A. Rowe, S. B. Racette, K. M. Ross, and E. McAuley, “Is the current BMI obesity classification appropriate for black and white postmenopausal women?,” *Int. J. Obes.*, vol. 30, no. 5, pp. 837–843, May 2006.
- [15] T. J. Cole, M. S. Faith, A. Pietrobelli, and M. Heo, “What is the best measure of adiposity change in growing children: BMI, BMI %, BMI z-score or BMI centile?,” *Eur. J. Clin. Nutr.*, vol. 59, no. 3, pp. 419–425, Mar. 2005.

- [16] Alberti K. G. M. M., Zimmet P., and Shaw J., “Metabolic syndrome—a new world-wide definition. A Consensus Statement from the International Diabetes Federation,” *Diabet. Med.*, vol. 23, no. 5, pp. 469–480, Apr. 2006.
- [17] P. L. Huang, “A comprehensive definition for metabolic syndrome,” *Dis. Model. Mech.*, vol. 2, no. 5–6, pp. 231–237, 2009.
- [18] S. M. Grundy *et al.*, “Diagnosis and Management of the Metabolic Syndrome: An American Heart Association/National Heart, Lung, and Blood Institute Scientific Statement,” *Circulation*, vol. 112, no. 17, pp. 2735–2752, Oct. 2005.
- [19] W. H. Organization, *Global report on diabetes*. World Health Organization, 2016.
- [20] E. Selvin *et al.*, “Glycated Hemoglobin, Diabetes, and Cardiovascular Risk in Nondiabetic Adults,” *N. Engl. J. Med.*, vol. 362, no. 9, pp. 800–811, Mar. 2010.
- [21] N. R. F. Collaboration, “Worldwide trends in diabetes since 1980: a pooled analysis of 751 population-based studies with 4. 4 million participants,” *The Lancet*, vol. 387, no. 10027, pp. 1513–1530, 2016.
- [22] W. H. Organization, *The selection and use of essential medicines: report of the WHO Expert Committee, 2017 (including the 20th WHO Model List of Essential Medicines and the 6th Model List of Essential Medicines for Children)*. World Health Organization, 2017.
- [23] M. Maggard-Gibbons *et al.*, “Bariatric surgery for weight loss and glycemic control in nonmorbidly obese adults with diabetes: a systematic review,” *Jama*, vol. 309, no. 21, pp. 2250–2261, 2013.
- [24] M. A. Colchero, J. Rivera-Dommarco, B. M. Popkin, and S. W. Ng, “In Mexico, evidence of sustained consumer response two years after implementing a sugar-sweetened beverage tax,” *Health Aff. (Millwood)*, vol. 36, no. 3, pp. 564–571, 2017.
- [25] L. D. Silver *et al.*, “Changes in prices, sales, consumer spending, and beverage consumption one year after a tax on sugar-sweetened beverages in Berkeley, California, US: A before-and-after study,” *PLoS Med.*, vol. 14, no. 4, p. e1002283, 2017.
- [26] A. J. Cruz-Jentoft *et al.*, “Sarcopenia: European consensus on definition and diagnosisReport of the European Working Group on Sarcopenia in Older PeopleA. J. Cruz-Gentoft et al.,” *Age Ageing*, vol. 39, no. 4, pp. 412–423, Jul. 2010.
- [27] S. D. Anker, J. E. Morley, and S. Haehling, “Welcome to the ICD-10 code for sarcopenia,” *J. Cachexia Sarcopenia Muscle*, vol. 7, no. 5, pp. 512–514, Dec. 2016.
- [28] D. R. Thomas, “Loss of skeletal muscle mass in aging: examining the relationship of starvation, sarcopenia and cachexia,” *Clin. Nutr.*, vol. 26, no. 4, pp. 389–399, 2007.
- [29] A. B. Newman *et al.*, “Strength, But Not Muscle Mass, Is Associated With Mortality in the Health, Aging and Body Composition Study Cohort,” *J. Gerontol. A. Biol. Sci. Med. Sci.*, vol. 61, no. 1, pp. 72–77, Jan. 2006.
- [30] B. H. Goodpaster *et al.*, “The Loss of Skeletal Muscle Strength, Mass, and Quality in Older Adults: The Health, Aging and Body Composition Study,” *J. Gerontol. Ser. A*, vol. 61, no. 10, pp. 1059–1064, Oct. 2006.
- [31] “Facts and Statistics | International Osteoporosis Foundation.” [Online]. Available: <https://www.iofbonehealth.org/facts-statistics>. [Accessed: 01-May-2018].

- [32] “Bone Density Test, Osteoporosis Screening & T-score Interpretation,” *National Osteoporosis Foundation*. [Online]. Available: <https://www.nof.org/patients/diagnosis-information/bone-density-examtesting/>. [Accessed: 01-May-2018].
- [33] “2015 ISCD Official Positions - Adult - International Society for Clinical Densitometry (ISCD).” .
- [34] J. A. Kanis, A. Oden, H. Johansson, F. Borgström, O. Ström, and E. McCloskey, “FRAX® and its applications to clinical practice,” *Bone*, vol. 44, no. 5, pp. 734–743, May 2009.
- [35] R. Hambli, “Micro-CT finite element model and experimental validation of trabecular bone damage and fracture,” *Bone*, vol. 56, no. 2, pp. 363–374, 2013.
- [36] A. M. Parfitt, “Trabecular bone architecture in the pathogenesis and prevention of fracture,” *Am. J. Med.*, vol. 82, no. 1, pp. 68–72, 1987.
- [37] “Osteoporosis Treatment: How to Choose the Right Medication,” *National Osteoporosis Foundation*. [Online]. Available: <https://www.nof.org/patients/treatment/>. [Accessed: 01-May-2018].
- [38] X. Chen, G. Mao, and S. X. Leng, “Frailty syndrome: an overview,” *Clin. Interv. Aging*, vol. 9, pp. 433–441, Mar. 2014.
- [39] H.-M. Ji, J. Han, and Y.-Y. Won, “Sarcopenia and Osteoporosis,” *Hip Pelvis*, vol. 27, no. 2, pp. 72–76, Jun. 2015.
- [40] A. Heinonen *et al.*, “Randomised controlled trial of effect of high-impact exercise on selected risk factors for osteoporotic fractures,” *The Lancet*, vol. 348, no. 9038, pp. 1343–1347, Nov. 1996.
- [41] J.-Y. Reginster, C. Beaudart, F. Buckinx, and O. Bruyère, “Osteoporosis and sarcopenia: two diseases or one?,” *Curr. Opin. Clin. Nutr. Metab. Care*, vol. 19, no. 1, pp. 31–36, Jan. 2016.
- [42] M. J. Ormsbee *et al.*, “Osteosarcopenic obesity: the role of bone, muscle, and fat on health,” *J. Cachexia Sarcopenia Muscle*, vol. 5, no. 3, pp. 183–192, Sep. 2014.
- [43] C. M. M. Prado, J. C. K. Wells, S. R. Smith, B. C. M. Stephan, and M. Siervo, “Sarcopenic obesity: A Critical appraisal of the current evidence,” *Clin. Nutr.*, vol. 31, no. 5, pp. 583–601, Oct. 2012.
- [44] F. Sofi, F. Cesari, R. Abbate, G. F. Gensini, and A. Casini, “Adherence to Mediterranean diet and health status: meta-analysis,” *BMJ*, vol. 337, p. a1344, Sep. 2008.
- [45] W. H. Organization, *Global action plan for the prevention and control of NCDs 2013-2020*. 2013. 2016.
- [46] W. Shen, M. P. St-Onge, Z. Wang, and S. B. Heymsfield, “Study of body composition: an overview,” *Hum. Body Compos.*, vol. 2, pp. 3–14, 2005.
- [47] “NHANES - National Health and Nutrition Examination Survey Homepage,” 24-Apr-2018. [Online]. Available: <https://www.cdc.gov/nchs/nhanes/index.htm>. [Accessed: 03-May-2018].
- [48] Z. M. Wang, R. N. Pierson, and S. B. Heymsfield, “The five-level model: a new approach to organizing body-composition research,” *Am. J. Clin. Nutr.*, vol. 56, no. 1, pp. 19–28, Jul. 1992.
- [49] H. H. Mitchell, T. S. Hamilton, F. R. Steggerda, and H. W. Bean, “The chemical composition of the adult human body and its bearing on the biochemistry of growth,” *J. Biol. Chem.*, vol. 158, no. 3, pp. 625–637, 1945.

- [50] A. R. Behnke, "Physiologic studies pertaining to deep sea diving and aviation, especially in relation to the fat content and composition of the body: the Harvey lecture, March 19, 1942," *Bull. N. Y. Acad. Med.*, vol. 18, no. 9, p. 561, 1942.
- [51] W. E. Siri, "Body composition from fluid spaces and density: analysis of methods. 1961," *Nutr. Burbank Los Angel. Cty. Calif*, vol. 9, no. 5, pp. 480–491; discussion 480, 492, Oct. 1993.
- [52] A. Bazzocchi, D. Diano, U. Albisinni, G. Marchesini, G. Battista, and G. Guglielmi, "Liver in the analysis of body composition by dual-energy X-ray absorptiometry," *Br. J. Radiol.*, vol. 87, p. 20140232, Jun. 2014.
- [53] S. B. Heymsfield *et al.*, "Multi-component molecular-level body composition reference methods: evolving concepts and future directions," *Obes. Rev.*, vol. 16, no. 4, pp. 282–294, Apr. 2015.
- [54] P. R. Schloerb, B. J. Friis-Hansen, I. S. Edelman, A. K. Solomon, and F. D. Moore, "The measurement of total body water in the human subject by deuterium oxide dilution: With a consideration of the dynamics of deuterium distribution," *J. Clin. Invest.*, vol. 29, no. 10, pp. 1296–1310, 1950.
- [55] J. R. Cameron and J. Sorenson, "Measurement of bone mineral in vivo: an improved method," *Science*, vol. 142, no. 3589, pp. 230–232, 1963.
- [56] A. Selinger, "The body as a three component system," University of Illinois at Urbana-Champaign, 1977.
- [57] R. B. Mazess, J. R. Cameron, and J. A. Sorenson, "Determining body composition by radiation absorption spectrometry," *Nature*, vol. 228, no. 5273, p. 771, 1970.
- [58] J. A. Stein, J. L. Lazewatsky, and A. M. Hochberg, "Dual-energy x-ray bone densitometer incorporating an internal reference system," in *Radiological Society of North America 73rd scientific assembly and annual meeting (Abstracts)*, 1987.
- [59] Z. Wang *et al.*, "Multicomponent methods: evaluation of new and traditional soft tissue mineral models by in vivo neutron activation analysis," *Am. J. Clin. Nutr.*, vol. 76, no. 5, pp. 968–974, 2002.
- [60] D. Hans *et al.*, "Skeletal Sites for Osteoporosis Diagnosis: The 2005 ISCD Official Positions," *J. Clin. Densitom.*, vol. 9, no. 1, pp. 15–21, Jan. 2006.
- [61] N. Sarkalkan, H. Weinans, and A. A. Zadpoor, "Statistical shape and appearance models of bones," *Bone*, vol. 60, pp. 129–140, 2014.
- [62] J. C. Baker-LePain, K. R. Luker, J. A. Lynch, N. Parimi, M. C. Nevitt, and N. E. Lane, "Active shape modeling of the hip in the prediction of incident hip fracture," *J. Bone Miner. Res.*, vol. 26, no. 3, pp. 468–474, 2011.
- [63] B. Schuler, K. D. Fritscher, V. Kuhn, F. Eckstein, T. M. Link, and R. Schubert, "Assessment of the individual fracture risk of the proximal femur by using statistical appearance models," *Med. Phys.*, vol. 37, no. 6, pp. 2560–2571, Jun. 2010.
- [64] J. A. Shepherd, J. T. Schousboe, S. B. Broy, K. Engelke, and W. D. Leslie, "Executive Summary of the 2015 ISCD Position Development Conference on Advanced Measures From DXA and QCT: Fracture Prediction Beyond BMD," *J. Clin. Densitom.*, vol. 18, no. 3, pp. 274–286, Jul. 2015.

- [65] R. A. McGregor, D. Cameron-Smith, and S. D. Poppitt, "It is not just muscle mass: a review of muscle quality, composition and metabolism during ageing as determinants of muscle function and mobility in later life," *Longev. Heal.*, vol. 3, p. 9, Dec. 2014.
- [66] K. M. Beavers *et al.*, "Associations between body composition and gait-speed decline: results from the Health, Aging, and Body Composition study," *Am. J. Clin. Nutr.*, vol. 97, no. 3, pp. 552–560, Mar. 2013.
- [67] A. H. FAIRFAX, R. BALNAVE, and R. D. ADAMS, "Variability of grip strength during isometric contraction," *Ergonomics*, vol. 38, no. 9, pp. 1819–1830, Sep. 1995.
- [68] Kuk Jennifer L., Katzmarzyk Peter T., Nichaman Milton Z., Church Timothy S., Blair Steven N., and Ross Robert, "Visceral Fat Is an Independent Predictor of All-cause Mortality in Men," *Obesity*, vol. 14, no. 2, pp. 336–341, Sep. 2012.
- [69] G. A. Rosito *et al.*, "Pericardial Fat, Visceral Abdominal Fat, Cardiovascular Disease Risk Factors, and Vascular Calcification in a Community-Based Sample: The Framingham Heart Study," *Circulation*, vol. 117, no. 5, pp. 605–613, Feb. 2008.
- [70] G. Marchesini *et al.*, "Nonalcoholic Fatty Liver Disease: A Feature of the Metabolic Syndrome," *Diabetes*, vol. 50, no. 8, pp. 1844–1850, Aug. 2001.
- [71] L. A. Adams *et al.*, "The Natural History of Nonalcoholic Fatty Liver Disease: A Population-Based Cohort Study," *Gastroenterology*, vol. 129, no. 1, pp. 113–121, Jul. 2005.
- [72] J. Aucouturier, M. Meyer, D. Thivel, M. Taillardat, and P. Duché, "Effect of Android to Gynoid Fat Ratio on Insulin Resistance in Obese Youth," *Arch. Pediatr. Adolesc. Med.*, vol. 163, no. 9, pp. 826–831, Sep. 2009.
- [73] J. P. Wilson, A. M. Kanaya, B. Fan, and J. A. Shepherd, "Ratio of Trunk to Leg Volume as a New Body Shape Metric for Diabetes and Mortality," *PLoS ONE*, vol. 8, no. 7, p. e68716, Jul. 2013.
- [74] S. B. Heymsfield and J. Stevens, "Anthropometry: continued refinements and new developments of an ancient method," *Am. J. Clin. Nutr.*, vol. 105, no. 1, pp. 1–2, Jan. 2017.
- [75] "Obesity," *nhs.uk*. [Online]. Available: <https://www.nhs.uk/conditions/obesity/>. [Accessed: 05-May-2018].
- [76] A. Keys, F. Fidanza, M. J. Karvonen, N. Kimura, and H. L. Taylor, "Indices of relative weight and obesity," *J. Chronic Dis.*, vol. 25, no. 6, pp. 329–343, Jul. 1972.
- [77] K. V. Bailey and A. Ferro-Luzzi, "Use of body mass index of adults in assessing individual and community nutritional status.," *Bull. World Health Organ.*, vol. 73, no. 5, pp. 673–680, 1995.
- [78] S. P. Garnett, L. A. Baur, and C. T. Cowell, "Waist-to-height ratio: a simple option for determining excess central adiposity in young people," *Int. J. Obes.*, vol. 32, no. 6, pp. 1028–1030, Apr. 2008.
- [79] N. Y. Krakauer and J. C. Krakauer, "A New Body Shape Index Predicts Mortality Hazard Independently of Body Mass Index," *PLoS ONE*, vol. 7, no. 7, p. e39504, Jul. 2012.
- [80] I. Janssen, P. T. Katzmarzyk, and R. Ross, "Waist circumference and not body mass index explains obesity-related health risk," *Am. J. Clin. Nutr.*, vol. 79, no. 3, pp. 379–384, Mar. 2004.

- [81] L. de Koning, A. T. Merchant, J. Pogue, and S. S. Anand, "Waist circumference and waist-to-hip ratio as predictors of cardiovascular events: meta-regression analysis of prospective studies," *Eur. Heart J.*, vol. 28, no. 7, pp. 850–856, Apr. 2007.
- [82] Wei Ming, Gaskill Sharon P., Haffner Steven M., and Stern Michael P., "Waist Circumference as the Best Predictor of Noninsulin Dependent Diabetes Mellitus (NIDDM) Compared to Body Mass Index, Waist/hip Ratio and Other Anthropometric Measurements in Mexican Americans—A 7-Year Prospective Study," *Obes. Res.*, vol. 5, no. 1, pp. 16–23, Sep. 2012.
- [83] M. Ashwell, P. Gunn, and S. Gibson, "Waist-to-height ratio is a better screening tool than waist circumference and BMI for adult cardiometabolic risk factors: systematic review and meta-analysis," *Obes. Rev.*, vol. 13, no. 3, pp. 275–286, 2012.
- [84] Mason Caitlin and Katzmarzyk Peter T., "Variability in Waist Circumference Measurements According to Anatomic Measurement Site," *Obesity*, vol. 17, no. 9, pp. 1789–1795, Sep. 2012.
- [85] J. Nadas, Z. Putz, G. Kolev, S. Nagy, and G. Jermendy, "Intraobserver and interobserver variability of measuring waist circumference," *Med. Sci. Monit.*, vol. 14, no. 1, pp. CR15–CR18, 2008.
- [86] J. Bro_ek and A. Henschel, *Techniques for Measuring Body Composition: Proceedings of a Conference, Quartermaster Research and Engineering Center, Natick, Massachusetts, January 22-23, 1959*. National Academies, 1961.
- [87] J. Brožek, F. Grande, J. T. Anderson, and A. Keys, "Densitometric analysis of body composition: revision of some quantitative assumptions," *Ann. N. Y. Acad. Sci.*, vol. 110, no. 1, pp. 113–140, 1963.
- [88] P. Dempster and S. Aitkens, "A new air displacement method for the determination of human body composition.,," *Med. Sci. Sports Exerc.*, vol. 27, no. 12, pp. 1692–1697, 1995.
- [89] M. A. McCrory, T. D. Gomez, E. M. Bernauer, and P. A. Molé, "Evaluation of a new air displacement plethysmograph for measuring human body composition.,," *Med. Sci. Sports Exerc.*, vol. 27, no. 12, pp. 1686–1691, 1995.
- [90] D. A. Fields, M. I. Goran, and M. A. McCrory, "Body-composition assessment via air-displacement plethysmography in adults and children: a review," *Am. J. Clin. Nutr.*, vol. 75, no. 3, pp. 453–467, Mar. 2002.
- [91] N. Pace and E. N. Rathbun, "Studies on body composition. 3. The body water and chemically combined nitrogen content in relation to fat content.,," *J. Biol. Chem.*, vol. 158, pp. 685–691, 1945.
- [92] IAEA, "Introduction to Body Composition Assessment Using the Deuterium Dilution Technique with Analysis of Saliva Samples by Fourier Transform Infrared Spectrometry," 2011.
- [93] T. C. Prentice *et al.*, "STUDIES OF TOTAL BODY WATER WITH TRITIUM 12," *J. Clin. Invest.*, vol. 31, no. 4, pp. 412–418, Apr. 1952.
- [94] U. G. Kyle *et al.*, "Bioelectrical impedance analysis—part I: review of principles and methods," *Clin. Nutr.*, vol. 23, no. 5, pp. 1226–1243, Oct. 2004.
- [95] M. Y. Jaffrin and H. Morel, "Body fluid volumes measurements by impedance: A review of bioimpedance spectroscopy (BIS) and bioimpedance analysis (BIA) methods," *Med. Eng. Phys.*, vol. 30, no. 10, pp. 1257–1269, 2008.

- [96] R. Buendia, “Improvements in Bioimpedance Spectroscopy Data Analysis: Artefact Correction, Cole Parameters, and Body Fluid Estimation,” KTH Royal Institute of Technology, 2013.
- [97] R. J. Toombs, G. Ducher, J. A. Shepherd, and M. J. Souza, “The Impact of Recent Technological Advances on the Trueness and Precision of DXA to Assess Body Composition,” *Obesity*, vol. 20, no. 1, pp. 30–39, Jan. 2012.
- [98] J. A. Shepherd, B. K. Ng, M. J. Sommer, and S. B. Heymsfield, “Body composition by DXA,” *Bone*, Jun. 2017.
- [99] S. Kaul *et al.*, “Dual-Energy X-Ray Absorptiometry for Quantification of Visceral Fat,” *Obesity*, vol. 20, no. 6, pp. 1313–1318, Jun. 2012.
- [100] S. Y. Lee and D. Gallagher, “Assessment methods in human body composition,” *Curr. Opin. Clin. Nutr. Metab. Care*, vol. 11, no. 5, pp. 566–572, Sep. 2008.
- [101] M. J. Delmonico *et al.*, “Longitudinal study of muscle strength, quality, and adipose tissue infiltration,” *Am. J. Clin. Nutr.*, vol. 90, no. 6, pp. 1579–1585, Dec. 2009.
- [102] M. Mourtzakis, C. M. M. Prado, J. R. Lieffers, T. Reiman, L. J. McCargar, and V. E. Baracos, “A practical and precise approach to quantification of body composition in cancer patients using computed tomography images acquired during routine care,” *Appl. Physiol. Nutr. Metab.*, vol. 33, no. 5, pp. 997–1006, Sep. 2008.
- [103] G. Delso *et al.*, “Clinical evaluation of zero-echo-time MR imaging for the segmentation of the skull,” *J. Nucl. Med. Off. Publ. Soc. Nucl. Med.*, vol. 56, no. 3, pp. 417–422, Mar. 2015.
- [104] M. A. Bredella *et al.*, “Comparison of DXA and CT in the Assessment of Body Composition in Premenopausal Women With Obesity and Anorexia Nervosa,” *Obes. Silver Spring Md*, vol. 18, no. 11, pp. 2227–2233, Nov. 2010.
- [105] M. Hadi, C. C. Chen, M. Whatley, K. Pacak, and J. A. Carrasquillo, “Brown fat imaging with 18F-6-fluorodopamine PET/CT, 18F-FDG PET/CT, and 123I-MIBG SPECT: a study of patients being evaluated for pheochromocytoma,” *J. Nucl. Med.*, vol. 48, no. 7, pp. 1077–1083, 2007.
- [106] M. J. Devlin, “The ‘Skinny’ on brown fat, obesity, and bone,” *Am. J. Phys. Anthropol.*, vol. 156, no. S59, pp. 98–115, Feb. 2015.
- [107] K. I. Stanford *et al.*, “Brown adipose tissue regulates glucose homeostasis and insulin sensitivity,” *J. Clin. Invest.*, vol. 123, no. 1, pp. 215–223, Jan. 2013.
- [108] S. Paquette, “3D scanning in apparel design and human engineering,” *IEEE Comput. Graph. Appl.*, vol. 16, no. 5, pp. 11–15, Sep. 1996.
- [109] P. R. M. Jones and M. Rioux, “Three-dimensional surface anthropometry: Applications to the human body,” *Opt. Lasers Eng.*, vol. 28, no. 2, pp. 89–117, Sep. 1997.
- [110] L. A. P. Kohn, J. M. Cheverud, G. Bhatia, P. Commean, K. Smith, and M. W. Vannier, “Anthropometric optical surface imaging system repeatability, precision, and validation,” *Ann. Plast. Surg.*, vol. 34, no. 4, pp. 362–371, 1995.
- [111] Y. Cui, S. Schuon, D. Chan, S. Thrun, and C. Theobalt, “3D shape scanning with a time-of-flight camera,” in *2010 IEEE Conference on Computer Vision and Pattern Recognition (CVPR)*, 2010, pp. 1173–1180.

- [112] J. C. K. Wells, “Three-Dimensional (3-D) Photonic Scanning: A New Approach to Anthropometry,” in *Handbook of Anthropometry*, V. R. Preedy, Ed. Springer New York, 2012, pp. 205–217.
- [113] B. Allen, B. Curless, and Z. Popović, “The Space of Human Body Shapes: Reconstruction and Parameterization from Range Scans,” in *ACM SIGGRAPH 2003 Papers*, New York, NY, USA, 2003, pp. 587–594.
- [114] J. C. Wells, P. Treleaven, and T. J. Cole, “BMI compared with 3-dimensional body shape: the UK National Sizing Survey,” *Am. J. Clin. Nutr.*, vol. 85, no. 2, pp. 419–425, Feb. 2007.
- [115] J. Wang, D. Gallagher, J. C. Thornton, W. Yu, M. Horlick, and F. X. Pi-Sunyer, “Validation of a 3-dimensional photonic scanner for the measurement of body volumes, dimensions, and percentage body fat,” *Am. J. Clin. Nutr.*, vol. 83, no. 4, pp. 809–816, 2006.
- [116] M. R. Pepper *et al.*, “Validation of a 3-dimensional laser body scanner for assessment of waist and hip circumference,” *J. Am. Coll. Nutr.*, vol. 29, no. 3, pp. 179–188, 2010.
- [117] J. C. K. Wells *et al.*, “Acceptability, Precision and Accuracy of 3D Photonic Scanning for Measurement of Body Shape in a Multi-Ethnic Sample of Children Aged 5-11 Years: The SLIC Study,” *PLoS ONE*, vol. 10, no. 4, p. e0124193, Apr. 2015.
- [118] G. M. Price, R. Uauy, E. Breeze, C. J. Bulpitt, and A. E. Fletcher, “Weight, shape, and mortality risk in older persons: elevated waist-hip ratio, not high body mass index, is associated with a greater risk of death,” *Am. J. Clin. Nutr.*, vol. 84, no. 2, pp. 449–460, Aug. 2006.
- [119] W. E. Consultation, “Waist circumference and waist-hip ratio,” 2011.
- [120] L. M. Browning, S. D. Hsieh, and M. Ashwell, “A systematic review of waist-to-height ratio as a screening tool for the prediction of cardiovascular disease and diabetes: 0.5 could be a suitable global boundary value,” *Nutr. Res. Rev.*, vol. 23, no. 2, pp. 247–269, Dec. 2010.
- [121] D. M. Thomas *et al.*, “Relationships between body roundness with body fat and visceral adipose tissue emerging from a new geometrical model,” *Obesity*, vol. 21, no. 11, pp. 2264–2271, Nov. 2013.
- [122] J. P. Bougourd and P. C. Treleaven, “Capturing the shape of a nation: size UK,” in *Proceedings of the International Federation of the Fashion Technology Institute (IFFTI) Conference*, 2002.
- [123] P. R. Apeageyi, “Application of 3 D body scanning technology to human measurement for clothing Fit,” *change*, vol. 4, no. 7, 2010.
- [124] L. A. Schwarz, A. Mkhitarian, D. Mateus, and N. Navab, “Human skeleton tracking from depth data using geodesic distances and optical flow,” *Image Vis. Comput.*, vol. 30, no. 3, pp. 217–226, Mar. 2012.
- [125] R. A. Clark *et al.*, “Validity of the Microsoft Kinect for assessment of postural control,” *Gait Posture*, vol. 36, no. 3, pp. 372–377, Jul. 2012.
- [126] H. Funaya, T. Shibata, Y. Wada, and T. Yamanaka, “Accuracy assessment of kinect body tracker in instant posturography for balance disorders,” in *2013 7th International Symposium on Medical Information and Communication Technology (ISMICT)*, 2013, pp. 213–217.
- [127] M. Reyes, A. Clapés, S. Escalera, J. Ramírez, and J. R. Revilla, “Posture Analysis and Range of Movement Estimation Using Depth Maps,” in *Advances in Depth Image Analysis and*

- Applications*, X. Jiang, O. R. P. Bellon, D. Goldgof, and T. Oishi, Eds. Springer Berlin Heidelberg, 2013, pp. 97–105.
- [128] J. J. Lee, J. H. Freeland-Graves, M. R. Pepper, P. R. Stanforth, and B. Xu, “Prediction of Android and Gynoid Body Adiposity via a Three-dimensional Stereovision Body Imaging System and Dual-Energy X-ray Absorptiometry,” *J. Am. Coll. Nutr.*, pp. 1–11, Apr. 2015.
- [129] J. J. Lee, J. H. Freeland-Graves, M. R. Pepper, W. Yu, and B. Xu, “Efficacy of thigh volume ratios assessed via stereovision body imaging as a predictor of visceral adipose tissue measured by magnetic resonance imaging,” *Am. J. Hum. Biol.*, vol. 27, no. 4, pp. 445–457, 2015.
- [130] G. M. Blake, H. W. Wahner, and I. Fogelman, *Evaluation Of Osteoporosis*. Taylor & Francis, 1998.
- [131] J. A. Shepherd and M. K. Oates, “ISCD DXA Body Composition Course,” 09-Aug-2014.
- [132] D. A. Schoeller *et al.*, “QDR 4500A dual-energy X-ray absorptiometer underestimates fat mass in comparison with criterion methods in adults,” *Am. J. Clin. Nutr.*, vol. 81, no. 5, pp. 1018–1025, May 2005.
- [133] G. Danaei *et al.*, “National, regional, and global trends in systolic blood pressure since 1980: systematic analysis of health examination surveys and epidemiological studies with 786 country-years and 5.4 million participants,” *Lancet Lond. Engl.*, vol. 377, no. 9765, pp. 568–577, Feb. 2011.
- [134] S. Basu, P. Yoffe, N. Hills, and R. H. Lustig, “The relationship of sugar to population-level diabetes prevalence: an econometric analysis of repeated cross-sectional data,” *PloS One*, vol. 8, no. 2, p. e57873, 2013.
- [135] E. S. Ford, “Risks for All-Cause Mortality, Cardiovascular Disease, and Diabetes Associated With the Metabolic Syndrome: A summary of the evidence,” *Diabetes Care*, vol. 28, no. 7, pp. 1769–1778, Jul. 2005.
- [136] R. J. Garrison and W. P. Castelli, “Weight and thirty-year mortality of men in the Framingham Study,” *Ann. Intern. Med.*, vol. 103, no. 6 (Pt 2), pp. 1006–1009, Dec. 1985.
- [137] S. W. Rabkin, F. A. L. Mathewson, and P.-H. Hsu, “Relation of body weight to development of ischemic heart disease in a cohort of young north American men after a 26 year observation period: The manitoba study,” *Am. J. Cardiol.*, vol. 39, no. 3, pp. 452–458, Jan. 1977.
- [138] A. Romero-Corral *et al.*, “Association of bodyweight with total mortality and with cardiovascular events in coronary artery disease: a systematic review of cohort studies,” *The Lancet*, vol. 368, no. 9536, pp. 666–678, Aug. 2006.
- [139] C. J. Lavie, A. De Schutter, D. A. Patel, A. Romero-Corral, S. M. Artham, and R. V. Milani, “Body Composition and Survival in Stable Coronary Heart Disease Impact of Lean Mass Index and Body Fat in the ‘Obesity Paradox,’” *J. Am. Coll. Cardiol.*, vol. 60, no. 15, pp. 1374–1380, Oct. 2012.
- [140] C. Zhang, K. M. Rexrode, R. M. van Dam, T. Y. Li, and F. B. Hu, “Abdominal Obesity and the Risk of All-Cause, Cardiovascular, and Cancer Mortality,” *Circulation*, vol. 117, no. 13, pp. 1658–1667, Apr. 2008.

- [141] T. Coutinho *et al.*, “Central obesity and survival in subjects with coronary artery disease: a systematic review of the literature and collaborative analysis with individual subject data,” *J. Am. Coll. Cardiol.*, vol. 57, no. 19, pp. 1877–1886, 2011.
- [142] R. Alissa, M. Esposito, K. Horner, and R. Oliver, “The influence of platelet-rich plasma on the healing of extraction sockets: an explorative randomised clinical trial,” *Eur. J. Oral Implantol.*, vol. 3, no. 2, 2010.
- [143] T. F. Cootes, G. J. Edwards, and C. J. Taylor, “Active appearance models,” *Pattern Anal. Mach. Intell. IEEE Trans. On*, vol. 23, no. 6, pp. 681–685, 2001.
- [144] T. F. Cootes, C. J. Taylor, D. H. Cooper, and J. Graham, “Active shape models—their training and application,” *Comput. Vis. Image Underst.*, vol. 61, no. 1, pp. 38–59, 1995.
- [145] D. Shi, S. R. Gunn, and R. I. Dampier, “Handwritten Chinese radical recognition using nonlinear active shape models,” *IEEE Trans. Pattern Anal. Mach. Intell.*, vol. 25, no. 2, pp. 277–280, 2003.
- [146] G. J. Edwards, T. F. Cootes, and C. J. Taylor, “Face recognition using active appearance models,” in *Computer Vision—ECCV’98*, Springer, 1998, pp. 581–595.
- [147] B. Van Ginneken, A. F. Frangi, J. J. Staal, B. M. ter Haar Romeny, and M. A. Viergever, “Active shape model segmentation with optimal features,” *IEEE Trans. Med. Imaging*, vol. 21, no. 8, pp. 924–933, 2002.
- [148] D. Beymer and T. Syeda-Mahmood, “Cardiac disease recognition in echocardiograms using spatio-temporal statistical models,” in *Engineering in Medicine and Biology Society, 2008. EMBS 2008. 30th Annual International Conference of the IEEE*, 2008, pp. 4784–4788.
- [149] S. Solloway, C. E. Hutchinson, J. C. Waterton, and C. J. Taylor, “The use of active shape models for making thickness measurements of articular cartilage from MR images,” *Magn. Reson. Med.*, vol. 37, no. 6, pp. 943–952, 1997.
- [150] T. Whitmarsh *et al.*, “Hip fracture discrimination from dual-energy X-ray absorptiometry by statistical model registration,” *Bone*, vol. 51, no. 5, pp. 896–901, 2012.
- [151] J. P. Wilson *et al.*, “Dual-energy X-ray absorptiometry–based body volume measurement for 4-compartment body composition,” *Am. J. Clin. Nutr.*, vol. 95, no. 1, pp. 25–31, Jan. 2012.
- [152] J. P. Wilson, B. Fan, and J. A. Shepherd, “Total and Regional Body Volumes Derived From Dual-Energy X-Ray Absorptiometry Output,” *J. Clin. Densitom.*, vol. 16, no. 3, pp. 368–373, Jul. 2013.
- [153] T. F. Cootes, M. C. Ionita, C. Lindner, and P. Sauer, “Robust and Accurate Shape Model Fitting Using Random Forest Regression Voting,” in *Computer Vision – ECCV 2012*, 2012, pp. 278–291.
- [154] D. Cristinacce and T. Cootes, “Automatic feature localisation with constrained local models,” *Pattern Recognit.*, vol. 41, no. 10, pp. 3054–3067, 2008.
- [155] M. Visser *et al.*, “Muscle mass, muscle strength, and muscle fat infiltration as predictors of incident mobility limitations in well-functioning older persons,” *J. Gerontol. A. Biol. Sci. Med. Sci.*, vol. 60, no. 3, pp. 324–333, 2005.
- [156] M. Visser *et al.*, “Validity of fan-beam dual-energy X-ray absorptiometry for measuring fat-free mass and leg muscle mass,” *J. Appl. Physiol.*, vol. 87, no. 4, pp. 1513–1520, 1999.

- [157] J. P. Wilson, “The search for advanced imaging descriptors of human body shape and their association to diabetes and other metabolic disorders,” University of California, San Francisco, 2013.
- [158] L. Humbert *et al.*, “3D-DXA: Assessing the Femoral Shape, the Trabecular Macrostructure and the Cortex in 3D from DXA images,” *IEEE Trans. Med. Imaging*, vol. 36, no. 1, pp. 27–39, 2017.
- [159] S. R. Goodyear *et al.*, “Can we improve the prediction of hip fracture by assessing bone structure using shape and appearance modelling?,” *Bone*, vol. 53, no. 1, pp. 188–193, 2013.
- [160] C. S. Fox *et al.*, “Abdominal Visceral and Subcutaneous Adipose Tissue Compartments Association With Metabolic Risk Factors in the Framingham Heart Study,” *Circulation*, vol. 116, no. 1, pp. 39–48, Jul. 2007.
- [161] O. Hamdy, S. Porramatikul, and E. Al-Ozairi, “Metabolic Obesity: The Paradox Between Visceral and Subcutaneous Fat,” *Curr. Diabetes Rev.*, vol. 2, no. 4, pp. 367–373, Nov. 2006.
- [162] Haarbo J., Gotfredsen A., Hassager C., and Christiansen C., “Validation of body composition by dual energy X-ray absorptiometry (DEXA),” *Clin. Physiol.*, vol. 11, no. 4, pp. 331–341, Apr. 2008.
- [163] T. L. Kelly, N. Berger, and T. L. Richardson, “DXA body composition: theory and practice,” *Appl. Radiat. Isot.*, vol. 49, no. 5, pp. 511–513, May 1998.
- [164] L. K. Micklesfield, J. H. Goedecke, M. Punyanitya, K. E. Wilson, and T. L. Kelly, “Dual-Energy X-Ray performs as well as clinical computed tomography for the measurement of visceral fat,” *Obesity*, vol. 20, no. 5, pp. 1109–1114, 2012.
- [165] E. Expert Panel on Detection, “Executive Summary of the Third Report of the National Cholesterol Education Program (NCEP) Expert Panel on Detection, Evaluation, and Treatment of High Blood Cholesterol in Adults (Adult Treatment Panel III),” *JAMA*, vol. 285, no. 19, pp. 2486–2497, May 2001.
- [166] N. D. D. Group, “Classification and diagnosis of diabetes mellitus and other categories of glucose intolerance,” *Diabetes*, vol. 28, no. 12, pp. 1039–1057, 1979.
- [167] Goodpaster BH, Krishnaswami S, Harris TB, and et al, “OBesity, regional body fat distribution, and the metabolic syndrome in older men and women,” *Arch. Intern. Med.*, vol. 165, no. 7, pp. 777–783, Apr. 2005.
- [168] J.-D. Lin, W.-K. Chiou, H.-F. Weng, Y.-H. Tsai, and T.-H. Liu, “Comparison of three-dimensional anthropometric body surface scanning to waist–hip ratio and body mass index in correlation with metabolic risk factors,” *J. Clin. Epidemiol.*, vol. 55, no. 8, pp. 757–766, Aug. 2002.
- [169] J.-D. Lin, W.-K. Chiou, H.-F. Weng, J.-T. Fang, and T.-H. Liu, “Application of three-dimensional body scanner: observation of prevalence of metabolic syndrome,” *Clin. Nutr.*, vol. 23, no. 6, pp. 1313–1323, 2004.
- [170] H. A. M. Daanen and F. B. Ter Haar, “3D whole body scanners revisited,” *Displays*, vol. 34, no. 4, pp. 270–275, Oct. 2013.
- [171] J. J. Lee, J. H. Freeland-Graves, M. R. Pepper, M. Yao, and B. Xu, “Predictive equations for central obesity via anthropometrics, stereovision imaging and MRI in adults,” *Obesity*, vol. 22, no. 3, pp. 852–862, Mar. 2014.

- [172] P. Tikuisis, P. Meunier, and C. Jubenville, "Human body surface area: measurement and prediction using three dimensional body scans," *Eur. J. Appl. Physiol.*, vol. 85, no. 3–4, pp. 264–271, 2001.
- [173] C. Jelenko, "Studies in burns. I. Water loss from the body surface.," *Ann. Surg.*, vol. 165, no. 1, pp. 83–96, Jan. 1967.
- [174] D. Pinkel, "The Use of Body Surface Area as a Criterion of Drug Dosage in Cancer Chemotherapy," *Cancer Res.*, vol. 18, no. 7, pp. 853–856, Aug. 1958.
- [175] A. L. Collins and H. D. McCarthy, "Evaluation of factors determining the precision of body composition measurements by air displacement plethysmography," *Eur. J. Clin. Nutr.*, vol. 57, no. 6, p. 770, 2003.
- [176] R. H. Eckel *et al.*, "Obesity and Type 2 Diabetes: What Can Be Unified and What Needs to Be Individualized?," *J. Clin. Endocrinol. Metab.*, vol. 96, no. 6, pp. 1654–1663, Jun. 2011.
- [177] E. E. Calle and R. Kaaks, "Overweight, obesity and cancer: epidemiological evidence and proposed mechanisms," *Nat. Rev. Cancer*, vol. 4, no. 8, pp. 579–591, Aug. 2004.
- [178] Javed A. *et al.*, "Diagnostic performance of body mass index to identify obesity as defined by body adiposity in children and adolescents: a systematic review and meta-analysis," *Pediatr. Obes.*, vol. 10, no. 3, pp. 234–244, Jun. 2014.
- [179] B. Bourgeois *et al.*, "Clinically applicable optical imaging technology for body size and shape analysis: comparison of systems differing in design," *Eur. J. Clin. Nutr.*, Sep. 2017.
- [180] B. K. Ng, B. J. Hinton, B. Fan, A. M. Kanaya, and J. A. Shepherd, "Clinical anthropometrics and body composition from 3D whole-body surface scans," *Eur. J. Clin. Nutr.*, vol. 70, no. 11, pp. 1265–1270, Nov. 2016.
- [181] P. Treleaven and J. Wells, "3D body scanning and healthcare applications," *Computer*, no. 7, pp. 28–34, 2007.
- [182] Y. Lu *et al.*, "Dual X-ray absorptiometry quality control: Comparison of visual examination and process-control charts," *J. Bone Miner. Res.*, vol. 11, no. 5, pp. 626–637, 1996.
- [183] P. J. Besl and N. D. McKay, "A method for registration of 3-D shapes," *IEEE Trans. Pattern Anal. Mach. Intell.*, vol. 14, no. 2, pp. 239–256, Feb. 1992.
- [184] K. M. Robinette, S. Blackwell, H. Daanen, M. Boehmer, and S. Fleming, "Civilian American and European Surface Anthropometry Resource (CAESAR), Final Report. Volume 1. Summary," Jun. 2002.
- [185] M. Hronek *et al.*, "Skinfold Anthropometry –The Accurate Method for Fat Free Mass Measurement in COPD," *COPD J. Chronic Obstr. Pulm. Dis.*, vol. 10, no. 5, pp. 597–603, Oct. 2013.
- [186] F. Bogo, J. Romero, M. Loper, and M. J. Black, "FAUST: Dataset and Evaluation for 3D Mesh Registration," in *2014 IEEE Conference on Computer Vision and Pattern Recognition*, 2014, pp. 3794–3801.
- [187] S. Zuffi and M. J. Black, "The stitched puppet: A graphical model of 3D human shape and pose," in *2015 IEEE Conference on Computer Vision and Pattern Recognition (CVPR)*, 2015, pp. 3537–3546.
- [188] A. Myronenko and X. Song, "Point set registration: Coherent point drifts," *IEEE Trans. Pattern Anal. Mach. Intell.*, vol. 32, no. 12, pp. 2262–2275, 2010.

- [189] S. Sperandei, M. C. Vieira, and A. C. Reis, “Adherence to physical activity in an unsupervised setting: Explanatory variables for high attrition rates among fitness center members,” *J. Sci. Med. Sport*, vol. 19, no. 11, pp. 916–920, 2016.
- [190] B. Allen, B. Curless, and Z. Popović, “Exploring the space of human body shapes: Data-driven synthesis under anthropometric control,” SAE Technical Paper, 2004.
- [191] F. Pedregosa *et al.*, “Scikit-learn: Machine learning in Python,” *J. Mach. Learn. Res.*, vol. 12, no. Oct, pp. 2825–2830, 2011.
- [192] “WHO | Obesity and overweight,” *WHO*. [Online]. Available: <http://www.who.int/mediacentre/factsheets/fs311/en/>. [Accessed: 04-Apr-2016].
- [193] “WHO | Double burden of malnutrition,” *WHO*. [Online]. Available: <http://www.who.int/nutrition/double-burden-malnutrition/en/>. [Accessed: 08-Nov-2017].
- [194] E. Tzioumis and L. S. Adair, “Childhood Dual Burden of Under- and Overnutrition in Low- and Middle-income Countries: A Critical Review,” *Food Nutr. Bull.*, vol. 35, no. 2, pp. 230–243, Jun. 2014.
- [195] Z. Wang, P. Deurenberg, W. Wang, A. Pietrobelli, R. N. Baumgartner, and S. B. Heymsfield, “Hydration of fat-free body mass: review and critique of a classic body-composition constant,” *Am. J. Clin. Nutr.*, vol. 69, no. 5, pp. 833–841, May 1999.
- [196] M. K. Mwangome, G. Fegan, A. M. Prentice, and J. A. Berkley, “Are diagnostic criteria for acute malnutrition affected by hydration status in hospitalized children? A repeated measures study,” *Nutr. J.*, vol. 10, p. 92, Sep. 2011.
- [197] M. J. Bossingham, N. S. Carnell, and W. W. Campbell, “Water balance, hydration status, and fat-free mass hydration in younger and older adults,” *Am. J. Clin. Nutr.*, vol. 81, no. 6, pp. 1342–1350, Jun. 2005.
- [198] S. von Haehling, J. E. Morley, and S. D. Anker, “An overview of sarcopenia: facts and numbers on prevalence and clinical impact,” *J. Cachexia Sarcopenia Muscle*, vol. 1, no. 2, pp. 129–133, Dec. 2010.
- [199] T. G. Lohman, “Applicability of body composition techniques and constants for children and youths,” *Exerc. Sport Sci. Rev.*, vol. 14, pp. 325–357, 1986.
- [200] J. P. Wilson, B. J. Strauss, B. Fan, F. W. Duewer, and J. A. Shepherd, “Improved 4-compartment body-composition model for a clinically accessible measure of total body protein,” *Am. J. Clin. Nutr.*, vol. 97, no. 3, pp. 497–504, Mar. 2013.
- [201] T. G. Lohman and S. B. Going, “Multicomponent models in body composition research: opportunities and pitfalls,” *Basic Life Sci.*, vol. 60, pp. 53–58, 1993.
- [202] C. J. Bartok-Olson, D. A. Schoeller, J. C. Sullivan, and R. R. Clark, “The ‘B’ in the Selinger Four-Compartment Body Composition Formula Should Be Body Mineral Instead of Bone Mineral,” *Ann. N. Y. Acad. Sci.*, vol. 904, no. 1, pp. 342–344, May 2000.
- [203] C. C. Glüer, G. Blake, Y. Lu, B. A. Blunt, M. Jergas, and H. K. Genant, “Accurate assessment of precision errors: how to measure the reproducibility of bone densitometry techniques,” *Osteoporos. Int. J. Establ. Result Coop. Eur. Found. Osteoporos. Natl. Osteoporos. Found. USA*, vol. 5, no. 4, pp. 262–270, 1995.
- [204] F. R. Hampel, “The Influence Curve and its Role in Robust Estimation,” *J. Am. Stat. Assoc.*, vol. 69, no. 346, pp. 383–393, Jun. 1974.

- [205] “FAQ - International Society for Clinical Densitometry (ISCD).” .
- [206] A. E. Smith-Ryan, M. G. Mock, E. D. Ryan, G. R. Gerstner, E. T. Trexler, and K. R. Hirsch, “Validity and reliability of a 4-compartment body composition model using dual energy x-ray absorptiometry-derived body volume,” *Clin. Nutr.*, vol. 36, no. 3, pp. 825–830, Jun. 2017.
- [207] I. of M. (US) C. on M. N. Research, S. J. Carlson-Newberry, and R. B. Costello, *Bioelectrical Impedance: A History, Research Issues, and Recent Consensus*. National Academies Press (US), 1997.
- [208] C. Vaché *et al.*, “Bioelectrical impedance analysis measurements of total body water and extracellular water in healthy elderly subjects,” *Int. J. Obes. Relat. Metab. Disord. J. Int. Assoc. Study Obes.*, vol. 22, no. 6, pp. 537–543, Jun. 1998.
- [209] R. A. Newcombe *et al.*, “KinectFusion: Real-time dense surface mapping and tracking,” in *2011 10th IEEE International Symposium on Mixed and Augmented Reality (ISMAR)*, 2011, pp. 127–136.
- [210] A. D. Laidevant, S. Malkov, C. I. Flowers, K. Kerlikowske, and J. A. Shepherd, “Compositional breast imaging using a dual-energy mammography protocol,” *Med. Phys.*, vol. 37, no. 1, pp. 164–174, Jan. 2010.
- [211] S. Malkov and J. Shepherd, “Combining 3D optical imaging and dual energy absorptiometry to measure three compositional components,” 2014, vol. 8937, pp. 893714–893714–6.
- [212] F. L. Siena, B. Byrom, P. Watts, and P. Breedon, “Utilising the Intel RealSense Camera for Measuring Health Outcomes in Clinical Research,” *J. Med. Syst.*, vol. 42, no. 3, p. 53, Mar. 2018.
- [213] S. C. Mitchell, J. G. Bosch, B. P. Lelieveldt, R. J. van der Geest, J. H. Reiber, and M. Sonka, “3-D active appearance models: segmentation of cardiac MR and ultrasound images,” *Med. Imaging IEEE Trans. On*, vol. 21, no. 9, pp. 1167–1178, 2002.
- [214] X. Gao, Y. Su, X. Li, and D. Tao, “A review of active appearance models,” *IEEE Trans. Syst. Man Cybern. Part C Appl. Rev.*, vol. 40, no. 2, pp. 145–158, 2010.
- [215] R. Cheng *et al.*, “Active appearance model and deep learning for more accurate prostate segmentation on MRI,” in *Medical Imaging 2016: Image Processing*, 2016, vol. 9784, p. 97842I.
- [216] I. Goodfellow, Y. Bengio, A. Courville, and Y. Bengio, *Deep learning*, vol. 1. MIT press Cambridge, 2016.
- [217] H. Greenspan, B. van Ginneken, and R. M. Summers, “Guest editorial deep learning in medical imaging: Overview and future promise of an exciting new technique,” *IEEE Trans. Med. Imaging*, vol. 35, no. 5, pp. 1153–1159, 2016.
- [218] G. Litjens *et al.*, “A survey on deep learning in medical image analysis,” *Med. Image Anal.*, vol. 42, pp. 60–88, 2017.
- [219] O. Ronneberger, P. Fischer, and T. Brox, “U-Net: Convolutional Networks for Biomedical Image Segmentation,” in *Medical Image Computing and Computer-Assisted Intervention – MICCAI 2015*, 2015, pp. 234–241.
- [220] A. Krizhevsky, I. Sutskever, and G. E. Hinton, “ImageNet Classification with Deep Convolutional Neural Networks,” in *Advances in Neural Information Processing Systems 25*, F.

- Pereira, C. J. C. Burges, L. Bottou, and K. Q. Weinberger, Eds. Curran Associates, Inc., 2012, pp. 1097–1105.
- [221] Z. Zhang, P. Luo, C. C. Loy, and X. Tang, “Facial landmark detection by deep multi-task learning,” in *European Conference on Computer Vision*, 2014, pp. 94–108.
- [222] Y. Zheng, D. Liu, B. Georgescu, H. Nguyen, and D. Comaniciu, “3D deep learning for efficient and robust landmark detection in volumetric data,” in *International Conference on Medical Image Computing and Computer-Assisted Intervention*, 2015, pp. 565–572.
- [223] R. Ranjan, V. M. Patel, and R. Chellappa, “Hyperface: A deep multi-task learning framework for face detection, landmark localization, pose estimation, and gender recognition,” *IEEE Trans. Pattern Anal. Mach. Intell.*, 2017.
- [224] M. Loper, N. Mahmood, J. Romero, G. Pons-Moll, and M. J. Black, “SMPL: A skinned multi-person linear model,” *ACM Trans. Graph. TOG*, vol. 34, no. 6, p. 248, 2015.
- [225] G. Pons-Moll, J. Romero, N. Mahmood, and M. J. Black, “Dyna: A model of dynamic human shape in motion,” *ACM Trans. Graph. TOG*, vol. 34, no. 4, p. 120, 2015.
- [226] F. Bogo, J. Romero, G. Pons-Moll, and M. J. Black, “Dynamic faust: Registering human bodies in motion,” in *Proc. the Conference on Computer Vision and Pattern Recognition*, 2017.
- [227] C. Lassner, J. Romero, M. Kiefel, F. Bogo, M. J. Black, and P. V. Gehler, “Unite the people: Closing the loop between 3d and 2d human representations,” in *IEEE Conf. on Computer Vision and Pattern Recognition (CVPR)*, 2017.
- [228] F. Bogo, A. Kanazawa, C. Lassner, P. Gehler, J. Romero, and M. J. Black, “Keep it SMPL: Automatic Estimation of 3D Human Pose and Shape from a Single Image,” *ArXiv160708128 Cs*, Jul. 2016.

Appendix: Code Availability

Several software tools and analysis scripts were developed over the course of this dissertation.

These pieces of code are maintained in secure repositories on the Shepherd Lab GitHub

(<https://github.com/shepherd-lab>). A listing of relevant repositories is provided below. Please direct

inquiries to Bennett Ng (bennett.ng@berkeley.edu) or John Shepherd (johnshep@hawaii.edu).

- **3c_dxa** (https://github.com/shepherd-lab/3c_dxa)

MATLAB program to extract quantitative 3-component bone, fat, and lean images from Hologic DXA scan files. Refer to section 4.1: High-resolution 3-component DXA image separation.

- **dxa_sam** (https://github.com/shepherd-lab/dxa_sam)

Statistical appearance model files for whole-body DXA scans to be used with `am_tools` and related software from Timothy F. Cootes (University of Manchester). Includes SAS and R code for analysis of statistical appearance models. Refer to section 4.2.2 Statistical Appearance Modeling.

- **shapeup** (<https://github.com/shepherd-lab/shapeup>)

Python scripts for processing 3D body shape meshes generated using Ganger template fitting software (Brett Allen and Brian Curless, University of Washington). Includes scripts for handling files and performing principal component analysis to generate shape models and synthesize predicted body meshes. Refer to 5.2: The Shape Up! Studies.

- **4c_dxa_bia** (https://github.com/shepherd-lab/4c_dxa_bia)

Python and SAS analysis code for simplified 4-component body composition from DXA and BIA measurements. Refer to section 6.1: Validation of DXA + BIA for Clinical 4C Body Composition Assessment.


- **ultradxa** (<https://github.com/shepherd-lab/ultradxa>)

Development scripts to support the Ultra DXA project. This includes KScan3D scripts for acquiring and processing depth images from Kinect cameras, MATLAB and Python scripts to perform timing-based alignment, and analysis code for step phantom data. Refer to section 6.2: Ultra DXA + 3D Optical Imaging for True 3C and 4C Whole-Body Imaging.

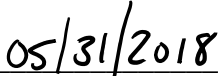
Publishing Agreement

It is the policy of the University to encourage the distribution of all theses, dissertations, and manuscripts. Copies of all UCSF theses, dissertations, and manuscripts will be routed to the library via the Graduate Division. The library will make all theses, dissertations, and manuscripts accessible to the public and will preserve these to the best of their abilities, in perpetuity.

I hereby grant permission to the Graduate Division of the University of California, San Francisco to release copies of my thesis, dissertation, or manuscript to the Campus Library to provide access and preservation, in whole or in part, in perpetuity.



Author Signature



Date